

**Measuring transversity in polarized p+p  
collisions with di-hadron correlations at  
 $\sqrt{s} = 200$  GeV at the STAR experiment**

Keith Landry

today

## **Abstract**

The transversity distribution  $h_1(x)$  of a transversely polarized proton describes the fraction of partons with polarization parallel to the parent proton, carrying a momentum fraction  $x$  of the parent proton. This distribution is fundamental for our understanding of the proton spin structure but still very much unknown for values of  $x$  larger than about 0.15. In order to understand transversity better, we study transversely spin-polarized proton collisions at STAR, as polarized p+p collisions at RHIC can access this  $x$  region and, with a higher scale and transverse momentum, probe a different kinematic regime than SIDIS. We find sizable spin asymmetries in di-hadron correlations, which can be used to directly probe the transversity distribution of quarks inside protons because they arise from a transversely spin polarized quark fragmenting into two hadrons by the Interference Fragmentation Function.

# Contents

<b>List of Figures</b>	<b>6</b>
<b>List of Tables</b>	<b>10</b>
<b>1 Introduction</b>	<b>13</b>
1.1 Substructure of the atom . . . . .	13
1.2 Quantum Mechanical Spin . . . . .	14
1.3 Nucleon Structure . . . . .	15
1.4 quark model . . . . .	16
1.5 Electron Proton Scattering and Stucture Functions . . . . .	17
1.6 Factorization theorem and the unpolarized parton distribution function . .	19
<b>2 Spin Physics</b>	<b>22</b>
2.1 Logintudinally Polarized Deep Inelastic Scattering . . . . .	22
2.2 Proton Spin Crisis . . . . .	24
2.3 Transversity Distribution Function . . . . .	25
2.4 First Experimental Measurements of Transversity . . . . .	26
2.4.1 In Single Hadron Production semi-inclusive DIS . . . . .	26
2.4.2 In Double Hadron Production semi-inclusive DIS . . . . .	27
2.4.3 In Proton Collisions . . . . .	29

2.5	Measuring the Interference Fragmentation Function at Belle . . . . .	29
2.6	Extracting IFF . . . . .	31
2.7	Summary . . . . .	32
<b>3</b>	<b>RHIC and The STAR Experiment</b>	<b>34</b>
3.1	The RHIC complex . . . . .	34
3.2	The STAR Detector . . . . .	37
3.3	STAR triggers? . . . . .	49
<b>4</b>	<b>Theoretical Background for Analysis</b>	<b>50</b>
<b>5</b>	<b>2006 analysis and sim</b>	<b>54</b>
<b>6</b>	<b>2012 IFF</b>	<b>59</b>
6.1	Data Set, Triggers, and Cuts . . . . .	59
6.2	Particle Identification and Contamination . . . . .	61
6.3	Finding $\pi^+\pi^-$ Pairs . . . . .	70
6.4	Pair Distributions . . . . .	71
6.5	Calculating The Asymmetry . . . . .	82
6.6	Analysis Code . . . . .	86
<b>7</b>	<b>Results</b>	<b>94</b>
7.1	One Dimensional Kinematic Binning . . . . .	94
7.2	Checking for Asymmetry in Same Sign Pairs . . . . .	99
7.3	Check For Other False Asymmetries . . . . .	101
7.4	Two Dimensional Kinematic Binning . . . . .	105
7.5	Asymmetry with partial wave expansion . . . . .	109
7.6	Kaon Pion Pairs . . . . .	112

<b>8 Theoretical Predictions</b>	<b>119</b>
8.0.1 Predictions for 2006 . . . . .	119
8.0.2 Predictions for 2012 . . . . .	121
<b>9 Pythia Tune Selection</b>	<b>124</b>
<b>10 Embedding Analysis</b>	<b>130</b>
<b>11 Trigger Bias</b>	<b>131</b>
<b>12 discussion</b>	<b>134</b>
<b>Bibliography</b>	<b>135</b>

# List of Figures

1.1	Scaling of the proton structure function $F_2$	18
1.2	Factorization theorem of $e + p \rightarrow X$	20
1.3	unpolarized parton distribution function	21
2.1	HERMES results for helicity distribution function	24
2.2		27
2.3	Interference Fragmentation Function	27
2.5	Asymmetry seen in $e^-e^+$ annihilation at Belle	30
2.6	Extraction of IFF from Belle data	32
2.7	Visual representation of unpolarized, helicity, and transversity distribution functions	33
3.1	The RHIC complex	36
3.2	Spin flip by Siberian Snake	37
3.3	STAR Time Projection Chamber	38
3.4	Anode sector of STAR TPC	40
3.5	Ionization energy loss in TPC gas	41
3.6	BEMC	42
3.7	Barrel Electromagnetic Calorimeter	44

3.8	Barrel Electromagnetic Calorimeter 2 . . . . .	45
3.9	Shower Maximum Detector cross sectional view . . . . .	46
3.10	Spatial reconstruction in the SMD . . . . .	46
3.11	pVPD detector element . . . . .	47
3.12	pVPD Assembly . . . . .	48
3.13	STAR Time of Flight System . . . . .	48
4.1	Angles $\phi_S$ and $\phi_R$ . . . . .	53
5.1	$A_{UT}$ vs Invariant Mass in 2006 data set . . . . .	55
5.2	$A_{UT}$ for different opening angles . . . . .	56
5.3	$A_{UT}$ vs $\eta^{\pi^+\pi^-}$ in 2006 data set . . . . .	57
5.4	Partonic momentum fraction in 2006 simulation forward and backward $\pi^+\pi^-$ pair . . . . .	58
6.1	Ionization energy loss in TPC . . . . .	62
6.2	$n_\sigma(\pi)$ distribution . . . . .	63
6.3	$n_\sigma(\pi)$ versus $n_\sigma(k)$ . . . . .	63
6.4	5-gaussian fit of $n_\sigma(\pi)$ distribution . . . . .	64
6.11	Schematic of Analysis . . . . .	70
6.12	$P_T$ distribution of $\pi^+$ . . . . .	72
6.13	$P_T$ distribution of $\pi^-$ . . . . .	72
6.14	$\phi$ distribution of $\pi^+$ . . . . .	73
6.15	$\phi$ distribution of $\pi^-$ . . . . .	73
6.16	$\eta$ distribution of $\pi^+$ . . . . .	74
6.17	$\eta$ distribution of $\pi^-$ . . . . .	74
6.18	$P_T$ distribution of $\pi^+\pi^-$ pair . . . . .	75

6.19	$\phi$ distribution of $\pi^+\pi^-$ pair . . . . .	75
6.20	$\eta$ distribution of $\pi^+\pi^-$ pair . . . . .	76
6.21	Invariant mass distribution of $\pi^+\pi^-$ pair . . . . .	76
6.22	$\phi_R$ distribution of $\pi^+\pi^-$ pair with reference to the yellow beam polarization	77
6.23	$\phi_R$ distribution of $\pi^+\pi^-$ pair with reference to the blue beam polarization .	77
6.24	$\phi_S$ distribution of $\pi^+\pi^-$ pair with reference to the yellow beam polarization	78
6.25	$\phi_S$ distribution of $\pi^+\pi^-$ pair with reference to the blue beam polarization .	78
6.26	$\phi_{RS}$ distribution of $\pi^+\pi^-$ pair with reference to the yellow beam polarization	79
6.27	$\phi_{RS}$ distribution of $\pi^+\pi^-$ pair with reference to the blue beam polarization	80
6.28	$\theta$ distribution of $\pi^+\pi^-$ pair . . . . .	80
6.29	$\cos\theta$ distribution of $\pi^+\pi^-$ pair . . . . .	81
6.30	Invariant mass of opposite and same sign pion pairs . . . . .	81
6.31	Sinusoid modulation of $\pi^+\pi^-$ pair produciton and fit for 9 $P_T^{\pi^+\pi^-}$ bins . .	85
6.32	something . . . . .	93
7.1	$P_T^{\pi^+\pi^-}$ Asymmetries 2012 and 2006 . . . . .	95
7.2	$M_{inv}^{\pi^+\pi^-}$ Asymmetries 2012 and 2006 . . . . .	95
7.3	$\eta^{\pi^+\pi^-}$ Asymmetries 2012 and 2006 . . . . .	96
7.4	Asymmetry vs $P_T^{\pi^+\pi^-}$ for different cone radii . . . . .	97
7.5	Asymmetry vs $M_{inv}^{\pi^+\pi^-}$ for different cone radii . . . . .	98
7.6	Asymmetry vs $\eta^{\pi^+\pi^-}$ for different cone radii . . . . .	98
7.7	comparison of $P_T$ asymmetry between same sign and opposite sign pairs . .	99
7.8	comparison of $M_{inv}$ asymmetry between same sign and opposite sign pairs .	100
7.9	comparison of $\eta$ asymmetry between same sign and opposite sign pairs . .	100
7.10	Asymmetry in $\pi^+\pi^-$ pairs when proton spin is randomly assigned . . . .	103
7.11	Asymmetry in $\pi^+\pi^-$ pair with randomly assigned charges . . . . .	104

7.12 Asymmetry vs $\eta^{\pi^+\pi^-}$ and $M_{inv}^{\pi^+\pi^-}$ 2D binning . . . . .	106
7.14 Asymmetry vs $\eta^{\pi^+\pi^-}$ and $P_T^{\pi^+\pi^-}$ 2D binning . . . . .	107
7.16 Asymmetry vs $M_{inv}^{\pi^+\pi^-}$ and $P_T^{\pi^+\pi^-}$ 2D binning . . . . .	108
7.18 Data and unbinned maximum likelihood fit . . . . .	110
7.19 $A_{sp}$ (black) and $A_{pp}$ (red) vs invariant mass for different $P_T^{\pi^+\pi^-}$ ranges for pion pairs scattered into the forward ( $\eta > 0$ ) direction . . . . .	111
7.22 Asymmetry vs Invariant Mass for Kaon Pion Pairs . . . . .	115
7.23 Asymmetry vs Invariant Mass for Kaon Pion Pairs . . . . .	116
7.24 Asymmetry vs Invariant Mass for different charge combinations of Kaon Pion Pairs . . . . .	117
9.4 Pion yield ratios for Perugia 0 and Perugia 2012 for nominal $k_T$ and reduced $k_T$ . . . . .	127
11.1 Trigger bias toward higher momentum fraction $x$ events . . . . .	133

## List of Tables

1.1	The eight lightest baryons in the quark model . . . . .	17
6.2	pion purity for 1D binning . . . . .	69
6.3	pion purity for 2D binning . . . . .	69
6.4	Binning for asymmetries differential in one kinematic variable . . . . .	88
6.5	Binning for asymmetries differential in two kinematic variables . . . . .	89
7.1	Track momentum bins for $K\pi$ analysis . . . . .	115

# Acronyms

<b>IFF</b>	interference fragmentation function
<b>QCD</b>	quantum chromo dynamics
<b>STAR</b>	Solenoid Tracker at RHIC
<b>RHIC</b>	Relativistic Heavy Ion Collider
<b>DIS</b>	deep inelastic scattering
<b>pdf</b>	parton distribution function
<b>HERMES</b>	?????
<b>SLAC</b>	Stanford Linear Accelerator Center
<b>Belle</b>	??????
<b>BNL</b>	Brookhaven National Laboratory
<b>AGS</b>	Alternating Gradient Synchrotron
<b>LINAC</b>	
<b>OPPIS</b>	optically pumped proton ion source
<b>TPC</b>	Time Projection Chamber

<b>BEMC</b>	Barrel Electromagnetic Calorimeter
<b>PMT</b>	photomultiplier tube
<b>SMD</b>	Shower Maximum detector
<b>ToF</b>	Time of Flight
<b>VPD</b>	
<b>BBC</b>	Beam Beam Counter
<b>JP</b>	Jet Patch trigger
<b>HT</b>	High Tower trigger
<b>UU</b>	unpolarized-unpolarized
<b>UT</b>	unpolarized-transversely polarized

# 1 Introduction

This thesis deals with the measurement of asymmetry in pion pair production from spin polarized proton collisions, which will allow for the extraction of the transversity distribution function, a fundamental piece needed to enhance our understanding of the proton's internal structure. However before this can be handled we must take a step back and take a look at what got us to this point. Therefore before delving into my analysis, I will include a brief overview of the relevant physics and motivation.

## 1.1 Substructure of the atom

From the ancient philosophers to current scientists, people have always been curious about the structure of matter. In the early 1800s John Dalton took the first large step down and even longer path. Dalton noticed that elements reacted in ratios of small whole numbers. As an explanation, he proposed the idea of atoms.<sup>f</sup> The next step came in 1897 when J.J. Thomson discovered the electron. He observed that cathode rays would bend in the presence of a magnet and therefore concluded that the rays were actually streams of particles carrying an electric charge. He was able to measure the charge to mass ratio which turned out much larger than expected. This indicated that the mass of the particle was very small. He figured this particle to be a constituent of the atom, but incorrectly proposed a “plum pudding model” where the electrons were suspended in the

accompanying positive charge making the neutral atom. Thomson's incorrect model of the atom was not adjusted until 1919 by Rutherford.

Rutherford challenged Thomson's model when he scattered alpha particles (not yet known to be helium nuclei) into a sheet of gold foil. If the plum pudding was correct, Rutherford expected the alpha particles to be deflected only slightly. What he observed was the opposite. Although most of the particles passed straight through, some of them were deflected wildly. This indicated the positive charge of the atom was concentrated in a very small nucleus. Rutherford named the nucleus of the lightest atom proton, but it wasn't until Chadwick discovered the neutron in 1932 other nuclei could be understood.[27]

As heavier nuclei were being described as multiple protons and neutrons, a natural question came up. *What is holding the nucleus together?* In fact with multiple protons all positively charged, one would expect the nucleus to fly apart. There must be another stronger force keeping it together. This conveniently became known as the strong force. In 1934 Yukawa proposed a theory for the strong force. It had to be very short ranged as we don't feel its effects on a large scale. Because of this Yukawa proposed it was mediated, much like the electromagnetic force is mediated by the photon, by a heavy particle. It wasn't until 1947 when Powell discovered Yukawa's predicted particle and named it the pion. At the same time another lighter particle was discovered that behaved similarly to an electron and given the name muon. The proton and neutron were grouped together and called baryons, or heavy weight particles, the electron and muon were light weight particles called leptons, and the pion was in between and classified a meson.[27]

## 1.2 Quantum Mechanical Spin

The Pauli exclusion principle and atomic spectra in the presence of an external magnetic field both hinted at the need for the electron to have another quantum number. This was

thought to be due to the electron spinning about an axis. Today we think of the electron as a point particle which cannot rotate, however the name “spin” stuck. The electron spin has an associated magnetic moment, which could naturally describe the atomic spectra seen from the Zeeman-effect.

$$\vec{\mu}_s = \frac{-ge}{2m_e} \vec{S} \approx \mu_B \quad (1.1)$$

The magnitude of the magnetic moment is approximately equal to the Bohr magneton.

The difference due to QED corrections.

The eigenvalues of the spin operators and it's z component are

$$S^2|s, m_s\rangle = \hbar^2 s(s+1)|s, m_s\rangle \quad S_z|s, m_s\rangle = \hbar m_s |s, m_s\rangle \quad (1.2)$$

As the spin-statistics theorem states, all particles with half integer spins are considered fermions, subject to the Pauli exclusion principle, and follow Fermi-Dirac statistics. All integer spin particles are considered bosons, follow Bose-Einstein statistics, and are allowed to occupy the same quantum states.

### 1.3 Nucleon Structure

Since the proton is a fermion with spin 1/2, it is expected to have a spin magnetic moment similar to that of the electron. Just as the electron's spin magnetic moment was approximatley equal to the Borh magneton, the proton's spin magnetic moment is expected to be approximately equal to the nuclear magneton  $\mu_N = e\hbar/2m_p$ . However the mesured value of the proton's spin magnetic moment is  $\mu_p \approx 2.8\mu_N$ . Moreover, the neutron's spin magnetic moment, which should be zero due to the neutron's lack of charge, was found to be  $\mu_n \approx -1.9\mu_N$ . These deviances from expected values were unexplainable

but hinted at the fact that nucleons were not elementary particles. This wasn't the only evidence that nucleons were not elementary. In a similar way Rutherford's scattering experiment suggested the positive charge was confined to a small volume inside the atom, deep inelastic scattering experiments at SLAC showed evidence that the charge of the proton was not distributed uniformly. Instead there was evidence of three substructures in the proton. It wasn't until the quark model this could be explained. fjdjfjklfjldjflsjfs  
ld use pic from textbook?

## 1.4 quark model

In the coming years experiments detected particles that behaved differently from those currently known. In 1949 a neutral particle, eventually called the  $K^0$ , was found to decay into a  $\pi^+$  and a  $\pi^-$ . In 1950 another neutral particle was found which decayed into a proton and a negatively charged pion. These newly discovered particles were labeled strange. By 1953 this strange label became a quantum number that had to be conserved just like electric charge. In fact this fits since these new strange particles are always created in pairs. In 1961 Gell-Mann was able to organize all the known particles using what he called the Eightfold Way. All the known mesons and baryons were arranged in a hexagon based on their electric charge and strangeness. Gell-Mann went even further by proposing that these meson and baryons were actually composed of smaller particles called quarks. He used these quarks to explain why the mesons and baryons were able to be grouped so nicely. His model consisted of three quarks, the up quark the down quark, and the strange quark. He also theorized these quarks were bound together by a force mediated by a gluon; a spin 1 boson. The quark makeup of the eight lightest baryons are shown in table 1.1. Today we know that there are six quarks, not just the three that originally proposed.

particle	quark content	rest mass	isospin	$J^p$	charge	strangeness
p	uud	938.27 MeV/ $c^2$	1/2	1/2 <sup>+</sup>	+1	0
n	udd	939.57 MeV/ $c^2$	1/2	1/2 <sup>+</sup>	0	0
$\Sigma^+$	uus	1189.37 MeV/ $c^2$	1	1/2 <sup>+</sup>	+1	-1
$\Sigma^0$	uds	1192.64 MeV/ $c^2$	1	1/2 <sup>+</sup>	0	-1
$\Sigma^-$	dds	1197.45 MeV/ $c^2$	1	1/2 <sup>+</sup>	-1	-1
$\Lambda^0$	uds	1115.68 MeV/ $c^2$	0	1/2 <sup>+</sup>	0	-1
$\Xi^0$	uss	1314.86 MeV/ $c^2$	1/2	1/2 <sup>+</sup>	0	-2
$\Xi^-$	dss	1321.71 MeV/ $c^2$	1/2	1/2 <sup>+</sup>	-1	-2

Table 1.1: The eight lightest baryons in the quark model

## 1.5 Electron Proton Scattering and Structure Functions

The proton structure can be investigated through the study of electron proton scattering.

The differential cross section for electron proton deep inelastic scattering, such as the experiments performed at SLAC, can be written in terms of two proton structure functions  $W_1(Q^2, x)$  and  $W_2(Q^2, x)$ .

$$\frac{d\sigma}{d\Omega} = \left( \frac{d\sigma}{d\Omega} \right)_{mott} \left[ 2W_1 \tan^2 \left( \frac{\theta}{2} \right) + W_2 \right] \quad (1.3)$$

where  $\left( \frac{d\sigma}{d\Omega} \right)_{mott}$  is the well known mott cross section.

In the deep inelastic scattering limit where the momentum transfer  $Q^2 \rightarrow \infty$  and proton momentum  $p \rightarrow \infty$ , but  $x = -\frac{q^2}{2q \cdot p}$  stays fixed, Bjorken predicted the  $Q^2$  dependence of

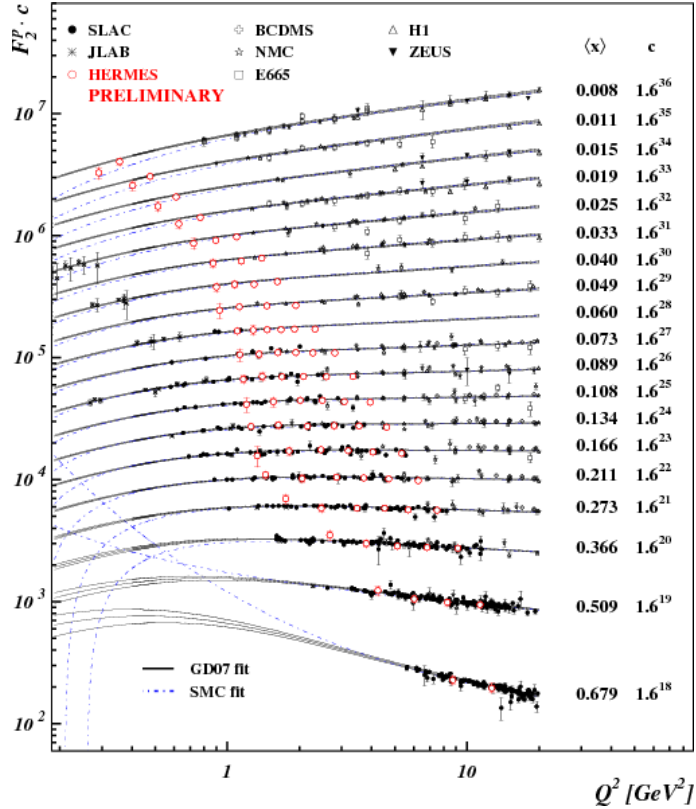


Figure 1.1: The proton structure function shows approximate Bjorken scaling.

the structure functions would disappear. We call this Bjorken scaling.

$$\lim_{Q^2 \rightarrow \infty, x \text{ fixed}} M W_1(Q^2, x) = F_1(x) \quad (1.4)$$

$$\lim_{Q^2 \rightarrow \infty, x \text{ fixed}} -\frac{q^2}{2Mx} W_2(Q^2, x) = F_2(x) \quad (1.5)$$

Although Bjorken scaling cannot exactly hold in any relativistic field theory, experiments have shown approximate Bjorken scaling. So structure functions in equations 1.4 and 1.5 will be written  $F_1(Q^2, x)$  and  $F_2(Q^2, x)$  with the dependence on  $Q^2$  being mild. This can be seen in figure 1.1. It was found that Bjorken scaling could be mildly violated in asymptotically free field theories. This led to the asymptotically free theory of Quantum Chromo Dynamics we have today.

## 1.6 Factorization theorem and the unpolarized parton distribution function

The factorization theorem says that in the DIS limit, scattering occurs between free partons. Because of this, we are able build up the structure functions for the proton from distributions of its constituent partons.

$$F_1(Q^2, x) = \sum_a \int_x^1 \frac{d\xi}{\xi} f_a(\xi, \mu) H_{1a} \left( \frac{x}{\xi}, \frac{Q^2}{\mu}, \alpha_s(\mu) \right) + \text{remainder} \quad (1.6)$$

$$\frac{1}{x} F_2(Q^2, x) = \sum_a \int_x^1 \frac{d\xi}{\xi} f_a(\xi, \mu) \frac{\xi}{x} H_{2a} \left( \frac{x}{\xi}, \frac{Q^2}{\mu}, \alpha_s(\mu) \right) + \text{remainder} \quad (1.7)$$

Here  $f_a(\xi, \mu)$  is the unpolarized parton distribution function. It gives the probability of finding a free quark for flavor  $a$  inside the proton with momentum fraction  $\xi$ . The renormalization scale,  $\mu$ , is free to be chosen. The functions  $H_{1a}$  and  $H_{2a}$  are the hard scattering coefficients which can be calculated. The convenient choice of  $\mu = Q$  will be used.[23] At leading order the form of the structure functions simplify. CITE GRIFFITH AND SCHOLARPEDIA?

$$F_2(Q^2, x) = 2x F_1(Q^2, x) = \frac{1}{2} \sum_a e_a^2 f_a(x, Q) \quad (1.8)$$

Where  $e_a$  is the charge of parton  $a$ .

The factorization theorem can also be applied directly to the cross sections. In this manor, we can write the cross section of electron proton scattering directly in terms of parton distribution functions and parton cross sections as seen in figure 1.2b.

$$\sigma_{ep} = \sum_a \int_x^1 d\xi f_a(\xi) \hat{\sigma}_{ea} \left( \frac{x}{\xi}, Q^2 \right) \quad (1.9)$$

Where  $\hat{\sigma}_{ea}$  is a calculable cross section for electron scattering off a parton of type  $a$ . In this way the factorization theorem can be generalized to other high energy processes.[23] The unpolarized distribution function  $f_1(x)$  is well known. It can be extracted by fitting a

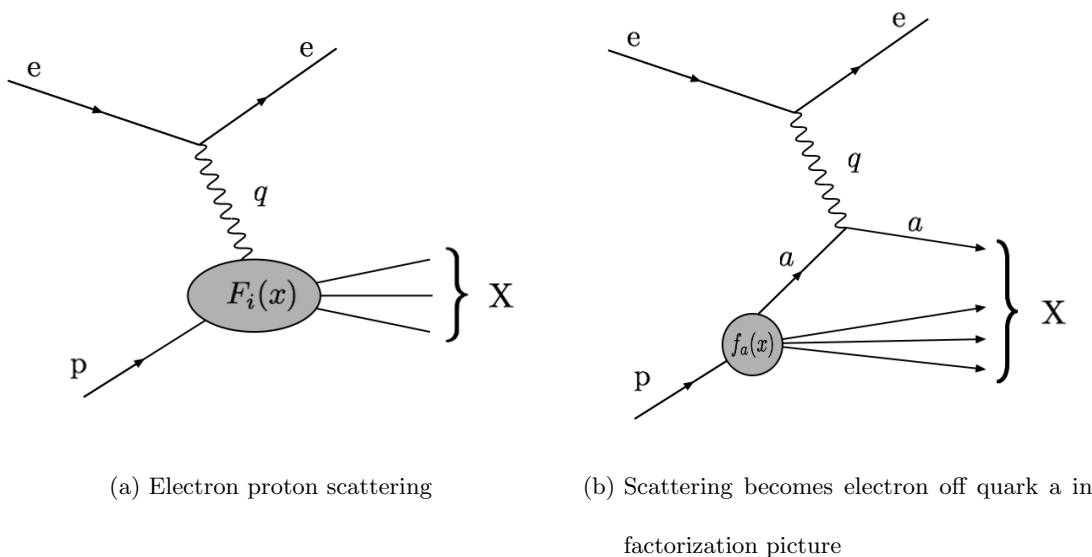


Figure 1.2: Factorization theorem of  $e + p \rightarrow X$

large number of data points from different DIS experiments at different values of  $Q^2$  and  $x$ . [9] In figure 1.3 the unpolarized distribution functions for different partons are shown. Not surprisingly partons carrying the largest momentum fraction  $x$  are the up quark and down quark.

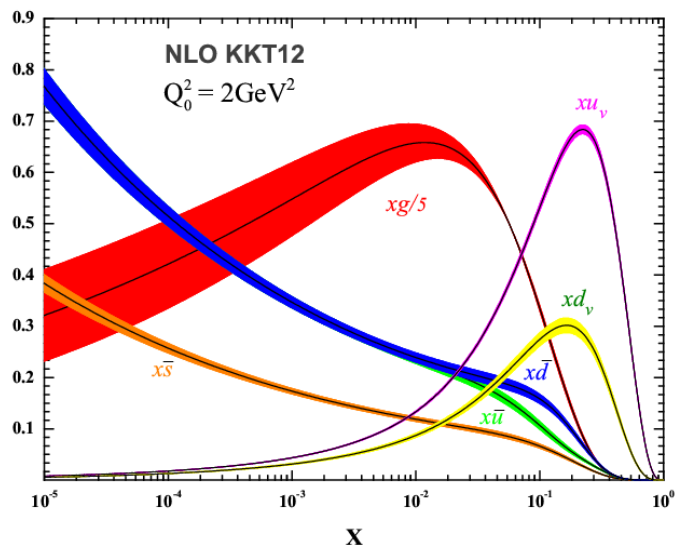


Figure 1.3: The unpolarized parton distribution functions as a function of  $x$  at initial scale

$Q_0^2 = 2 \text{ GeV}^2$  in NLO approximation.[9]

## 2 Spin Physics

While the unpolarized distribution tells us some information about the number density of quarks inside a proton, it does not give a complete picture, and does nothing to answer the question about the origin of proton spin. For this we need to look at spin dependent physics, which gives rise to spin dependent parton distribution functions. One of which will be of interest in the remainder of this thesis.

### 2.1 Logitudinally Polarized Deep Inelastic Scattering

A good starting point for the study of spin physics is the polarized version of deep inelastic scattering. Specifically we are interested in a longitudinally polarized lepton beam scattering off of a longitudinally polarized proton. Similarly to the unpolarized case, we can describe it in terms two structure functions  $G_1$  and  $G_2$ . The difference in cross sections when the beam and proton are polarized in the same versus opposite directions is given by

$$\frac{d^2\theta_{\leftarrow}^{\leftarrow}}{d\Omega dE'} - \frac{d^2\theta_{\rightarrow}^{\leftarrow}}{d\Omega dE'} = \frac{4\alpha^2 E'}{Q^2 E} \left[ (E + E' \cos\theta) MG_1(\nu, Q^2) - Q^2 G_2(\nu, Q^2) \right]. \quad (2.1)$$

Where  $E$  and  $E'$  are the energies of the lepton in the initial and final states,  $\nu = p \cdot q/M$ , and  $G_1$  and  $G_2$  are spin dependent structure funtions. In the deep inelastic scattering limit the structure functions  $G_1$  and  $G_2$  can be written in terms of dimensionless structure

functions that show approximate Bjorken scaling[15].

$$\lim_{Q^2 \rightarrow \infty, x \text{ fixed}} M^2 G_1(\nu, Q^2) = g_1(x) \quad (2.2)$$

$$\lim_{Q^2 \rightarrow \infty, x \text{ fixed}} M\nu^2 G_2(\nu, Q^2) = g_2(x) \quad (2.3)$$

At leading twist, the contribution from  $g_2$  vanishes. The spin dependent structure function  $g_1$  can be build up from parton distribution functions in the same way as the unpolarized structure functions. At leading order  $g_1$  is given by

$$g_1(x, Q^2) = \frac{1}{2} \sum_a e_a^2 (\Delta f_a(x, Q^2) + \Delta \bar{f}_a(x, Q^2)) . \quad (2.4)$$

Called the “helicity distribution function”,  $\Delta f$  describes, in the infinite momentum frame of the proton, the number of quarks inside a longitudinally polarized proton with their spin aligned minus the number of quarks with their spin anti-aligned with the proton’s spin carrying momentum fraction  $x$ [15].

In 1997 the HERMES collaboration measured  $g_1$  using a combination of inclusive and semi-inclusive lepton-nucleon deep inelastic scattering data. [] The data was taken with 27.6 GeV longitudinally polarized positron beam scattering off a longitudinally polarized hydrogen gas target. They constructed a single spin asymmetry  $A_{||}$  in the number of scattered positrons.

$$A_{||} = \frac{N^- L^+ - N^+ L^-}{N^- L_P^+ + N^+ L_P^-} \quad (2.5)$$

Where  $N^+(N^-)$  is the number of positrons scattered when the target spin is parallel(antiparallel) to the positron beam spin. The luminosities are  $L^+$ ,  $L^-$  when the target spin is parallel or antiparallel with the beam spin, while  $L_P^+$ ,  $L_P^-$  are weighted luminosities. The structure function  $g_1$  was extracted based on its relation to this asymmetry,

$$\frac{g_1}{F_1} = \frac{1}{1 + \gamma^2} \left[ \frac{A_{||}}{D} + (\gamma - \eta) A_2 \right] \quad (2.6)$$

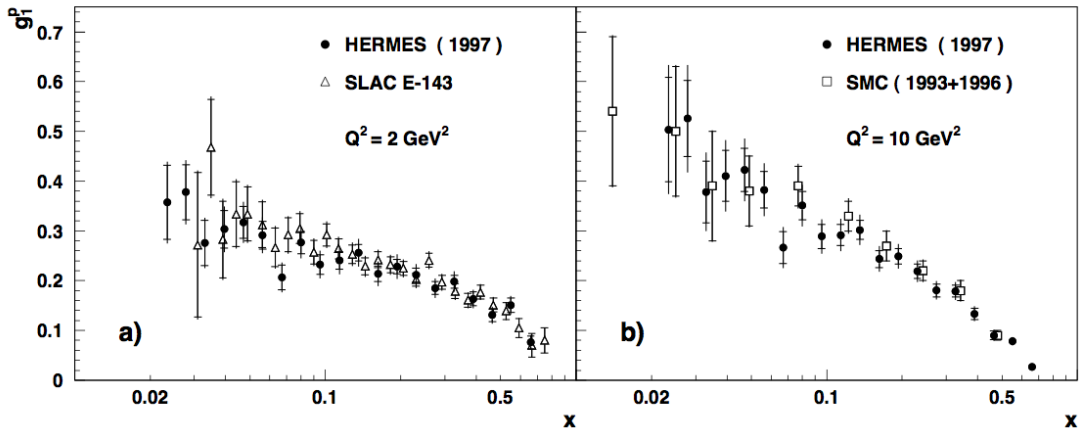


Figure 2.1: The helicity distribution as a function of momentum fraction  $x$  for  $Q^2 = 2$   $\text{GeV}^2$  and  $10 \text{ GeV}^2$ .

where  $\gamma = 2Mx/\sqrt{Q^2}$ . Here  $A_2$  was previously measured to be small[4][1]. Hermes is not the only collaboration to extract the helicity distribution. The Hermes data along with other experiments data is shown in figure 2.1.

## 2.2 Proton Spin Crisis

However the spin of the proton comes about, it must be conceived from the spin of the quarks,  $\Sigma$ , the orbital angular momentum of the quarks,  $L_q$ , the orbital angular momentum of the gluons,  $L_g$ , and the spin of the gluon,  $G$ . These must sum to equal the spin of the proton.

$$\frac{1}{2} = \frac{1}{2}\Sigma + L_q + L_g + G \quad (2.7)$$

In the naive quark model, it was expected that the entirety of the proton spin would be carried by the three valence quarks. In a relativistic theory with QCD corrections, only about 60% of the proton spin is thought to be carried by the quarks. The measured value of  $\int_0^1 dx g_1(x)$ , however corresponds to a value of  $\Sigma$  of  $0.120 \pm 0.16$  or consistent with zero. This suggests that virtually none of the proton spin is carried by valence quarks.

More recent measurements provide a value of  $0.27 \pm 0.05$  for  $\Sigma$ , still much smaller than theoretical prediction from relativistic models [32].

## 2.3 Transversity Distribution Function

So far only longitudinal spin has been taken into account. Another piece to the proton spin puzzle deals with transverse spin. This can be described by another parton distribution function (written  $h_1$  or  $\Delta_T f$ ), which wasn't even considered until Ralston and Soper introduced it in 1979[41], called the “transversity distribution function”. This distribution function describes the number of quarks with their spin aligned minus the number of quarks with their spin anti-aligned with the proton's spin carrying momentum fraction  $x$  when the proton's spin is perpendicular to its direction of motion. One might think this is equivalent to the helicity distribution function as the probability of finding a parton whose spin is aligned versus anti-aligned with the proton spin shouldn't depend on the direction of the proton spin. This is true for a proton in its rest frame. However this interpretation of the helicity and transversity distributions are only viable in the infinite momentum frame of the proton. In a relativistic setting such as this, Lorentz boosts cause these distributions to differ [11].

Unlike the helicity distribution function, the transversity distribution function does not appear in lepton inclusive deep inelastic scattering due to its chiral odd nature. In order to observe its effects, it must be paired with another chiral odd object to create a chiral even observable. Because of this, the transversity distribution function is currently not very well known.

## 2.4 First Experimental Measurements of Transversity

### 2.4.1 In Single Hadron Production semi-inclusive DIS

The detection of a single hadron in the final state introduces another chiral odd piece to the cross section in the form of a quark fragmentation function which describes how probable it is for a quark to fragment into a given hadron. When paired with the transversity distribution a chiral even observable is created, allowing the transversity distribution to be probed. This was first done by HERMES through semi-inclusive DIS of positrons off of a polarized proton target with a single hadron detected in the final state [5, 8],

$$e + p^\uparrow \rightarrow e + h + X. \quad (2.8)$$

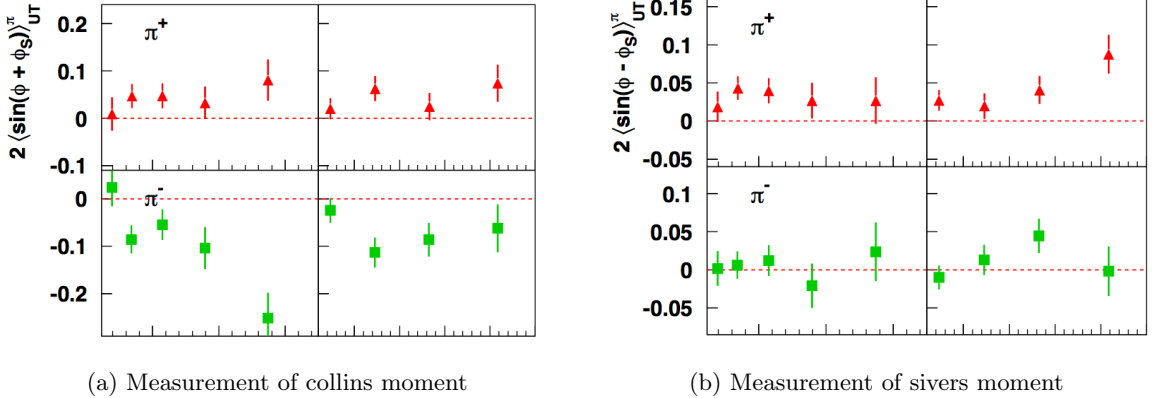
Just as in the experiment to measure the helicity distribution, a single spin asymmetry was detected ??,

$$A_{UT}^h(\phi, \phi_S) = \frac{1}{|S_T|} \frac{N_h^\uparrow(\phi, \phi_S) - N_h^\downarrow(\phi, \phi_S)}{N_h^\uparrow(\phi, \phi_S) + N_h^\downarrow(\phi, \phi_S)} \quad (2.9)$$

where  $N_h^{\uparrow(\downarrow)}(\phi, \phi_S)$  is the number of hadrons produced at azimuthal angle  $\phi$  and angle  $\phi_S$  to the proton spin when the spin is polarized up(down), and  $|S_T|$  is the polarization of the target proton spin.

There are two sources of this asymmetry present in the cross section. These are the Collins azimuthal moment  $\langle \sin(\phi + \phi_S) \rangle_{UT}^h$  and the Sivers moment  $\langle \sin(\phi - \phi_S) \rangle_{UT}^h$ . These were both measured and can be seen in figures 2.3a, 2.3b. From these transversity could be extracted [8].

Figure 2.2



#### 2.4.2 In Double Hadron Production semi-inclusive DIS

Quark fragmentation into two hadrons in the same jet, as described by the interference fragmentation function (IFF) and shown in figure 2.3, can also be paired with transversity to create a chiral even observable [25, 19]. This was done by the COMPASS collaboration [22] and the HERMES collaboration [21] via the process

$$e + p^\uparrow \rightarrow e + (\pi^+, \pi^-)_{jet} + X. \quad (2.10)$$

Once again a single spin asymmetry was measured. This is shown in figure 2.4 for the HERMES data. This asymmetry is related to the transversity distribution by [21],

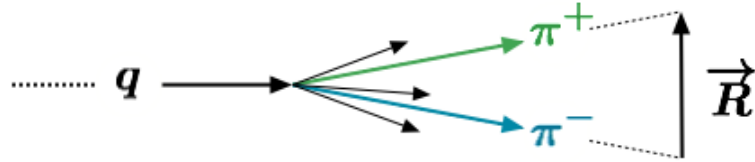


Figure 2.3: an outgoing quark fragments into a  $\pi^+\pi^-$  pair. This is described by the Interference Fragmentation Function (IFF). The Vector  $\vec{R}$  gives the orientation of the pair.

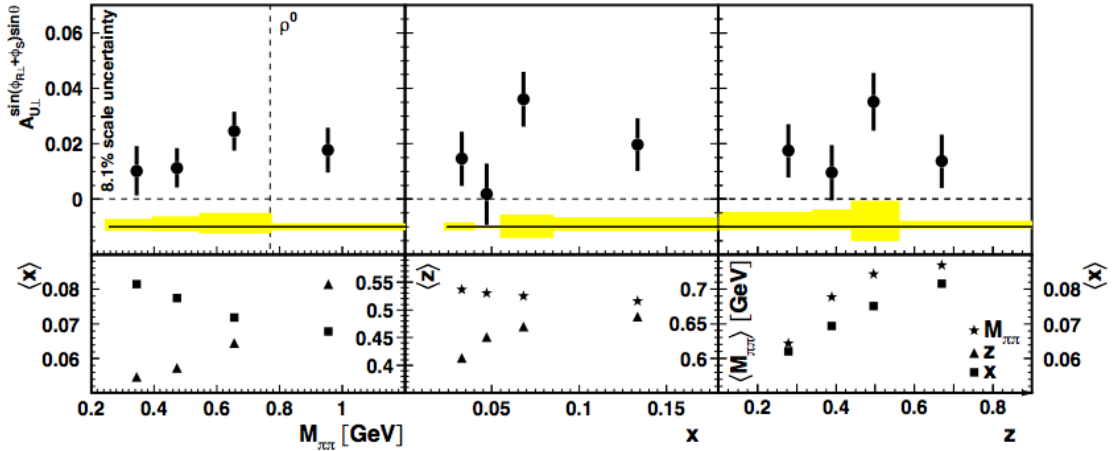


Figure 2.4

$$A_{UT}^{\sin(\phi_{R\perp} + \phi_S) \sin \theta} = -\frac{1-y}{1-y-\frac{y^2}{2}} \frac{1}{2} \sqrt{1-4 \frac{M_\pi^2}{M_{\pi\pi}^2} \frac{\sum_q e_q^2 h_1^q(x) H_{1,q}^{<,sp}(z, M_{\pi\pi})}{\sum_q e_q^2 f_1^q(x) D_{1,q}(z, M_{\pi\pi})}} \quad (2.11)$$

where  $y = (P \cdot q)/(P \cdot k)$ ,  $q$  and  $k$  are the momenta of the virtual photon and incoming positron respectively,  $H_{1,q}^{<,sp}(z, M_{\pi\pi})$  is the IFF describing the probability of transversely polarized quark  $q$  fragmenting into a pion pair with invariant mass  $M_{\pi\pi}$  retaining momentum fraction  $z$  of the fragmenting quark, and  $D_{1,q}(z, M_{\pi\pi})$  is the unpolarized partner of the IFF.

The asymmetry observed in this dihadron production does not depend on parton transverse momentum allowing it to be analyzed in the collinear framework. The single hadron production must be analyzed in the Transverse Momentum Dependent (TMD) framework. TMD factorization has been shown to not be equivalent between different processes, however collinear factorization is the same from process to process. This allows the dihadron production to be useful in comparing results in lepton scattering and hadronic collisions as well as making predictions [37].

### 2.4.3 In Proton Collisions

There are several benefits in measuring the transversity distribution in proton-proton collisions as well. First of all, it can act as a test of the universality of the parton distributions. Furthermore, in proton-proton collisions, the momentum fraction carried by the interacting quarks is much higher than the fixed target SIDIS experiments previously discussed. This allows us to extend our knowledge we have of the transversity distribution.

There are several ongoing experiments at STAR which are sensitive to the transversity distribution. One such experiment is single charged hadron, typically a pion, production  $p^\uparrow + p \rightarrow \pi + X$  at mid-rapidity coupled to the Collins Fragmentation Function. Another is mid-rapidity W and Z boson production coupled to the Sivers Function. In the forward rapidity, neutral pion production is sensitive to the transversity distribution through both the Collins and the Sivers Functions.

The rest of this thesis will cover the measurement of transversity through double charged hadron production  $p^\uparrow + p \rightarrow h_1^+ h_2^- + X$  at mid-rapidity. As mentioned in chapter 2.4.2, this is coupled with the Interference Fragmentation Function. Therefore in order to obtain useful information about the transversity distribution, we need a measurement of the IFF.

## 2.5 Measuring the Interference Fragmentation Function at Belle

In our experiment, transversity only shows up as a convolution with the interference fragmentation function,  $h_1 H_1^\triangleleft$ . In order to isolate transversity in our data we need to know how the interference fragmentation function behaves. Luckily for us Belle already did this work[45]. They performed an electron positron annihilation experiment detecting back to back  $\pi^+\pi^-$  pairs. A relative angle between the two pions was measured and a modulation  $a_{12}$  of the number of back to back pairs found at different values of the relative

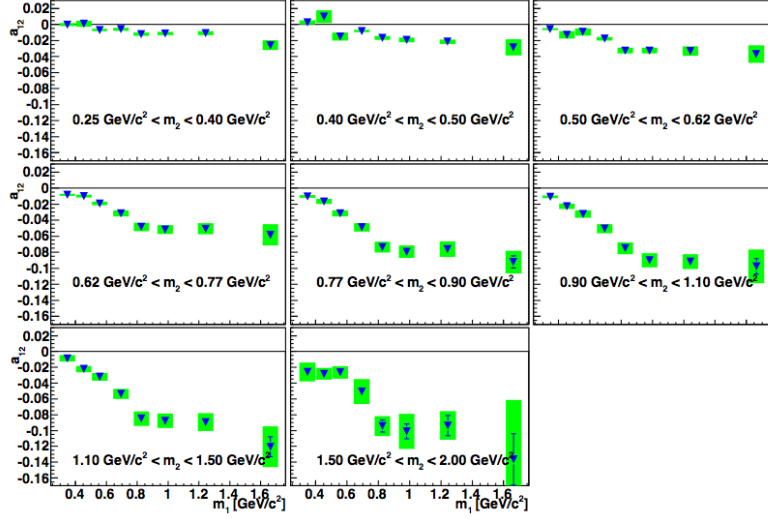


Figure 2.5: Asymmetry in the number of back to back pion pairs seen at Belle plotted vs the invariant mass.

angle was seen. This modulation, called the Artuo-Collins asymmetry is related to two IFFs.

$$a_{12} \propto \frac{1}{2} \frac{\sin^2 \theta}{1 + \cos^2 \theta} \left[ \sum_{q,\bar{q}} e_q^2 z_1^2 z_2^2 H_1^{\triangleleft q}(z_1, m_1^2) H_1^{\triangleleft \bar{q}}(z_2, m_2^2) \right]^{-1} \times \left[ \sum_{q,\bar{q}} e_q^2 z_1^2 z_2^2 D^q(z_1, m_1^2) D^{\bar{q}}(z_2, m_2^2) \right]^{-1} \quad (2.12)$$

Here  $\theta$  is the polar angle defined between the beam axis and the reference axis,  $D^q$  is the unpolarized equivalent of the IFF,  $z_{1(2)}$  is the energy fraction pion pair 1(2) has, and  $m_{1(2)}$  is the invariant mass of pair 1(2). The people at Belle reported the modulation  $a_{12}$  for different  $z_1, z_2$  bins as well as different  $m_1, m_2$  bins for different quark flavors. The modulation  $a_{12}$  is shown in figure 2.5 plotted versus the invariant mass. With this data, Courtoy et al were able to extract the Interference Fragmentation Function.[10]

## 2.6 Extracting IFF

The interference fragmentation function was extracted from the BELLE data using the replica method[10]. N sets of replica data points were produced by shifting the experimentally determined data points by gaussian noise with the same width as the measured error. It was found that roughly 100 replicas were sufficient for the mean and standard deviation of the replicated data points reflected the measurement accurately[38].

By integrating over the antiquark jet, the Arturo-Collins asymmetry from equation 2.12 becomes proportional to

$$a_{12} \propto \frac{H(z_1, m_1; Q^2)}{D(z_1, m_1; Q^2)}, \quad (2.13)$$

where  $D(z_1, m_1; Q^2)$  is known from other unpolarized experiments. Restricting to only up and down quarks and requiring  $n_u^\uparrow(Q^2) = -n_d^\uparrow(Q^2)$  gives

$$H(z_1, m_1; Q^2) = \frac{|\mathbf{R}|}{m_1} H_1^{\leftarrow u}(z_1, m_1; Q^2) n^\uparrow(Q^2). \quad (2.14)$$

Here the normalization  $n^\uparrow(Q^2) = \int dz \int dm_1 H(z_1, m_1; Q^2)$ .

A theoretical value  $H^{TH}(z_1, m_1, Q^2; \{p\})$  is a complicated function[39] with parameter vector  $\{p\}$  containing 9 parameters. These best-fit parameters were found for each replicated data set by minimizing the error

$$E_r^2(\{p\}) = \sum_{ij} (H_{ij}^{TH}(z_1, m_1, Q^2; \{p\}) - H_{ij}(z_1, m_1; Q^2))^2 / \sigma_{ij}^2 \quad (2.15)$$

where index  $i$  runs over the data points in invariant mass bin  $j$ . This results in  $N = 100$  different parameter vectors. The extracted value of  $H_1^{\leftarrow u}(z_1, m_1; Q^2)$  is calculated from  $H^{TH}(z_1, m_1, Q^2; \{p\})$  for each replica and a ratio is constructed.

$$R(z_1, m_1) = \frac{|\mathbf{R}|}{m_1} \frac{H_1^{\leftarrow u}(z_1, m_1; Q^2)}{D_1^u(z_1, m_1; Q^2)} \quad (2.16)$$

This ratio can be seen in figure 2.6 as a function of  $m_1$  for different values of the fractional

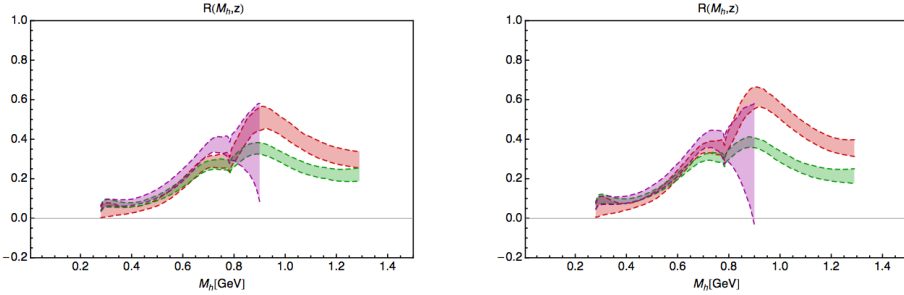


Figure 2.6: The ratio  $R(z, M_h)$  as a function of  $M_h$  for three values of  $z$ :  $z = 0.25$ (purple),  $z = 0.45$ (green), and  $z = 0.65$ (red). The left panel is for  $\alpha_s = 0.125$ , and the right pannel is for  $\alpha_s = 0.139$ [39]. Note: in their notation  $M_h = m_1$  is the invariant mass of the pion pair coming from the quark.

energy  $z$ . Each colored band represents one of these values of  $z$  and corresponds to 68% of the 100 replicas. Now armed with  $H_1^\triangleleft$ , we can access the transversity in our analysis.

## 2.7 Summary

To leading order, the parton kinematics inside a proton can be described by three parton distribution functions (figure 2.7); the unpolarized distribution function,  $f_1(x)$ , the helicity distribution function  $\Delta f(x)$ , and the transversity distribution function,  $h_1(x)$ [30]. The first two are known well from DIS experiments, while the transversity distribution is not. Due to its chiral odd nature, a more difficult experiment is required to probe the transversity of partons inside the proton. In the case of this thesis, a SIDIS experiment where two pions oppositely charged pions are detected will be utilized to probe transversity. The IFF, which is used to describe how a transversely polarized quark fragments into a pair of oppositely charged pions is used as the second chiral odd object to pair with the transversity distribution function in order to construct an observable. A more detailed overview of the physics involved in the experiment will be given in chapter 4.

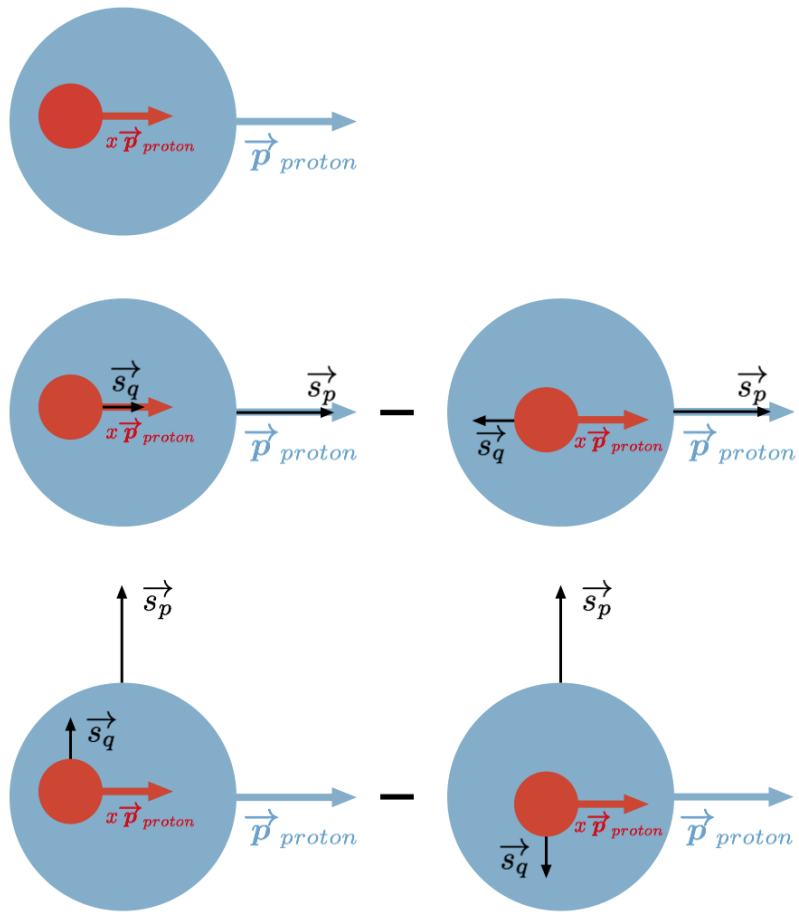


Figure 2.7: Top: Unpolarized distribution function  $f_1(x)$

Middle: Helicity distribution function  $\Delta f(x)$

Bottom: Transversity distribution function  $h_1(x)$

## 3 RHIC and The STAR Experiment

### 3.1 The RHIC complex

The Relativistic Heavy Ion Collider, located at Brookhaven Nation Lab, is one of the only places in the world that allows for spin polarized proton collisions, yet is also able to collide heavy nuclei as the name suggests. The RHIC complex, shown in figure 3.1, is composed of a chain of accelerators which boost the energy in steps before finally injecting the particles into the large ring of RHIC. Heavy nuclei are first delivered to the Booster Synchrotron where they are accelerated to 95MeV per nucleon. After which they are transferred to the Alternating Gradient Synchrotron (AGS). Here they are re-bunched into four bunches and accelerated to 10.8 GeV per nucleon, at which point they are injected into the RHIC ring and accelerated to their final energy. The highest energy RHIC can accommodate for heavy ions is 100 GeV per nucleon. The story for protons is a little different. They are injected already spin polarized into the Booster Synchrotron from an older LINAC accelerator. In order to keep the spin polarization for the proton beam, special magnets called Siberian Snakes are used. These magnets flip the proton spin by 180 degrees. From this point they are accelerated in the Booster and AGS before being injected into the RHIC storage ring. Here they are accelerated up to a maximum 250 GeV. The RHIC storage ring itself actually consists of two independent rings 3.8 km in

circumference. This allows for the collisions of different species. The independent rings intersect at six locations. the STAR detector is located at one such intersection points[34].

As acceleration of polarized protons in a circular accelerator cause resonances which act to depolarize the beam. Special magnets called Siberian Snakes are used to overcome these depolarizing resonances. The roll of the Siberian Snakes are to rotate the proton spin as shown in figure 3.2. If the spin rotation from the Siberian Snakes is much larger than that of the depolarizing resonances, the beam polarization is kept intact. In the RHIC ring, this is achieved with Siberian Snakes which rotate the proton spin by 180 degrees. The lower energy of the AGS calls for only partial Siberian Snakes which rotate less than 180 degrees, but still enough to maintain beam polarization. [28] Each Siberian Snake consists of 4 superconducting helical dipole magnets. Along with the Siberian Snakes, spin rotators are located at the six interaction points. These allow for the proton spin to be rotated from the transverse plane to the longitudinal plane before collisions. [28]

Polarized protons start out as polarized  $H^-$  ions produced from an optically pumped proton ion source (OPPIS). This source produces  $9 \times 10^{11}$  polarized  $H^-$  ions per  $300\mu s$  pulse. These polarized ions are then accelerated to 200 MeV in the LINAC. They are then stripped of the electrons and injected into the Booster where they are further accelerated to 10.5 GeV. From here they are sent to the AGS and accelerated to 25 GeV. The final step is a transfer to RHIC for acceleration to a maximum of 250 GeV and storage. [28]

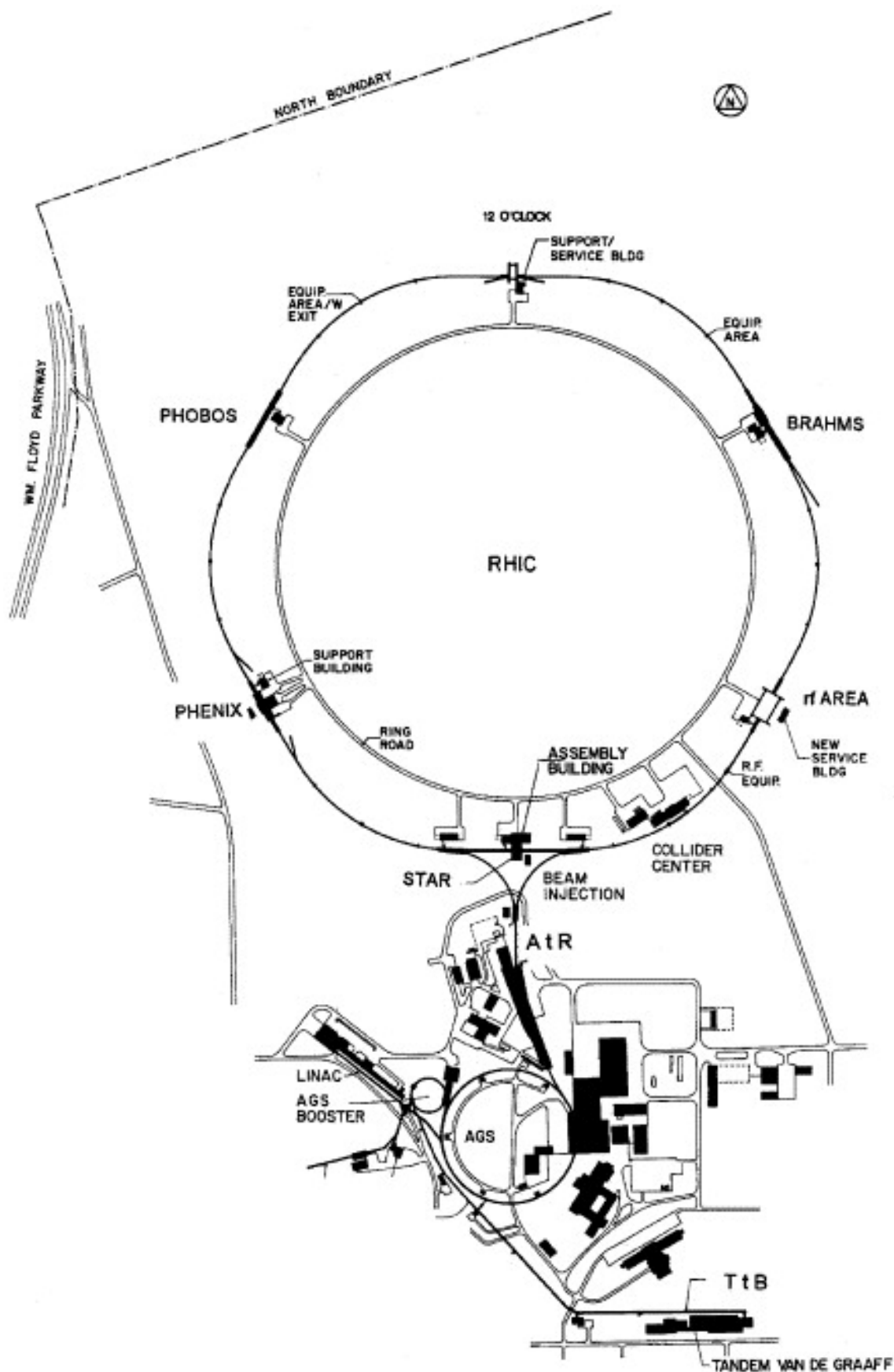


Figure 3.1: The RHIC complex

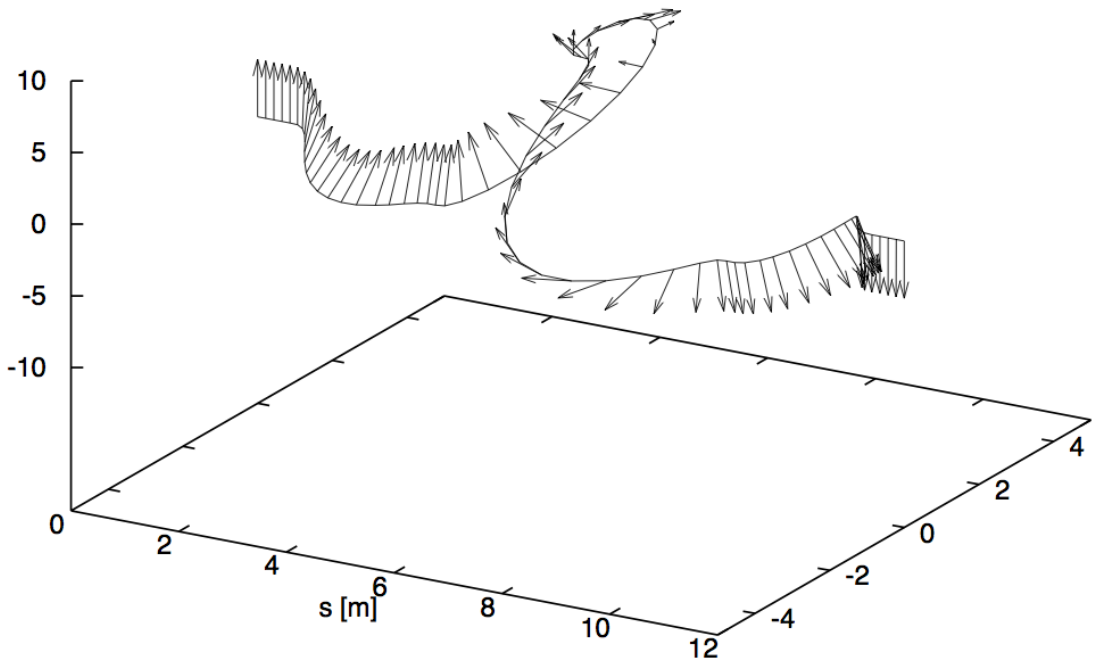


Figure 3.2: 180 degree proton spin flip by Siberian Snake

### 3.2 The STAR Detector

The Solenoid Tracker at RHIC (STAR) is located at the 6 o'clock position on the RHIC ring. It consists of several sub-detectors working in conjunction to detect, identify, and track particles.

#### Time Projection Chamber

One of the key detectors of STAR is the Time Projection Chamber (TPC). It is tasked with tracking particles, measuring momenta, and detecting ionization energy loss,  $dE/dx$ , to aid in particle identification. The TPC is the large cylindrical gas chamber covering  $\pm 1.8$  units of pseudorapidity around the interaction point. It's filled with a mixture of 10% methane and 90% argon at a pressure of 2mbar above atmospheric pressure. As a charged particle passes through the TPC, the gas is ionized, leaving a trail of electrons

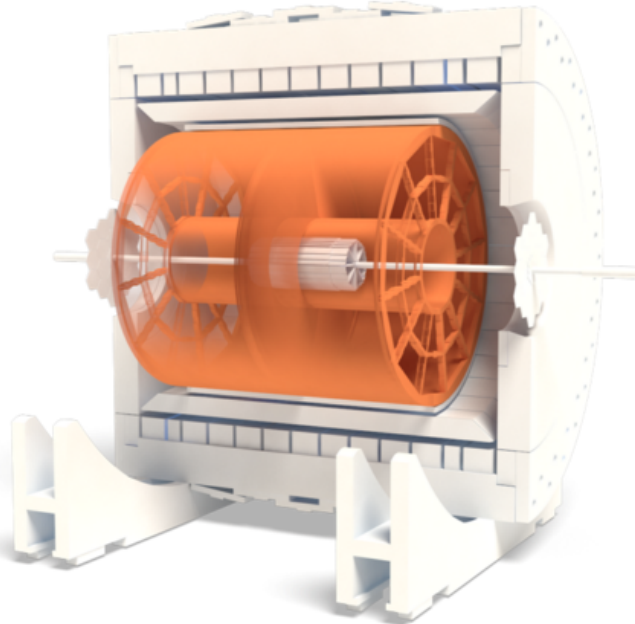


Figure 3.3: STAR Time Projection Chamber

in its wake. These electrons drift to the end caps of the TPC under a uniform electric field of about 135 V/cm where they are analyzed to reconstruct the track of the ionizing particle. The particle's path will curve due to the presence of STAR's magnetic field an amount proportional to the particles charge and it's velocity, allowing for the measurement of particle momenta, charge, and ionization energy loss.

At the center of the TPC is a central membrane which splits the TPC in two halves. This membrane is kept at 28 kV while the two end caps are at ground. A field cage is located around the TPC to create 182 equipotential slices in the TPC. This set up allows for a very uniform electric field to be kept.

A mixture of 10% methane and 90% argon is chosen for the TPC gas due to its fast drift velocity. This drift velocity also peaks at the operating electric field (135 V/cm) making it relatively unaffected by subtle fluctuations in the electric field.

The TPC gas drift velocity is calibrated with a laser system. Thirty six aluminum

plates are positioned on either side of the central membrane and are illuminated with an ultraviolet laser. This causes photo-ejection of electrons which drift to the end caps where they are read. The position of the aluminum plates are known with such precision that the time it takes the ejected electrons to reach the end cap readouts as well as the position they reach can be used for calibration.

The end cap is equipped with 12 modular sectors arranged in a circle. These sectors are arranged like a clock with only 3mm separating them. Each sector, shown in figure 3.4, has a grid of readout pads and a wire proportional chamber consisting of three wire girds; a gated grid, a shield (or ground) grid and an anode grid. The gated grid is required to keep boundary conditions with the central membrane and field cage in order to achieve the uniform electric field, and is thus arranged to do so. The anode wire plane is made up of  $20\mu$  wires aligned radially around the sector. This is to achieve maximum precision of the measurement of momenta from high momentum (straight) tracks. The anode grid is completed by wires in the other direction separated by 4 mm.

As the drifting electrons reach the anode grid an avalanche occurs triggering a temporary image charge to be induced on the read out pads. The width of each read out pad is chosen such that only three read out pads will share the signal from a single avalanche. This allows for the best centriod reconstruction. The grid of read out pads is broken up into two sections. The outer portion of the grid has continuously packed read-out pads measuring 6.7mm by 20mm optimized for good dE/dx resolution. These pads are located 4mm behind the anode grid. The inner portion has smaller read out pads measuring 3.35 mm by 12 mm optimized for good 2 hit detection. This helps with the large track density seen in the inner portion of the TPC. Unfortunately the available space for electronics for the small pads isn't large enough to have continuous coverage as in the outer section. Instead they are arranged in strips as seen in figure 3.4. This arrangement prohibits the

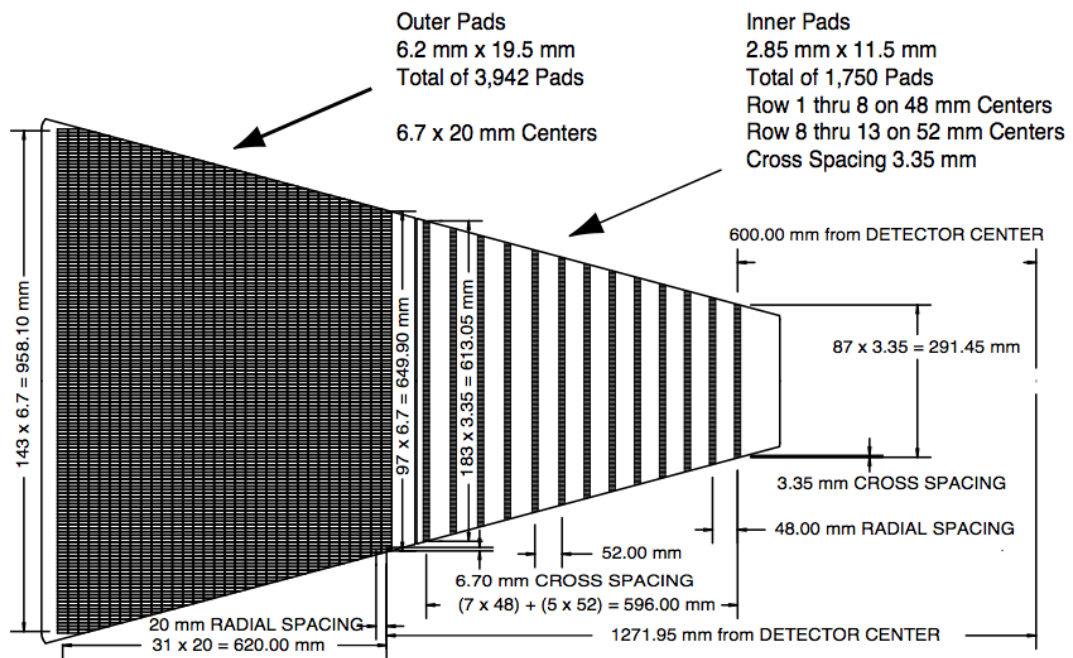


Figure 3.4: One of the 12 anode sectors of the TPC. The outer portion has densely packed pads, while the inner portion is composed of wider rows.

inner section to be much help in  $dE/dx$  resolution[7].

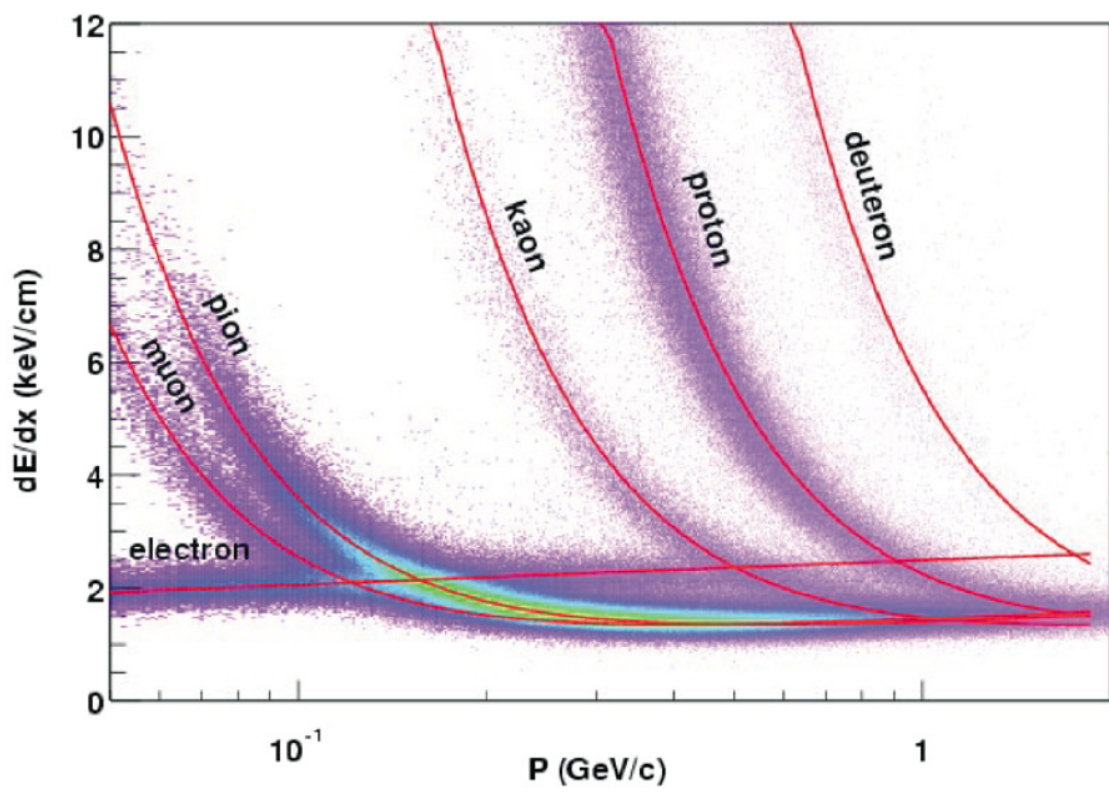


Figure 3.5: Ionization energy loss in TPC gas. Different species show different energy loss signature. This aids in particle identification.

## Barrel Electromagnetic Calorimeter

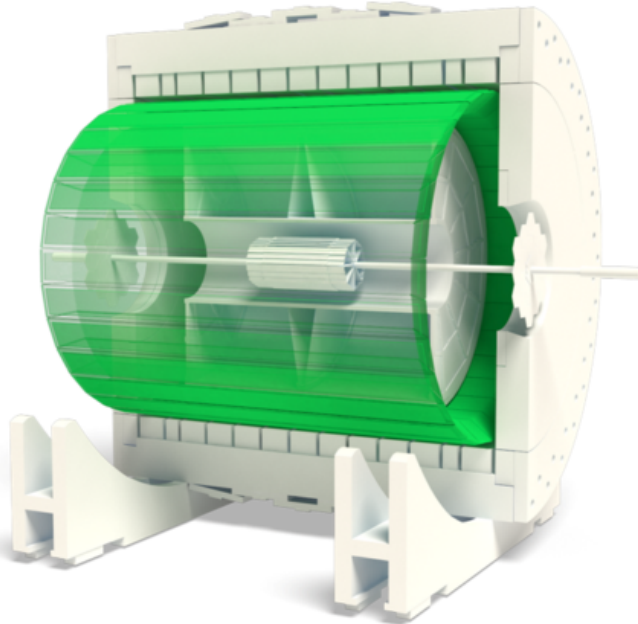


Figure 3.6: Barrel Electromagnetic Calorimeter (BEMC)

The Barrel Electromagnetic Calorimeter (BEMC) is a large array of lead and plastic scintillator sitting outside the TPC and inside the STAR magnet. At  $\eta = 0$  the BEMC is roughly 20 radiation lengths thick allowing it to contain electromagnetic showers up to 60 GeV. Scintillation light is carried from the BEMC array to outside the STAR magnet where it is fed into photomultiplier tubes (PMT).

The BEMC is composed of a total of 4800 towers, each one subtending  $0.05^\circ$  in  $\phi$  and 0.05 units in  $\eta$ . A tower consists of 20 layers of 5 mm thick lead, 19 layers of 5mm thick scintillator, and two layers of 6 mm thick scintillator. Each tower is angled toward the reaction region as seen in figure 3.8.

The BEMC is equipped with a pre-shower detector which provide readings of the longitudinal shower development after 1 to 1.5 radiation lengths. Made up of the first two (6 mm) scintillating layers of the tower, the pre-shower detector aids in distinguishing

between  $\pi^0$  and  $\gamma$  as well as between electrons and hadrons. Electrons will typically have a larger ionization energy loss  $dE/dx$  inside the BEMC than hadrons resulting in roughly 63% of electrons showering before the pre-shower volume and 84% by the middle of the pre-shower detector compared to only 3% and 6% for hadrons. The pre-shower detector consists of two 6 mm thick layers of scintillator instead of the 5 mm thick scintillator layers in the rest of the BEMC.

The active scintillating layers, both pre-shower and regular, are made of Kuraray SCSN81 and light from each layer is carried out with wavelength shifting fiber embedding into the scintillator layer. The scintillation light from each layer is transferred to a 2.1 m long optical cable which carries it passed the magnet to a decoder box. Here the light from all 21 layers in a tower, including the two pre-shower layers, are combined and fed into a single PMT. The pre-shower detector also passes a second sample of scintillation light from layers 1 and 2 to a separate PMT, this time not combined with light from any other layers.

As neutral particles, such as  $\pi^0$ , do not ionize the TPC gas, the BEMC is tasked with providing spacial resolution of such species. Instead of making the size of each tower of the BEMC comparable to the Moliere radius in the lead-plastic scintillator, a shower maximum detector (SMD) is added into the BEMC for spacial resolution. The SMD, set at about 5.6 radiation lengths at  $\eta = 0$ , is composed of an aluminum plate with divots on either side. As seen in figure 3.9, a  $50\mu\text{m}$  gold-plated tungsten anode wire lies in each divot. The wires run along the barrel. As the electromagnetic shower passes these wires a charge is induced. This charge is amplified by the gas in the divot. Detection strips are located on the top and bottom faces of the aluminum plate. One set of strips runs parallel to the wires and provides the spacial distribution of the shower in the  $\eta$  direction. The other set, running perpendicular to the wires provides the spacial distribution in the  $\phi$

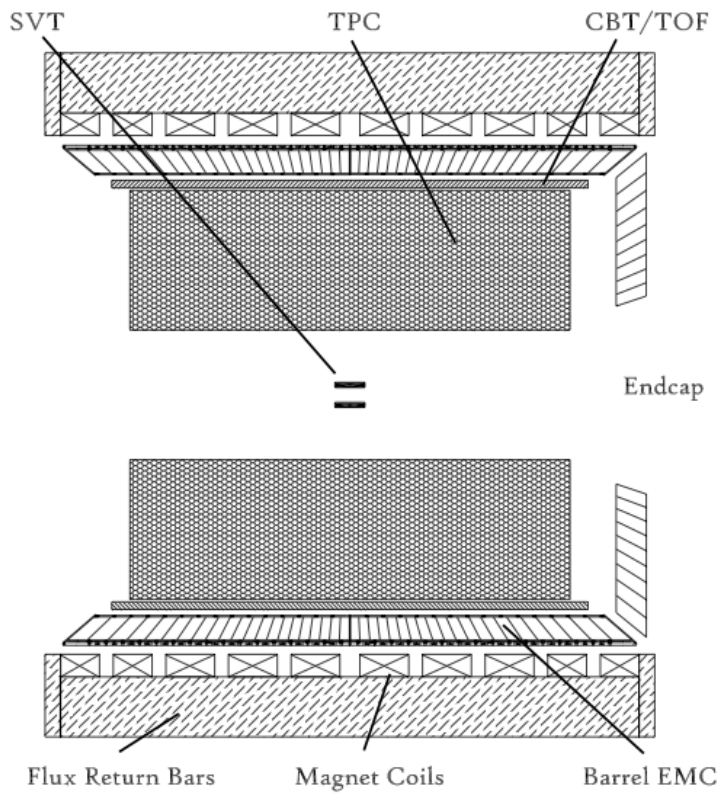


Figure 3.7: The BEMC is located outside the TPC but inside the STAR magnet and return bars. The scintillation light is transported past the magnet and return bars where it is read out by PMTs.

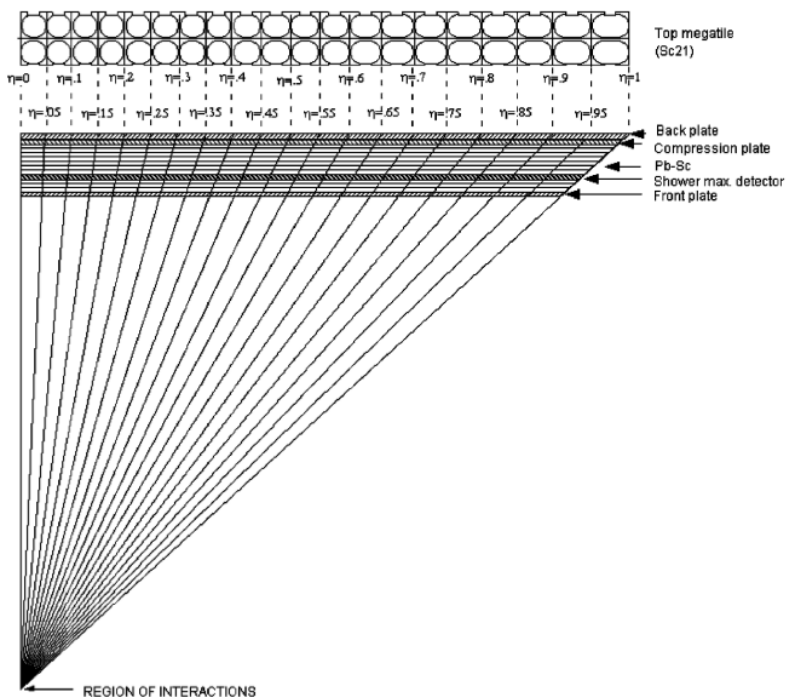


Figure 3.8: Each tower of the BEMC is angled to point back to the interaction region of STAR. The shower max detector as well as the individual scintillator/lead layers are shown.

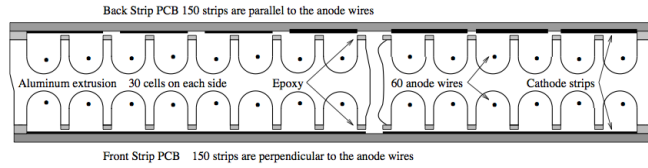


Figure 3.9: Cross sectional view of the shower max detector. Aluminum extrusion in the center containing two sets of anode wires. Cathode strips on the top and bottom face run either parralell or perpendicular to the anode wires.

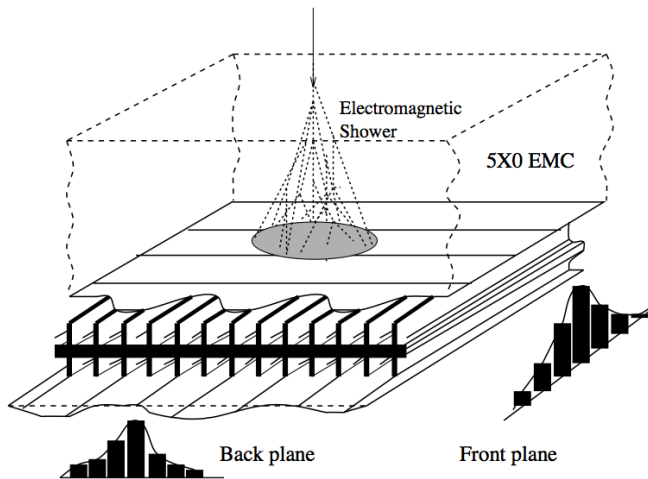


Figure 3.10: Schematic of spatial reconstruction in SMD. The cathode strips on the top and bottom faces read the induced charged in the  $\phi$  and  $\eta$  directions seperately.

direction. A schematic of this is shown in figure 3.10. Together They give a full description of the shower position.[16]

### **Endcap Electromagnetic Calorimeter**

#### **Time of Flight**

To aid in particle identification STAR has a time of flight system. The system is composed of two different detectors, the Time of Flight Patch (TOFp) and the Pseudo Vertex Position Detector (pVPD). Together these detectors allow for direct  $2\sigma \pi/K/p$

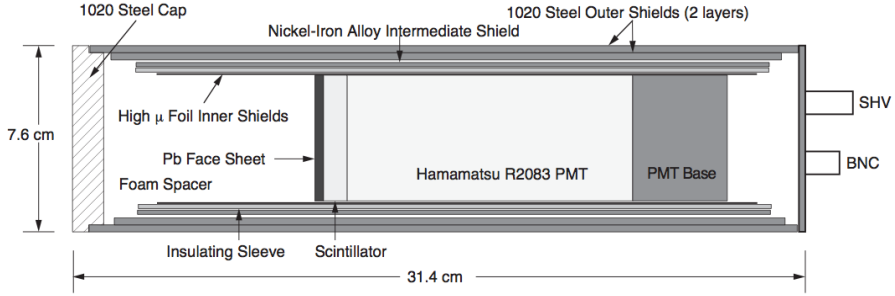


Figure 3.11: A cross section of a pVPD detector element.

identification for track momenta up to about  $1.7 \text{ GeV}/c$ .

The pVPD is responsible for starting the clock of the time of flight system. It consists of two plastic scintillator detectors, one on either side of the STAR interaction region sitting 5.6 m away from the center of the STAR detector. Both are positioned very close to the beam pipe and detect very forward, high energy photons produced in the collision. The average of the time for both detectors to see this photon pulse is declared the “start time” for the event. The scintillation light is read out by PMTs. The magnetic field strength near the pVPD is on the order of a few hundred Gauss. Because of this the PMTs are shielded on the sides with a steel outer shield, a nickel-Iron alloy intermediate shield, and finally a foil inner shield. They are also shielded from the front with a lead face sheet and a steel cap. A pVPD detector element is shown in figure 3.11. This is mounted to the beam pipe support structure as shown in figure 3.12.

The pVPD starts the clock for the event and the TPCp stops it. The TPCp, shown in figure 3.13, is again a scintillator/PMT detector. It covers about one unit in  $\eta$  and about  $1/60$  of STAR’s azimuthal coverage. It is encapsulated in an aluminum tray which is fastened to the outer field cage of the TPC at the 7 o’clock position. There are a total of 41 detector assemblies, each consisting of a  $3.81 \times 2 \times 10 \text{ cm}^3$  BC420 plastic scintillator and a PMT. The PMTs are specially designed to work inside the STAR magnet.[33]

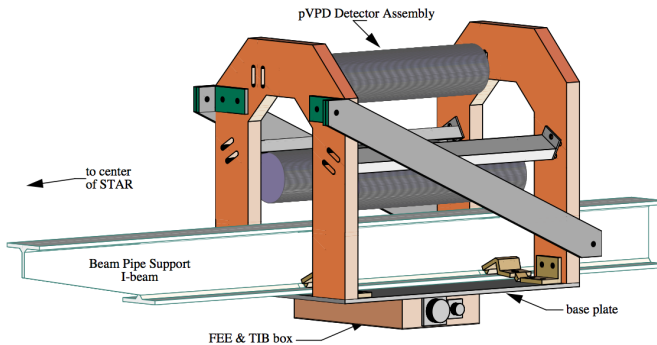


Figure 3.12: The pVVD detector is mounted in the assembly.

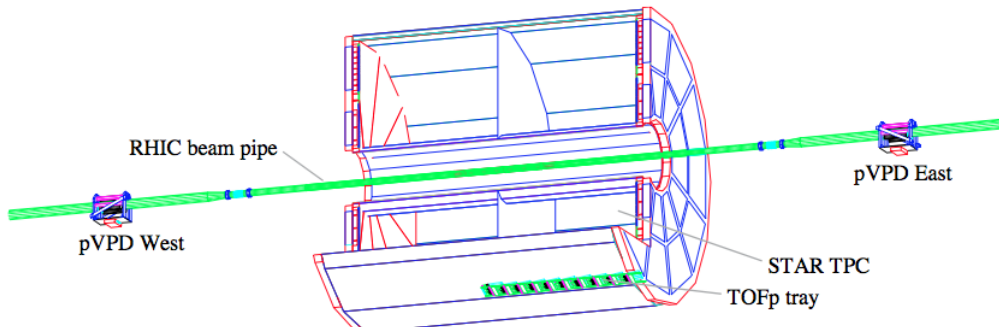


Figure 3.13: The Time of Flight Patch is located near the bottom of the STAR detector

at the 7 o'clock position. Also shown here are the two pVVD detectors on either side of the STAR detector.

Once the clock is stopped a value of  $\beta$  for the track can be calculated as in equation 3.1.

$$\frac{1}{\beta} = \frac{c\tau}{s} \quad (3.1)$$

Here  $c$  is the speed of light,  $\tau$  is the time measured by the time of flight system, and  $s$  is the path length of the track using the reconstructed path of the TPC. From here the mass of the particle can be found using the momentum of the track measured in the TPC.

$$M^2 = \frac{p^2}{\beta^2} - 1 \quad (3.2)$$

### 3.3 STAR triggers?

## 4 Theoretical Background for Analysis

One of the most theoretically clean ways to access the transversity distribution function is through the observation of a single spin asymmetry(SSA) in a semi-inclusive deep inelastic scattering(SIDIS) process between transversely polarized and unpolarized protons where a hadron pair is detected[6]. This thesis will be focused mainly on the case where the hadron pair is  $\pi^+\pi^-$ . At leading twist, only one source of a SSA exists[6].

The process we are interested in is  $p_a p_b^\uparrow \rightarrow \pi^+ \pi^- + X$ , where unpolarized proton  $a$  collides with transversely polarized proton  $b$  with spin  $\mathbf{s}_b$ . Outgoing pions with momentum  $p_{h,1}$  for the positively charged pion and  $p_{h,2}$  for the negatively charged pion are detected. The total pair momentum  $\mathbf{P}_h$  is the sum of  $p_{h,1}$  and  $p_{h,2}$ . The average of the pion momenta is defined as  $\mathbf{R} = (p_{h,1} - p_{h,2})/2$ .

The difference between cross sections when proton  $b$  is polarized up and down can be written in a factorized form which includes the transversity distribution  $h_1$ , and the IFF,  $H_1^\triangleleft$ .

$$\begin{aligned} d\sigma^\uparrow - d\sigma^\downarrow = d\sigma_{UT} &= 2P_T^{\pi^+\pi^-} \sum_{a,b,c,d} |\mathbf{s}_b| \frac{|\mathbf{R}|}{M_{inv}^{\pi^+\pi^-}} \sin(\phi_{RS}) \int \frac{dx_a dx_b}{8\pi^2 z_c} f_1(x_a) h_1(x_b) \frac{d\Delta\hat{\sigma}_{ab^\uparrow \rightarrow c^\uparrow d}}{d\hat{t}} \\ &\quad \times \sin \theta H_1^{\triangleleft c} (\bar{z}_c, \cos \theta, M_{inv}^{\pi^+\pi^-})^2 \end{aligned} \quad (4.1)$$

Where  $\theta$  is the angle between  $p_{h,1}$  in the center of mass frame of the pair and  $\mathbf{P}_h$  in the lab frame. In the above expression,  $\phi_{RS} = \phi_S - \phi_R$ , where  $\phi_S$  is the angle between the spin

vector or proton  $b$  and the scattering plane and  $\phi_R$  is the angle between the scattering plane and the two hadron plane. These angles are shown in figure 4.1 and defined as[6]

$$\begin{aligned}\cos \phi_S &= \frac{(\hat{\mathbf{P}}_b \times \mathbf{P}_h)}{|\hat{\mathbf{P}}_b \times \mathbf{P}_h|} \cdot \frac{(\hat{\mathbf{P}}_b \times \mathbf{S}_b)}{|\hat{\mathbf{P}}_b \times \mathbf{S}_b|} & \sin \phi_S &= \frac{(\mathbf{P}_h \times \mathbf{S}_b) \cdot \hat{\mathbf{P}}_b}{|\hat{\mathbf{P}}_b \times \mathbf{P}_h| |\hat{\mathbf{P}}_b \times \mathbf{S}_b|} \\ \cos \phi_R &= \frac{(\hat{\mathbf{P}}_h \times \mathbf{P}_a)}{|\hat{\mathbf{P}}_h \times \mathbf{P}_a|} \cdot \frac{(\hat{\mathbf{P}}_h \times \mathbf{R})}{|\hat{\mathbf{P}}_h \times \mathbf{R}|} & \sin \phi_R &= \frac{(\mathbf{P}_a \times \mathbf{R}) \cdot \hat{\mathbf{P}}_h}{|\hat{\mathbf{P}}_h \times \mathbf{P}_a| |\hat{\mathbf{P}}_h \times \mathbf{R}|}\end{aligned}\quad (4.2)$$

where  $\mathbf{P}_a$  and  $\mathbf{P}_b$  are the momenta of protons  $a$  and  $b$  respectively.

Also appearing in equation 8.1 is the calculable hard scattering cross section of parton  $a$  scattering off of transversely polarized parton  $b$  into transversely polarized parton  $c$  and parton  $d$ . Parton  $c$  then goes on to fragment into a  $\pi^+\pi^-$  pair keeping a fraction  $z_c$  of quark  $c$ 's momentum as described by  $H_1^\triangleleft$ . The transverse component of  $\mathbf{P}_h$  is written as  $P_T^{\pi^+\pi^-}$ .

Comparing this to the cross section when both initial state quarks are unpolarized we see several similarities.

$$d\sigma_{UU} = 2P_T^{\pi^+\pi^-} \sum_{a,b,c,d} \int \frac{dx_a dx_b}{8\pi^2 z_c} f_1^a(x_a) f_1^b(x_b) \frac{d\hat{\sigma}_{ab \rightarrow cd}}{d\hat{t}} D_1^c(\bar{z}_c, \cos\theta_C, M_C^2) \quad (4.3)$$

As similar as equations 8.1 and 4.3 look, there are some important differences worth noting. Obviously the polarization isn't there since we now are dealing with unpolarized scattering. The sinusoidal modulation has also disappeared. The transversity distribution has turned into a second unpolarized distribution, and the IFF has turned into  $D_1^c$  which is the unpolarized counterpart to the IFF.

The most important thing to mention is that the sine modulation seen in unpolarized-polarized (U-T) scattering is not seen in unpolarized-unpolarized (U-U) scattering. This means that there is a bias to the yield of  $\pi^+\pi^-$  pairs in U-T scattering when compared to U-U scattering. We can observe this by looking at the number of  $\pi^+\pi^-$  pairs at a given value of  $\phi_{RS}$  when the polarization of the proton beam is  $\hat{y}$  vs the number when the polarization is  $-\hat{y}$ . We then normalize by the number we see at that value of  $\phi_{RS}$  for U-U

scattering, which gives the SSA  $A_{UT}$ .

$$A_{UT} \sin(\phi_{RS}) = \frac{1}{|\mathbf{s}_b|} \frac{d\sigma^\uparrow - d\sigma^\downarrow}{d\sigma_{UU}} \quad (4.4)$$

In our experiment we never scatter unpolarized protons, so we have to be clever about the cross section seen in the denominator of equation 4.4. If we sum over the two spin states we are left with the entire unpolarized cross section  $d\sigma^\uparrow + d\sigma^\downarrow = d\sigma_{UU}$ . Using this, equation 4.4 can be rewritten as

$$A_{UT} \sin(\phi_{RS}) = \frac{1}{|\mathbf{s}_b|} \frac{d\sigma^\uparrow - d\sigma^\downarrow}{d\sigma^\uparrow + d\sigma^\downarrow}. \quad (4.5)$$

[cite thesis and papers by Bacchetta also maybe add the jeffe paper and info] This is the only source of a single spin asymmetry at leading twist.[6] It is important to keep this single spin asymmetry differential in many kinematic variables, otherwise it is likely to average to zero[29]. In this analysis the asymmetry will be kept differential in  $M_{inv}^{\pi^+\pi^-}$ ,  $\eta^{\pi^+\pi^-}$ , and  $P_T^{\pi^+\pi^-}$  individually. It will also be kept differential in two of the three variables simultaneously ( $M_{inv}^{\pi^+\pi^-}/P_T^{\pi^+\pi^-}$ ,  $M_{inv}^{\pi^+\pi^-}/\eta^{\pi^+\pi^-}$ , and  $P_T^{\pi^+\pi^-}/\eta^{\pi^+\pi^-}$ ).

Important physics can be seen by performing a partial wave expansion of the cross section[13]. Namely  $\sin \theta H_1^{\triangleleft}$  can be expanded. Looking at the first two terms in the expansion,

$$\begin{aligned} \sin \theta H_1^{\triangleleft c}(\bar{z}_c, \cos \theta, M_{inv}^{\pi^+\pi^-}) &\approx H_{1,ot}^{\triangleleft c}(\bar{z}_c, M_{inv}^{\pi^+\pi^-}) \sin \theta \\ &+ H_{1,lt}^{\triangleleft c}(\bar{z}_c, M_{inv}^{\pi^+\pi^-}) \sin \theta \cos \theta \end{aligned} \quad (4.6)$$

The first term, S/P wave interference, is due to the interference between amplitudes for a decay into an  $L = 0$   $\pi^+\pi^-$  pair and an  $L = 1$  transversely polarized  $\pi^+\pi^-$  pair. The second term, P/P wave interference, is due to the interference between amplitudes for a decay into an  $L = 1$   $\pi^+\pi^-$  pair and an  $L = 1$  transversely polarized  $\pi^+\pi^-$  pair. The  $L = 1$

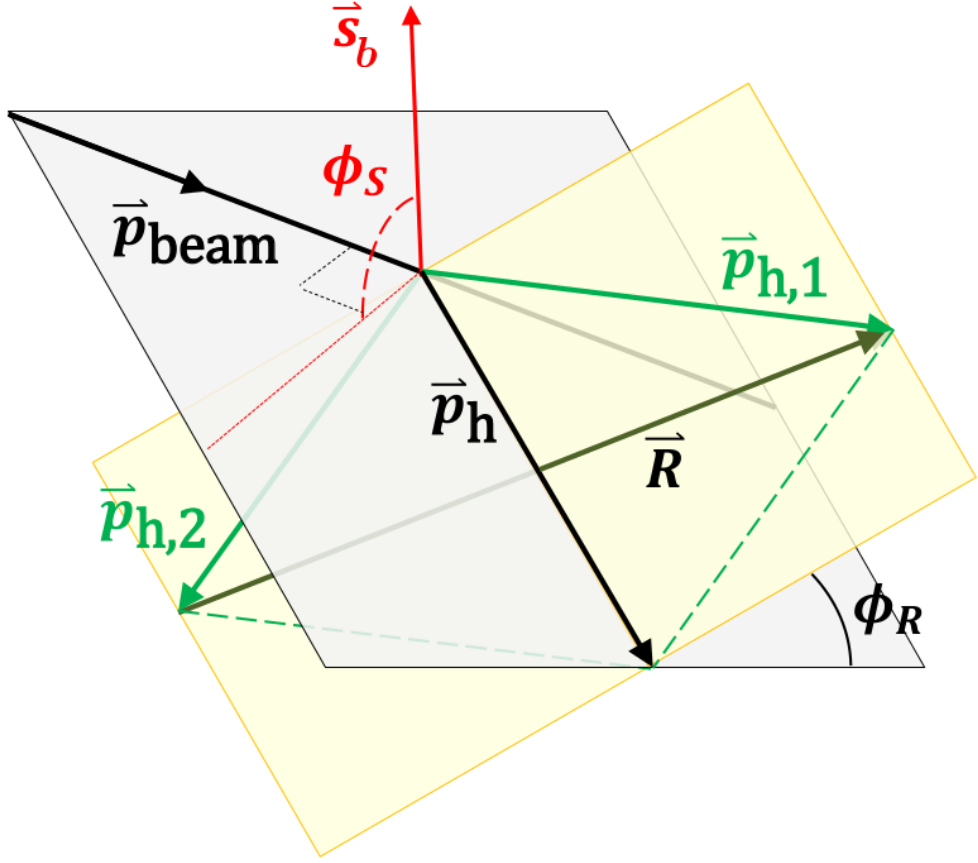


Figure 4.1: Visual representation of angles  $\phi_R$  and  $\phi_S$ .  $\phi_{RS} = \phi_R - \phi_S$

$\vec{p}_{h,1}$  is the momentum of the positive hadron while  $\vec{p}_{h,2}$  is the momentum of the negative hadron.

contributions comes from a  $\pi^+\pi^-$  pair that went through a spin-1 intermediate state. One such intermediary we have the ability and statistics to look for is the  $\rho$  meson. We expect there to be an enhancement in the IFF, and thus the asymmetry, in the invariant mass region of the  $\rho$  (770 MeV). [6, 44]

## 5 2006 analysis and sim

The 2006 data set gave us the first glimpse of this asymmetry. The analysis of the 2006 data set was done by Anselm Vossen. The 2006 run had only a small integrated luminosity of 200 GeV transverse proton proton collisions. Due to this, the data set was small and the asymmetry couldn't be investigated as closely as was wanted.

Figure 5.1 shows the asymmetry as a function of the pion pair invariant mass. As hinted from the theory there is an increase in the asymmetry around the  $\rho$  meson mass for both forward and backward pairs.

Varying the opening angle of the pion pair grants access to the  $z$  dependence of the asymmetry. The fraction of the fragmenting quark momentum the pion pair retains,  $z$ , influences the size of the IFF. It turns out the asymmetry increases as the opening angle decreases as seen in figure 5.2.

As stated previously,  $\eta^{\pi^+\pi^-}$  acts as a stand in for the momentum fraction of the polarized parton, as a larger partonic momentum fraction will cause the pion pair to be produced in a more forward direction. The asymmetry is plotted as a function of  $\eta^{\pi^+\pi^-}$  in figure 5.3. As one might expect, the asymmetry is larger the more forward the pion pair is. This is explained by the fact that more forward pairs result from polarized partons with larger momentum fractions allowing for a larger spin transfer.

A supplemental analysis was done on simulated data to investigate partonic momentum

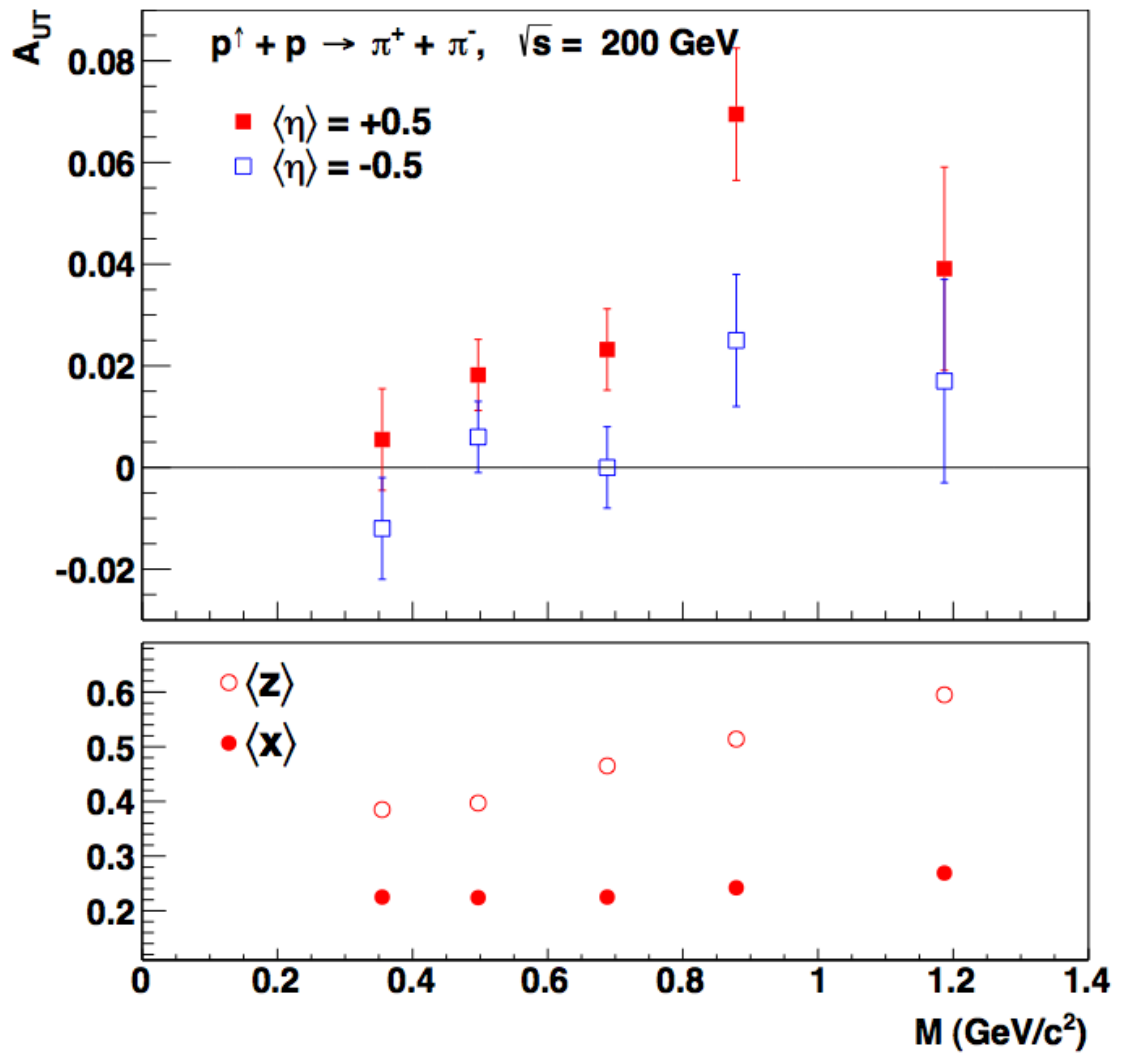


Figure 5.1: Asymmetry versus invariant mass of the  $\pi^+\pi^-$  pair for the 2006 data set for pairs scattering in the forward direction (red) and in the backward direction (blue).

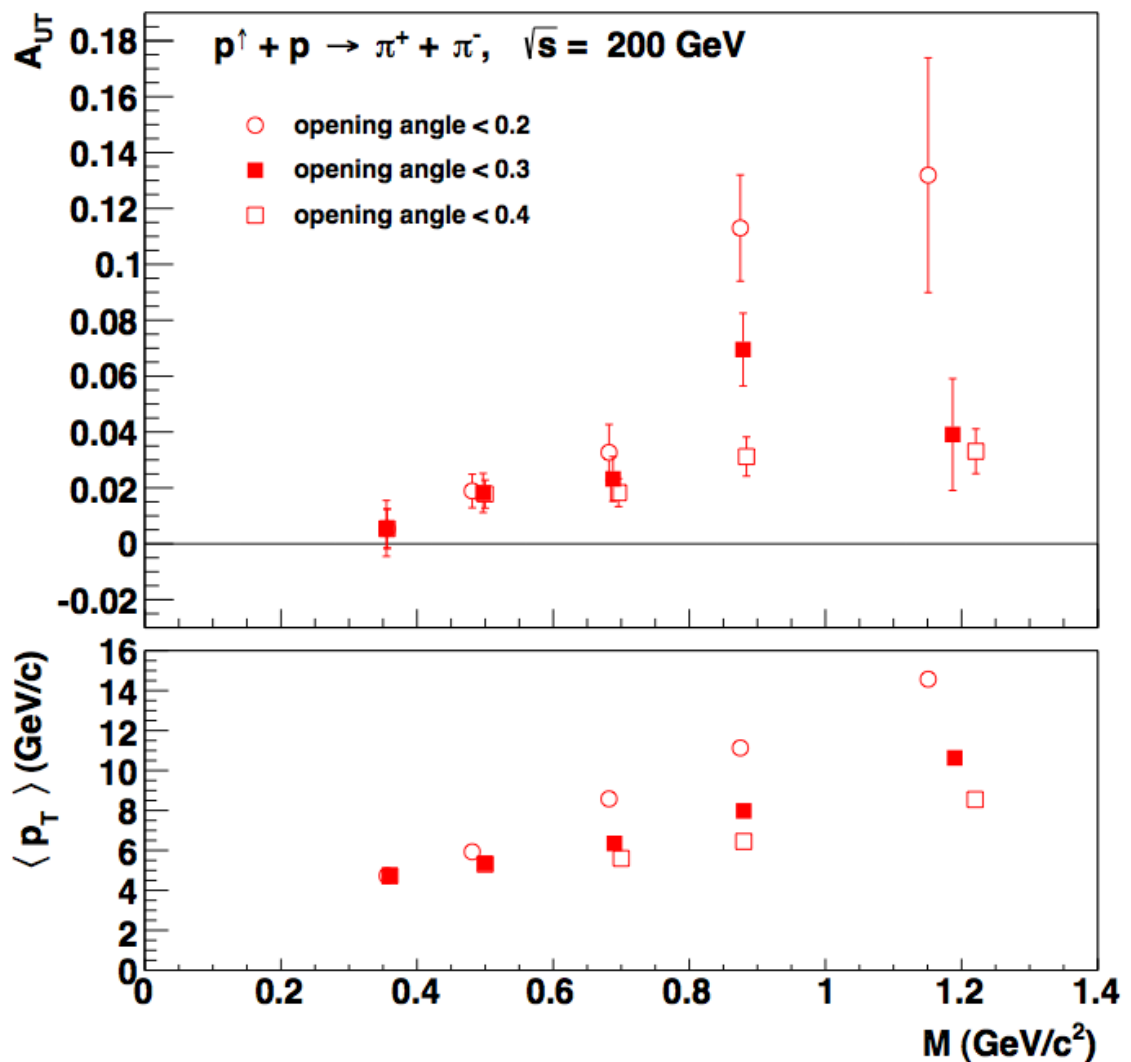


Figure 5.2: Asymmetry versus invariant mass of the  $\pi^+\pi^-$  pair for the 2006 data set for different opening angles of pairs are scattered into the forward direction.

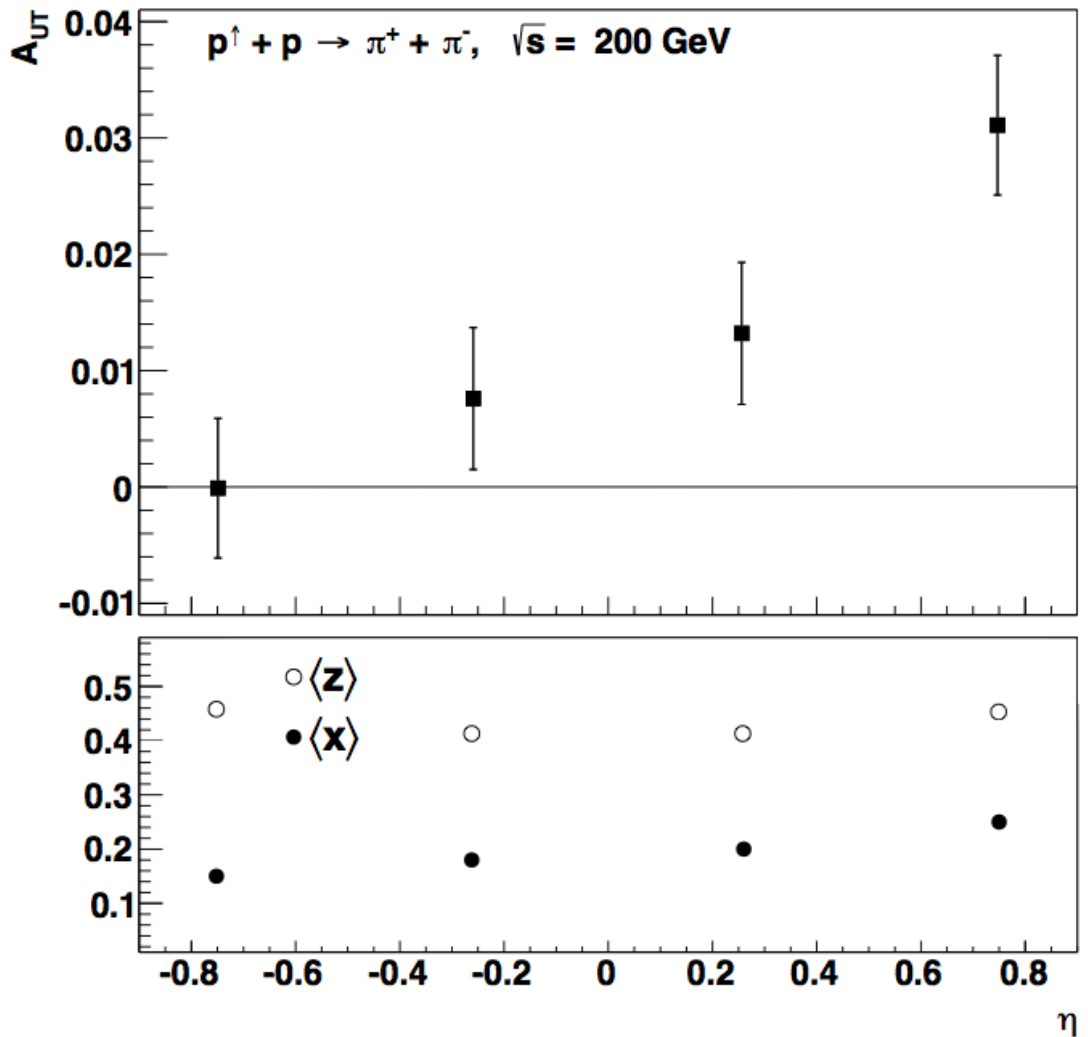


Figure 5.3: Asymmetry versus  $\eta^{\pi^+\pi^-}$  for the 2006 data set

fractions as well as biases introduced by STAR triggers. Figure 5.4 shows the momentum fraction of the fragmenting quark for pairs in the forward and reverse directions. A more in depth discussion for the analysis on the simulated data is given in chapters 10 and ??

These results are the first sign of nonzero asymmetries in  $\pi^+\pi^-$  pair correlation in polarized proton collisions. More can be read about the 2006 study in reference [3].

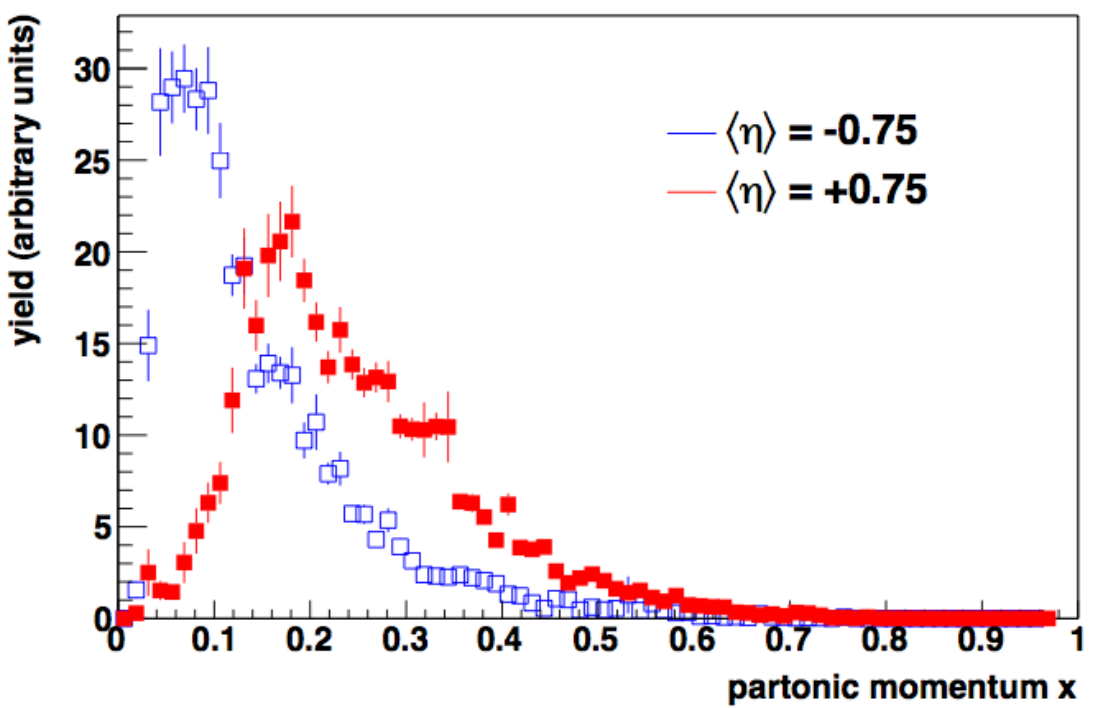


Figure 5.4: Partonic momentum fraction  $x$  for the parton from the polarized proton in the forward (red) and backward (blue) direction

# 6 2012 IFF

## 6.1 Data Set, Triggers, and Cuts

The runs from the 2012 production that passed quality tests and are eligible to be used in the analysis are listed in the table bellow.

13044126	13045001	13045003	13045005	13045006	13045007	13045012	13045029
13045056	13045133	13045134	13045135	13045138	13045145	13045146	13045164
13046001	13046002	13046003	13046004	13046011	13046012	13046013	13046014
13046015	13046017	13046121	13047003	13047004	13047022	13047023	13047024
13047026	13047027	13047028	13047029	13047030	13047031	13047032	13047033
13047034	13047035	13048010	13048011	13048012	13048013	13048014	13048015
13048016	13048017	13048018	13048019	13048030	13048031	13048032	13048040
13048041	13048042	13048043	13048044	13048045	13048046	13048049	13048050
13048051	13048052	13048053	13048087	13048088	13048089	13048090	13048091
13048092	13048093	13049031	13049032	13049035	13049039	13049041	13049042
13049044	13049045	13049046	13049047	13049048	13049049	13049050	13049072
13049073	13049080	13049081	13049082	13049089	13049093	13049094	13049096
13049098	13049099	13049101	13050001	13050007	13050009	13050011	13050012
13050015	13050016	13050020	13050022	13050023	13050028	13050029	13050031
13050032	13050033	13050036	13050037	13050038	13050039	13050041	13050043
13050044	13050046	13050047	13050049	13050050	13051011	13051012	13051015
13051016	13051017	13051019	13051020	13051021	13051022	13051023	13051024
13051026	13051028	13051074	13051080	13051081	13051083	13051085	13051086
13051087	13051088	13051092	13051093	13051095	13052001	13052002	13052003
13052004	13052005	13052009	13052010	13052011	13052012	13052013	13052014
13052015	13052016	13052017	13052018	13052020	13052021	13052022	13052037
13052039	13052042	13052043	13052045	13052048	13052050	13052051	13052052
13052053	13052054	13052056	13052088	13053004	13053005	13053006	13053007
13053012	13053013	13053015	13053027	13053028	13054022	13054023	13054044
13054045	13054060	13054061	13054062	13054063	13054064	13054065	13054066
13054068	13054069	13054084	13054085	13055004	13055006	13055007	13055008
13055009	13055010	13055011	13055014	13055016	13055017	13055018	13055019
13055020	13055021	13055022	13055023	13055024	13055035	13055036	13055037
13055038	13055039	13055068	13055070	13055072	13055075	13055076	13055080
13055081	13055082	13055086	13055087	13056005	13056007	13056008	13056020

13056021	13056022	13056023	13056024	13056025	13056026	13056027	13056028
13056029	13056030	13056031	13056033	13056034	13056035	13056037	13056038
13056039	13057011	13057014	13057015	13057016	13057017	13057018	13057019
13057021	13057022	13057023	13057024	13057025	13057026	13057027	13057044
13057045	13057046	13057047	13057048	13057049	13057050	13057051	13057052
13057053	13057055	13057056	13057057	13057058	13058002	13058015	13058016
13058017	13058018	13058025	13058026	13058028	13058029	13058030	13058031
13059084	13060010	13061024	13061025	13061026	13061030	13061031	13061035
13061054	13061055	13061059	13061060	13061061	13062001	13062002	13062004
13062005	13062006	13062007	13062013	13062025	13062026	13062028	13062029
13062049	13062050	13062052	13062059	13062060	13062061	13062062	13062063
13063009	13063010	13063011	13063020	13063022	13063023	13063030	13063031
13063032	13063033	13063034	13063035	13063036	13063053	13063054	13063062
13063063	13063065	13063067	13063068	13063071	13063072	13063073	13063074
13063076	13064001	13064002	13064003	13064004	13064005	13064006	13064012
13064014	13064020	13064021	13064022	13064023	13064024	13064025	13064026
13064028	13064029	13064030	13064031	13064032	13064052	13064055	13064056
13064057	13064059	13064061	13064064	13064065	13064066	13064068	13064070
13064074	13064075	13065005	13065006	13065007	13065008	13065009	13065013
13065014	13065015	13065016	13065017	13065018	13065019	13065020	13065021
13065022	13065047	13065048	13065049	13065050	13065052	13065053	13065055
13065056	13065058	13065059	13065060	13066021	13066022	13066023	13066024
13066025	13066026	13066027	13066028	13066029	13066030	13066031	13066033
13066034	13066035	13066036	13068084	13068088	13068090	13069001	13069002
13069003	13069004	13069005	13069006	13069007	13069014	13069016	13069017
13069018	13069020	13069021	13069022	13069023	13069024	13069026	13069027
13069029	13069030	13069031	13069035	13069036	13069066	13069067	13069068
13069069	13069073	13070006	13070008	13070010	13070011	13070012	13070014
13070015	13070016	13070017	13070018	13070019	13070020	13070021	13070022
13070024	13070025	13070026	13070027	13071009	13071010	13071011	13071012
13072006	13072014	13072015	13072016	13072017	13072018	13072019	13072020

From these runs, events were selected which triggered at least one of the following STAR triggers of interest: JP0, JP1, JP2, AJP, BHT0VPD, BHT1VPD, BHT2BBC, or BHT2. These were chosen because they were most similar to the triggers used to select events in the 2006 analysis, thus allowing for a proper comparison of the results.

Tracks from these triggered events were then scrutinized. As the BEMC only covers a finite range in  $\eta$ , tracks at pseudorapidity above 2 and below  $-2$  were rejected. To ensure good track resolution in the TPC necessary for particle identification, tracks with less than five fit points were also rejected. Since different trajectories in the TPC offer a

different number of possible fit points, tracks are also required to have at least half of the possible fit points. The position of the vertex the track originated is required to be less than 60 cm from the center of the star detector. This helps the detector reconstruct the correct kinematic location of the particle. The track is also required to have a transverse momentum larger than  $1.5 \text{ GeV}/c$ . If a track possesses all the required attributes, it is then considered for the analysis.

## 6.2 Particle Identification and Contamination

Once a track is selected for the analysis, the particle creating the track needs to be identified. As charged particles traverse the TPC, they deposit energy in the TPC gas. This energy loss is different for different particles. A value,  $n_\sigma(\pi)$ , is given to each track in an event describing how many standard deviations away it is from an ideal pion on the ionization energy loss curve shown in figure 6.1; the ideal curves shown as black lines. Each track is also given values of  $n_\sigma(p)$ ,  $n_\sigma(k)$ , and  $n_\sigma(e)$  describing how close it is to ideal protons, kaons, and electrons. For example if a track has an  $n_\sigma(\pi)$  value of zero, it is very likely a pion and should be included in the analysis.

If the data set strictly contained pions, the  $n_\sigma(\pi)$  distribution would be gaussian centered around zero. However as seen in figure 6.2 it is not exactly gaussian. Although it looks gaussian near  $n_\sigma(\pi) = 0$ , there is a clear shoulder on the left side due to kaon and proton contamination and a much less observable shoulder to the right from electron contamination. To account for this contamination we fit the  $n_\sigma(\pi)$  distribution with a 5-gaussian fit; one gaussian for each particle species plus one gaussian to account for the tail at high  $n_\sigma(\pi)$  most likely due to pile up or merged tracks.

Several of the degrees of freedom of the fit can be constrained for physical reasons. First the expected  $n_\sigma(\pi)$  value of an ideal kaon can be readily found from fitting a plot of  $n_\sigma(\pi)$

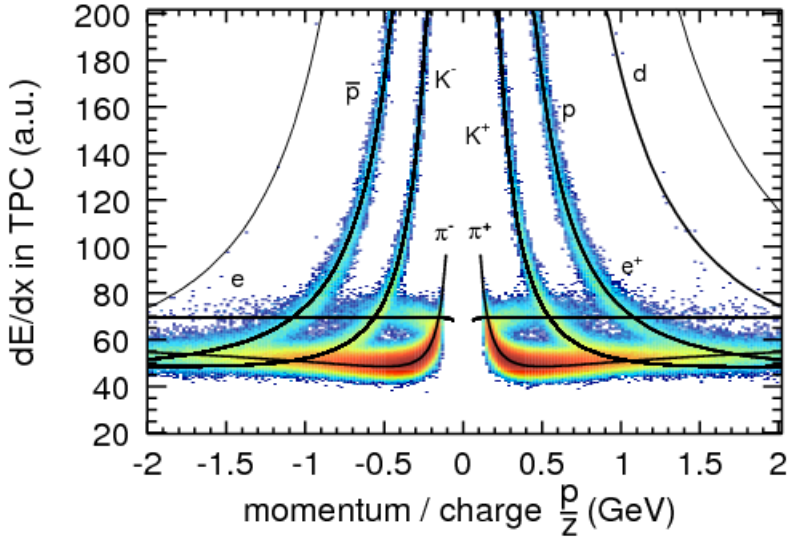


Figure 6.1: Ionization energy loss as a function of particle momentum divided by electric charge for TPC tracks

vs  $n_\sigma(k)$  as in figure 6.3. The separation between the pion and kaon gaussians in the 5-gaussian fit is required to be equal to the value of  $n_\sigma(\pi)$  at  $n_\sigma(k) = 0$ . This is repeated to constrain the separation between the pion and proton gaussians as well as the separation between the pion and electron gaussians. Secondly kaons and protons are required to have the same width. Third the “pile up” gaussian is required to have a smaller amplitude and be located at a larger  $n_\sigma(\pi)$  than the electron gaussian. This is to make sure it actually does fit the high  $n_\sigma(\pi)$  tail. This tail is more prominent at higher track momentum but is sometimes absent at lower momentum.

Armed with this fitting procedure, the location and amount of each particle species becomes clear (figure 6.4). A clean sample of pions can be found by selecting tracks with an  $n_\sigma(\pi)$  between  $-1$  and  $2.5$ . This choice maximizes the number of pions included in the analysis while not compromising the purity of the pion sample too much.

When interpreting the asymmetry results, it is important to quantify the pion purity of

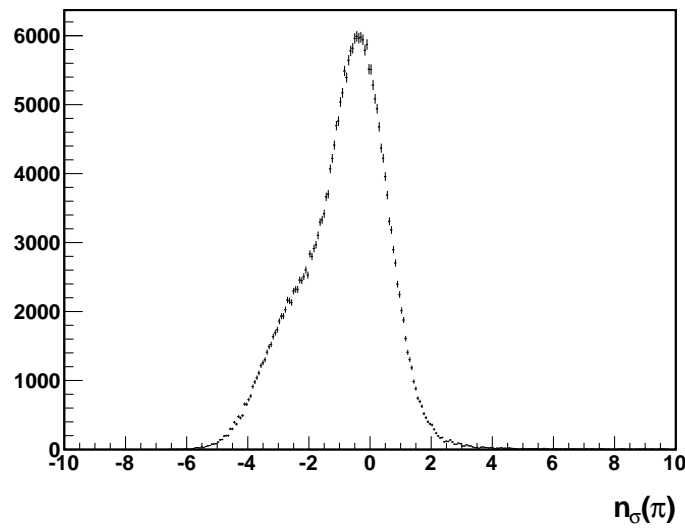


Figure 6.2:  $n_\sigma(\pi)$  distribution of TCP tracks

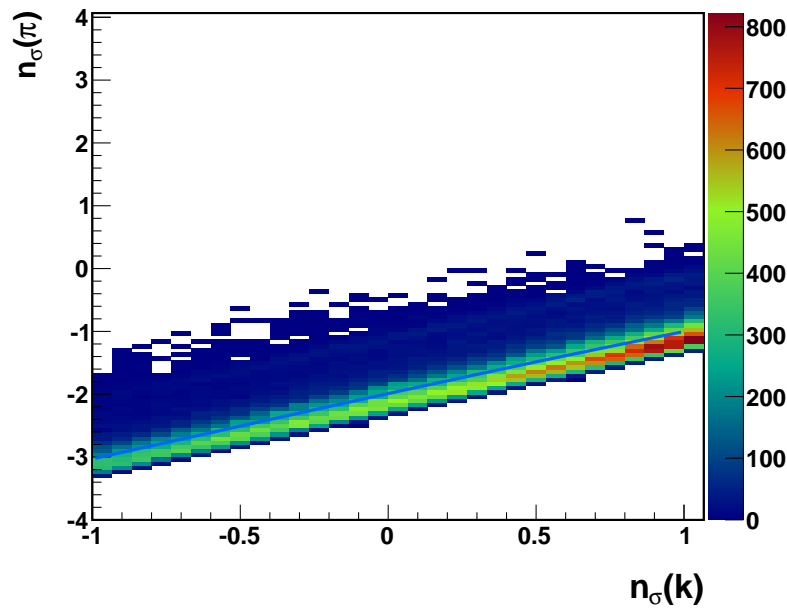


Figure 6.3:  $n_\sigma(\pi)$  versus  $n_\sigma(k)$ . The blue line is a 3rd order polynomial fit of the profile.

The  $n_\sigma(\pi)$  value at  $n_\sigma(k) = 0$  is taken as the separation between the pion gaussian and the kaon gaussian in the 5-gaussian fit.

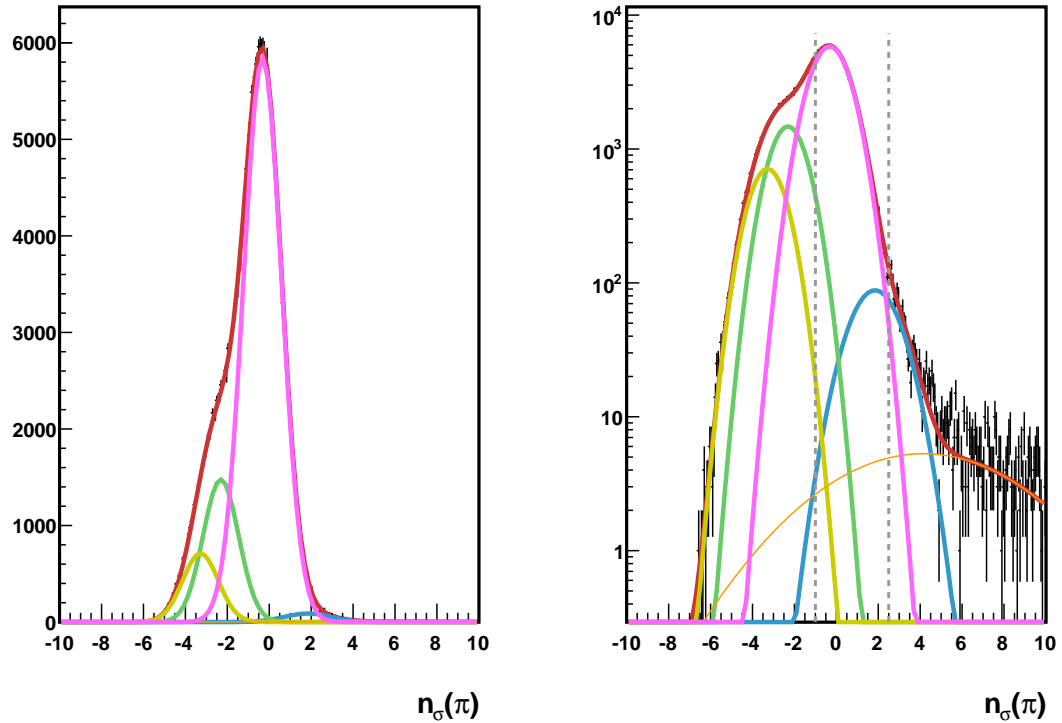


Figure 6.4: 5-gaussian fit of  $n_\sigma(\pi)$  distribution. The pion peak is shown in pink, the kaon peak in green, the proton peak in yellow, the electron peak in blue, and the pile up peak in orange. Right panel is a log scale for better visibility of smaller peaks. The red line is the sum of all gaussian fits and matches the histogram almost perfectly. The dashed lines indicate the  $-1 < n_\sigma(\pi) < 2.5$  range chosen for the analysis.

the data. As the ionization energy loss curves show (figure 6.1), the energy loss depends on track momentum. More importantly, each particle species displays a different energy loss behavior. Some of these energy loss curves even cross each other at track momentum between 1 and 2  $GeV/c$  making it hard to determine the contamination of the pion data set all at once. Instead the data set is broken into 5 bins in track momentum and 5 in detector  $\theta$  (the polar angle measured with respect to the beam direction). In each of these bins, the 5-gaussian fitting procedure is repeated. The 5 gaussian fits are shown in figures 6.5 to 6.9. For the four highest track momentum bins, the pion fraction is calculated by integrating the pion gaussian from  $n_\sigma(\pi) = -1$  to  $n_\sigma(\pi) = 2.5$  and dividing by the integral of the total fit in the same range. As seen in figure 6.1, the proton and pion energy loss curves start to overlap in the smallest track momentum bin used ( $1.5 \text{ GeV}/c < p < 2.04 \text{ GeV}/c$ ). This prohibits an accurate determination of the pion fraction using the same method. Luckily in this low momentum range, the time of flight can accurately distinguish protons and pions very easily. Using the ToF, the particle mass may be detected. A two dimensional histogram of  $M^2$  and  $n_\sigma(\pi)$  shown in figure 6.10 shows how the protons are distinguished from pions. Any particle above the red line is taken to be a proton. The proton fraction is then computed by dividing the number of tracks above the red line by the total number of tracks. The kaon, electron, and pile up fractions can still be computed from integrating the 5-gaussian fits, and the pion fraction is determined by the relationship:  $1 - F_k - F_p - F_e - F_{pile-up} = F_\pi$ .

Since the actual asymmetry analysis is binned in pion pair transverse momentum, invariant mass, and pseudorapidity, we need to find pion fractions for these bins. These purity fractions were computed from the known pion fractions found in the track momentum and detector  $\theta$  bins using a weighted mean. The purity values for the analysis binning can be found in tables 6.2 and 6.3.

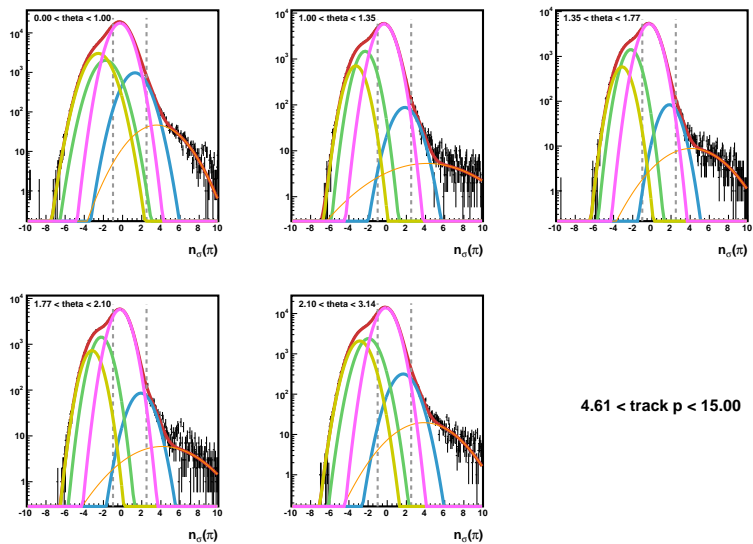


Figure 6.5

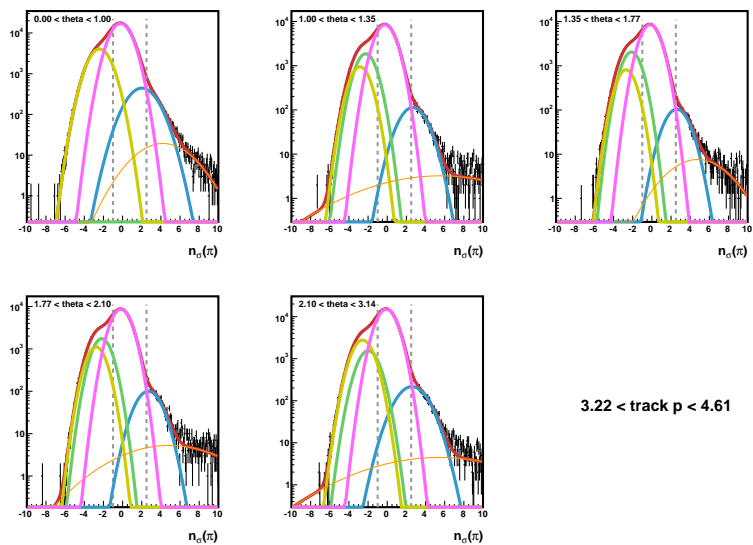


Figure 6.6

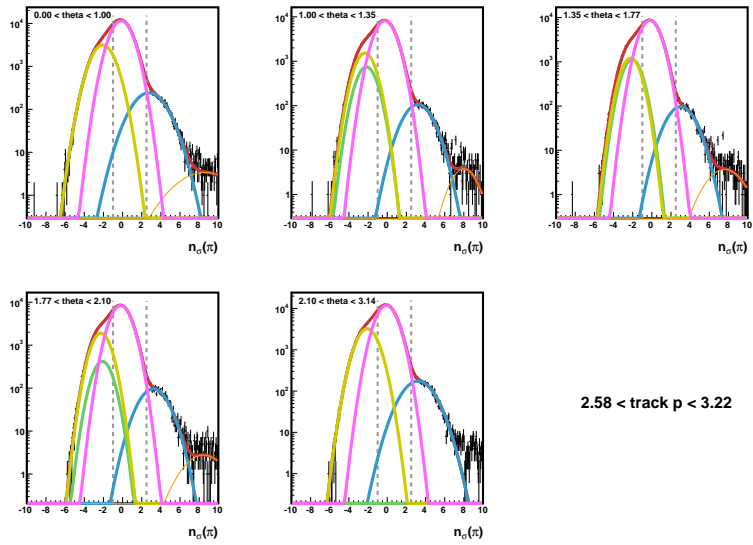


Figure 6.7

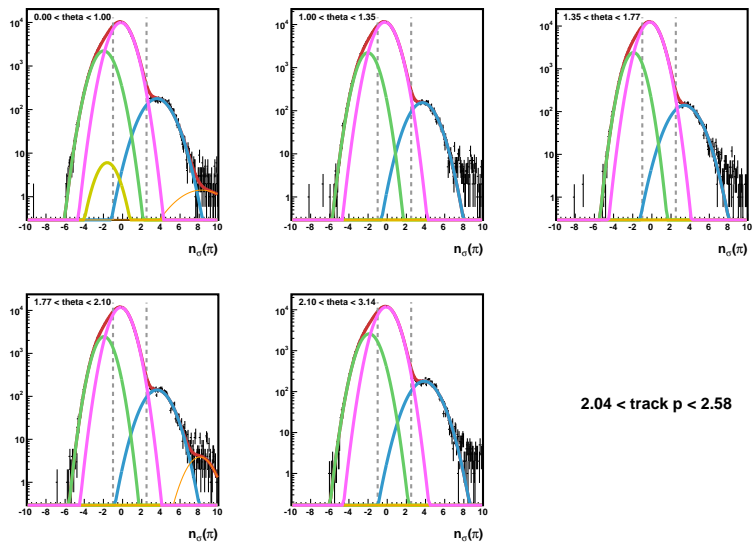


Figure 6.8

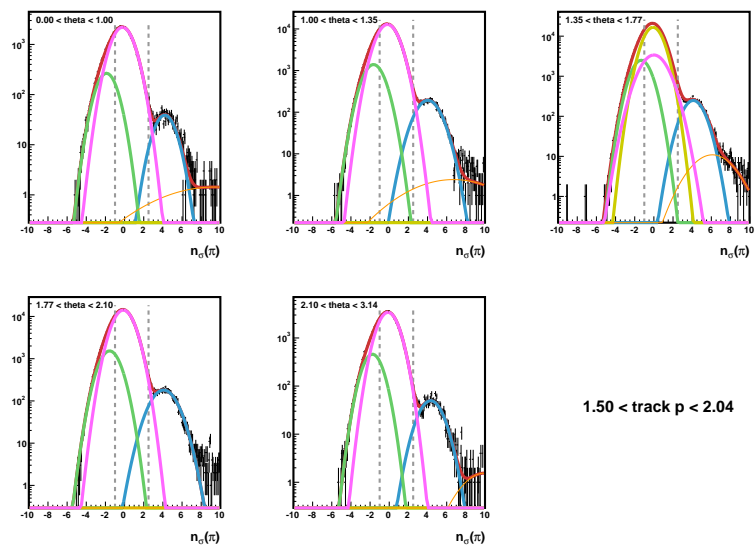


Figure 6.9

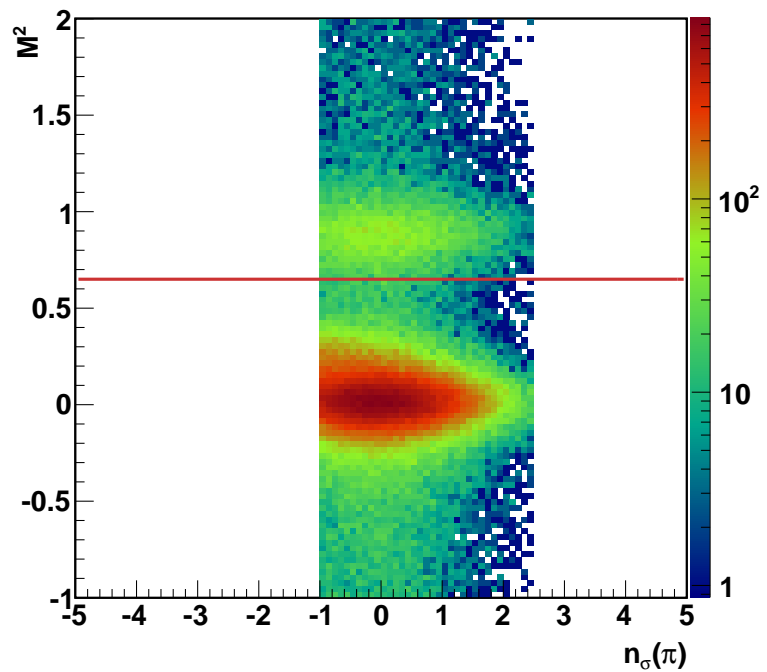


Figure 6.10

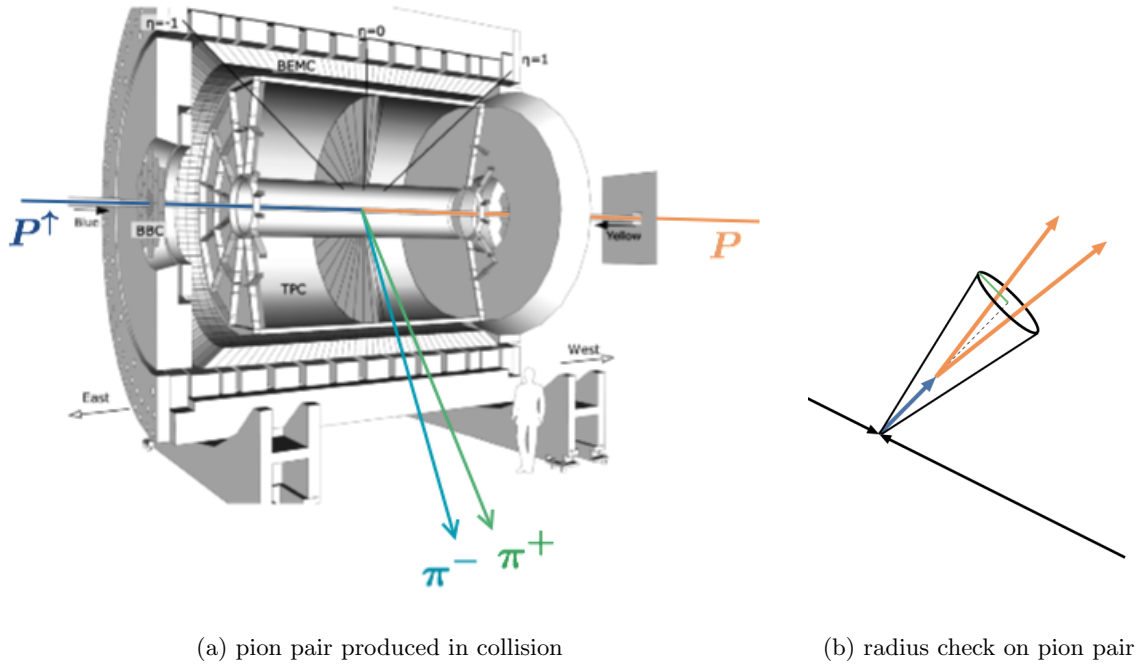
Table 6.2: pion purity for 1D binning

$\eta^{\pi^+\pi^-}$	pion %	$M_{inv}^{\pi^+\pi^-}$	pion %	$\eta^{\pi^+\pi^-}$	pion %
-2.00 – -0.60	95	0.00 – 0.38	94	3.00 – 3.70	93
-0.60 – -0.30	95	0.38 – 0.44	94	3.70 – 4.15	95
-0.30 – 0.00	95	0.44 – 0.50	94	4.15 – 4.63	95
0.00 – 0.40	95	0.50 – 0.56	94	4.63 – 5.19	95
0.40 – 0.75	95	0.56 – 0.62	95	5.19 – 5.87	95
0.75 – 2.00	92	0.62 – 0.72	95	5.87 – 6.80	95
		0.72 – 0.86	95	6.80 – 7.80	94
		0.86 – 1.10	94	7.80 – 10.00	94
		1.10 – 100	94	10.00 – 50.00	94

Table 6.3: pion purity for 2D binning

$M_{inv}^{\pi^+\pi^-}$	$\eta^{\pi^+\pi^-}$	pion %	$M_{inv}^{\pi^+\pi^-}$	$P_T^{\pi^+\pi^-}$	pion %	$P_T^{\pi^+\pi^-}$	$\eta^{\pi^+\pi^-}$	pion %
0.00 – 0.40	-2.00 – -0.50	96	3.00 – 4.00	0.00 – 0.40	94	3.00 – 4.00	-2.00 – -0.50	95
0.00 – 0.40	-0.50 – 0.00	94	3.00 – 4.00	0.40 – 0.60	94	3.00 – 4.00	-0.50 – 0.00	93
0.00 – 0.40	0.00 – 0.50	94	3.00 – 4.00	0.60 – 0.80	94	3.00 – 4.00	0.00 – 0.50	93
0.00 – 0.40	0.50 – 2.00	94	3.00 – 4.00	0.80 – 1.00	94	3.00 – 4.00	0.50 – 2.00	94
0.40 – 0.60	-2.00 – -0.50	96	3.00 – 4.00	1.00 – 100.50	94	4.00 – 5.00	-2.00 – -0.50	96
0.40 – 0.60	-0.50 – 0.00	94	4.00 – 5.00	0.00 – 0.40	94	4.00 – 5.00	-0.50 – 0.00	95
0.40 – 0.60	0.00 – 0.50	94	4.00 – 5.00	0.40 – 0.60	94	4.00 – 5.00	0.00 – 0.50	94
0.40 – 0.60	0.50 – 2.00	94	4.00 – 5.00	0.60 – 0.80	94	4.00 – 5.00	0.50 – 2.00	94
0.60 – 0.80	-2.00 – -0.50	96	4.00 – 5.00	0.80 – 1.00	94	5.00 – 6.50	-2.00 – -0.50	96
0.60 – 0.80	-0.50 – 0.00	94	4.00 – 5.00	1.00 – 100.50	94	5.00 – 6.50	-0.50 – 0.00	95
0.60 – 0.80	0.00 – 0.50	94	5.00 – 6.50	0.00 – 0.40	95	5.00 – 6.50	0.00 – 0.50	94
0.60 – 0.80	0.50 – 2.00	94	5.00 – 6.50	0.40 – 0.60	94	5.00 – 6.50	0.50 – 2.00	94
0.80 – 1.00	-2.00 – -0.50	96	5.00 – 6.50	0.60 – 0.80	94	6.50 – 8.00	-2.00 – -0.50	96
0.80 – 1.00	-0.50 – 0.00	94	5.00 – 6.50	0.80 – 1.00	94	6.50 – 8.00	-0.50 – 0.00	94
0.80 – 1.00	0.00 – 0.50	94	5.00 – 6.50	1.00 – 100.50	94	6.50 – 8.00	0.00 – 0.50	94
0.80 – 1.00	0.50 – 2.00	94	6.50 – 8.00	0.00 – 0.40	94	6.50 – 8.00	0.50 – 2.00	94
1.00 – 100.50	-2.00 – -0.50	96	6.50 – 8.00	0.40 – 0.60	94	8.00 – 50.00	-2.00 – -0.50	95
1.00 – 100.50	-0.50 – 0.00	95	6.50 – 8.00	0.60 – 0.80	94	8.00 – 50.00	-0.50 – 0.00	94
1.00 – 100.50	0.00 – 0.50	94	6.50 – 8.00	0.80 – 1.00	94	8.00 – 50.00	0.00 – 0.50	93
1.00 – 100.50	0.50 – 2.00	94	6.50 – 8.00	1.00 – 100.50	94	8.00 – 50.00	0.50 – 2.00	94
			8.00 – 50.00	0.00 – 0.40	94			
			8.00 – 50.00	0.40 – 0.60	94			
			8.00 – 50.00	0.60 – 0.80	94			
			8.00 – 50.00	0.80 – 1.00	94			
			8.00 – 50.00	1.00 – 100.50	94			

Figure 6.11: Schematic of Analysis



### 6.3 Finding $\pi^+\pi^-$ Pairs

Once a clean pion sample is found,  $\pi^+$ s and  $\pi^-$ s must be combined into  $\pi^+\pi^-$  pairs. An example of an event of interest can be seen in figure 6.12a. Here we see a positively charged pion and negatively charged pion produced in close proximity by the proton collision. This is what we refer to as a pion pair. Every combination of  $\pi^+$  and  $\pi^-$  in an event are checked. Since the two pions are required to be from the same fragmenting quark, they are taken as a pair and used in the analysis if they pass the individual track cuts and if they are contained in a cone of a certain radius in  $\eta - \phi$  space (figure 6.12b). For 1D binning, radii of 0.2, 0.3, and 0.4 are used, while 0.7 is used in 2D binning in order to increase statistics. Even the largest of these radii should ensure the two pions are from the same fragmenting quark.

## 6.4 Pair Distributions

The entire data set provides 17544516  $\pi^+\pi^-$  pairs in a radius between 0.05 and 1.0 in  $\eta, \phi$  space before trigger information is used. The minimum radius cut of 0.05 is used because when the tracks are very close together, the uncertainty in track position can cause the orientation of the pairs to flip. Since the orientation of the pair is so important to the observed asymmetry, this is unacceptable for our analysis.

Once the data set was ready, quality tests were preformed on the pion pairs. These included looking at the invariant mass, transverse momentum, and pseudorapidity distributions for the pairs. Quality control plots of relevant kinematic variables of individual pions and pion pairs with a maximum radius of 0.3 can be seen in figures 6.12 to 6.29.

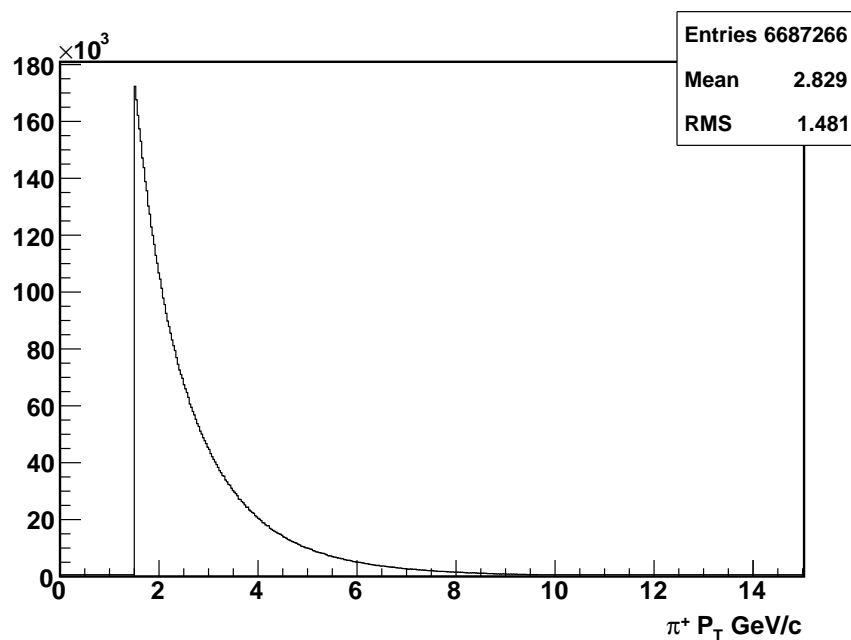


Figure 6.12:  $P_T$  distribution of  $\pi^+$

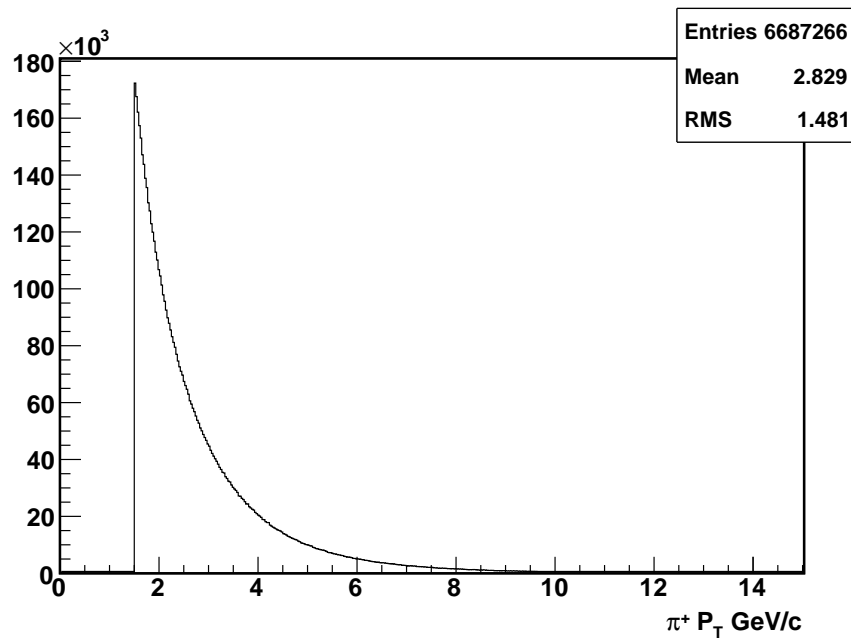


Figure 6.13:  $P_T$  distribution of  $\pi^-$

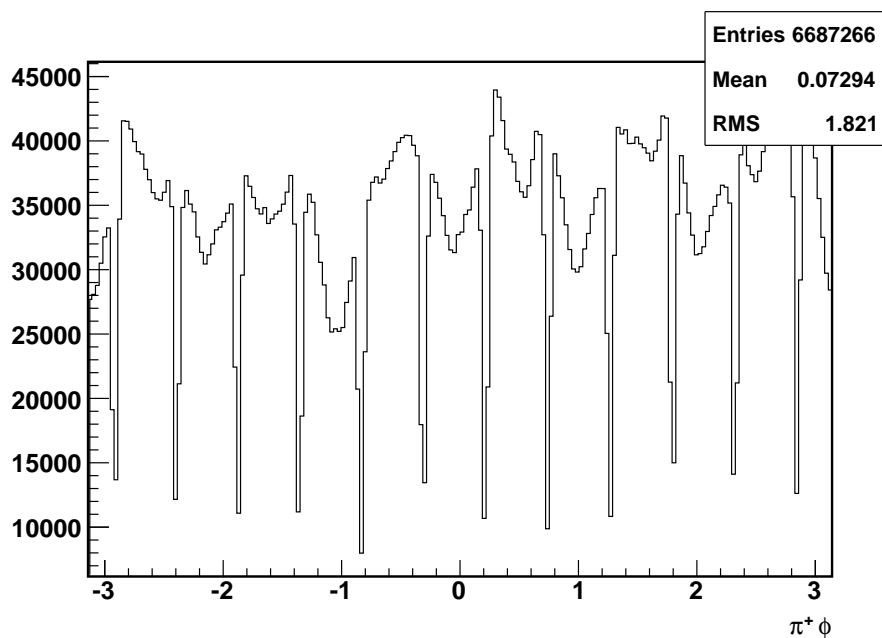


Figure 6.14:  $\phi$  distribution of  $\pi^+$

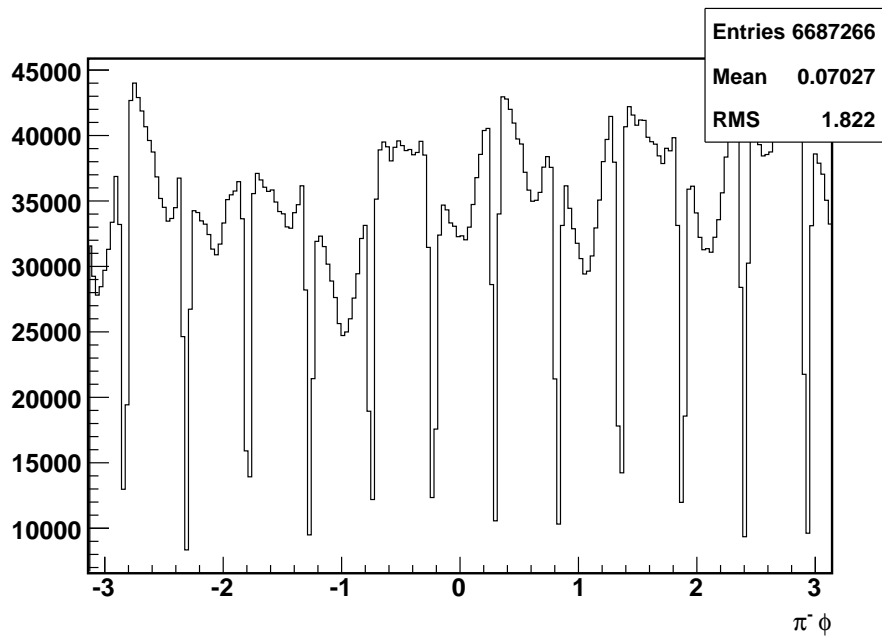


Figure 6.15:  $\phi$  distribution of  $\pi^-$

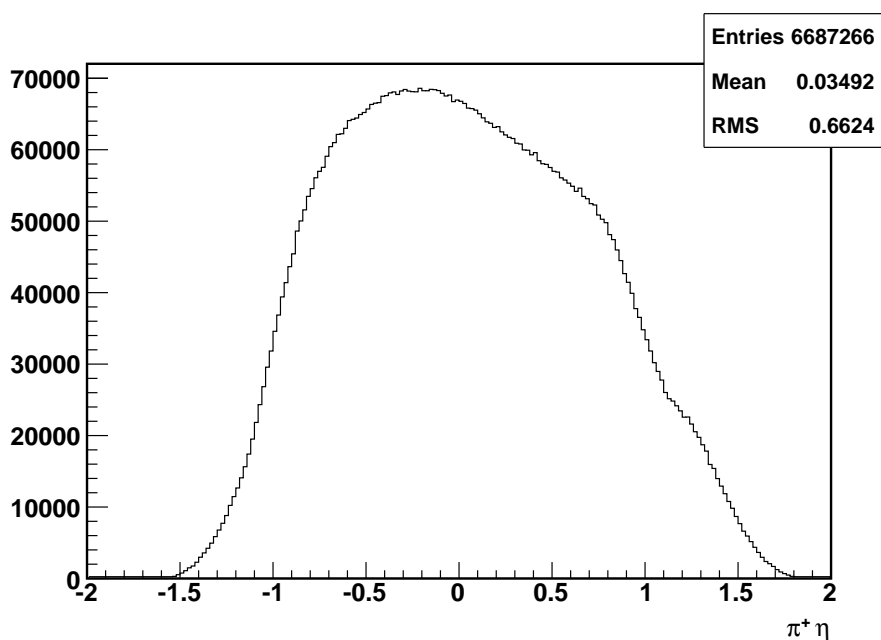


Figure 6.16:  $\eta$  distribution of  $\pi^+$

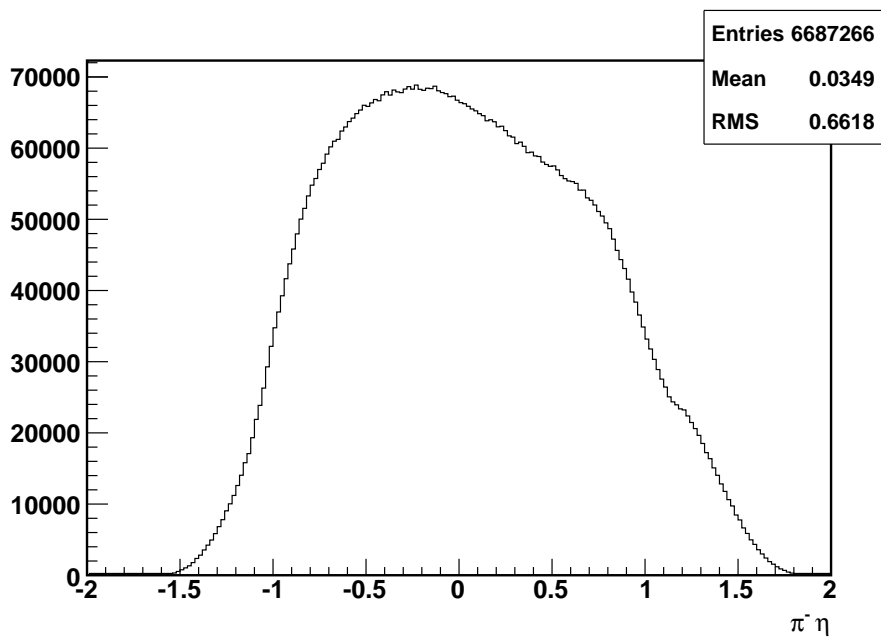


Figure 6.17:  $\eta$  distribution of  $\pi^-$

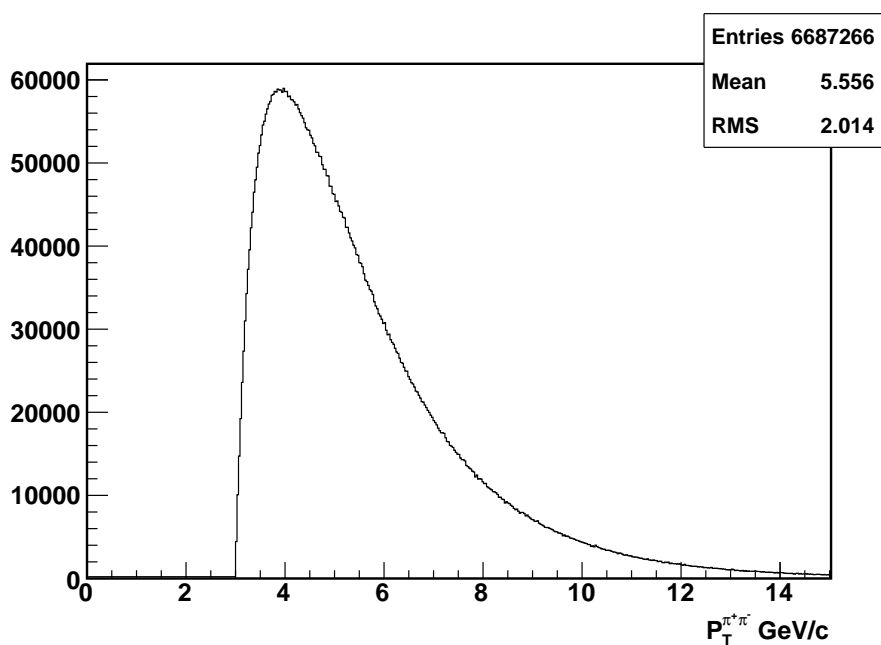


Figure 6.18:  $P_T$  distribution of  $\pi^+\pi^-$  pair

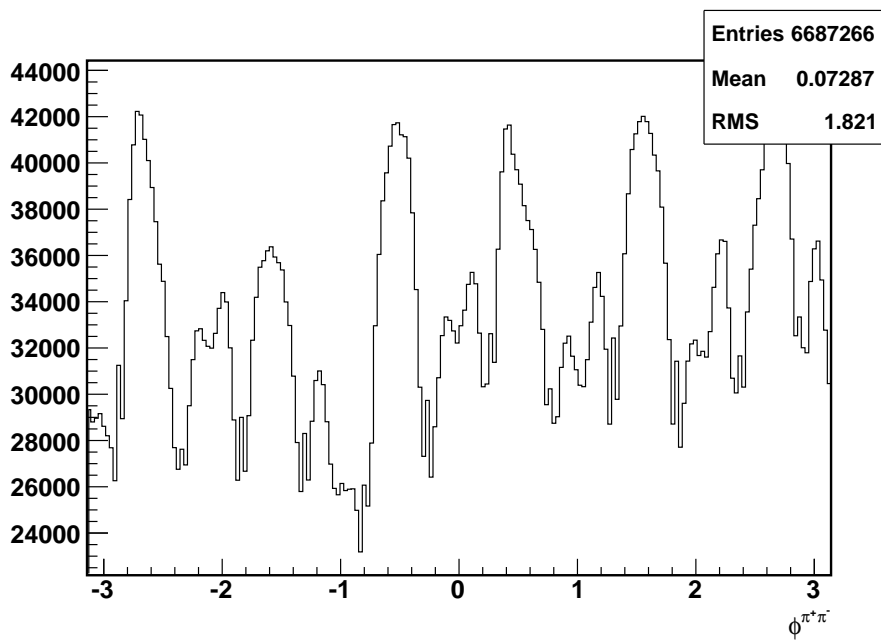


Figure 6.19:  $\phi$  distribution of  $\pi^+\pi^-$  pair

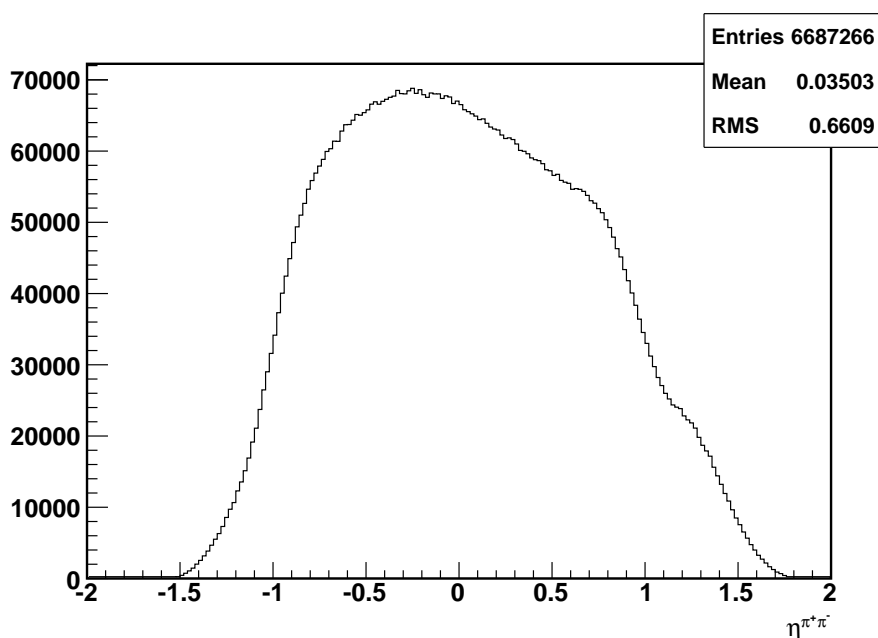


Figure 6.20:  $\eta$  distribution of  $\pi^+\pi^-$  pair

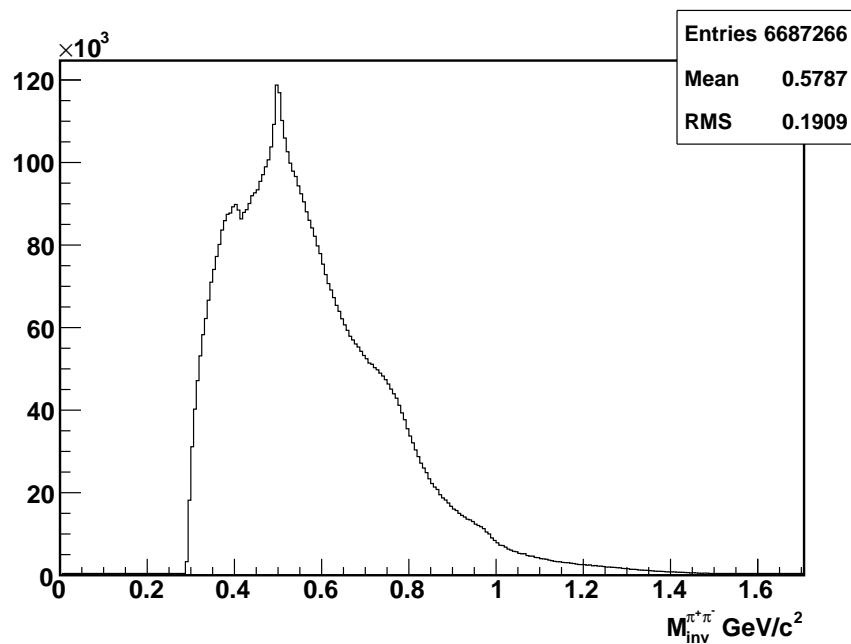


Figure 6.21: Invariant mass distribution of  $\pi^+\pi^-$  pair

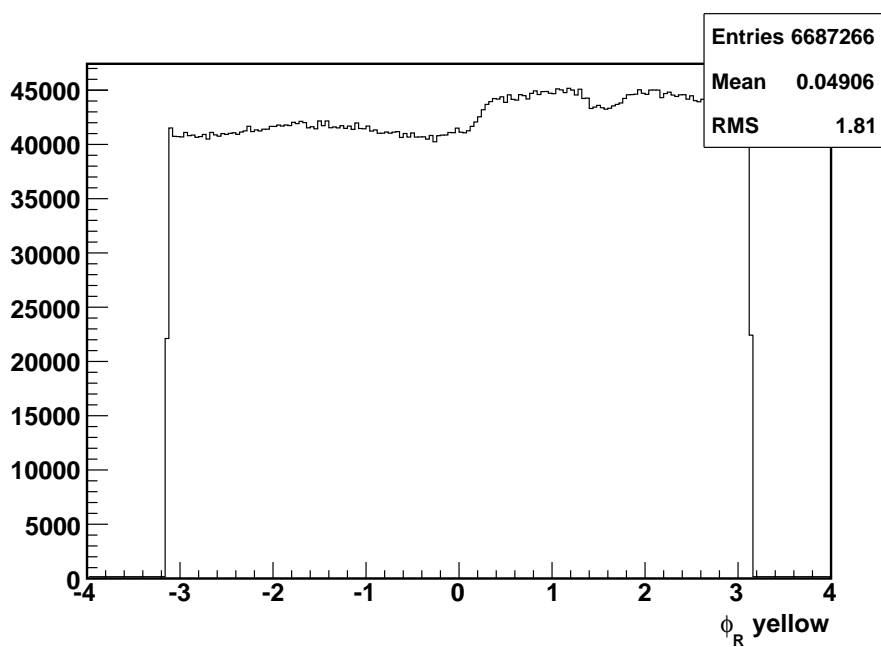


Figure 6.22:  $\phi_R$  distribution of  $\pi^+\pi^-$  pair with reference to the yellow beam polarization

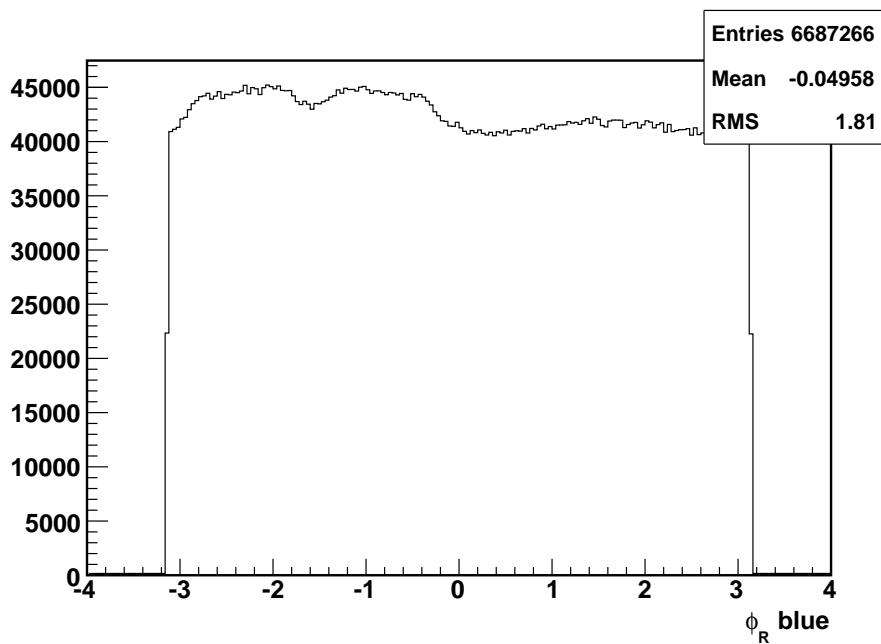


Figure 6.23:  $\phi_R$  distribution of  $\pi^+\pi^-$  pair with reference to the blue beam polarization

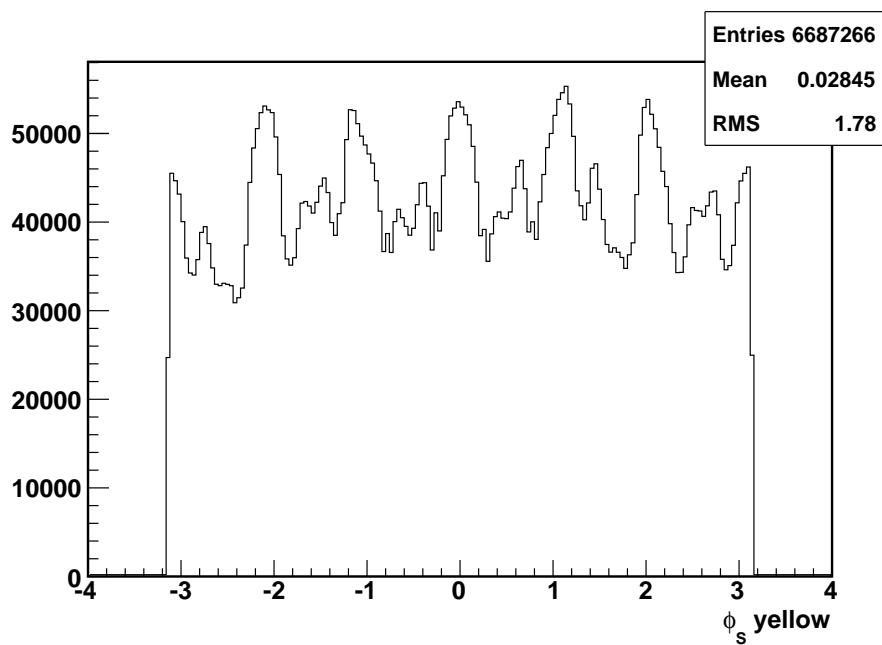


Figure 6.24:  $\phi_S$  distribution of  $\pi^+\pi^-$  pair with reference to the yellow beam polarization

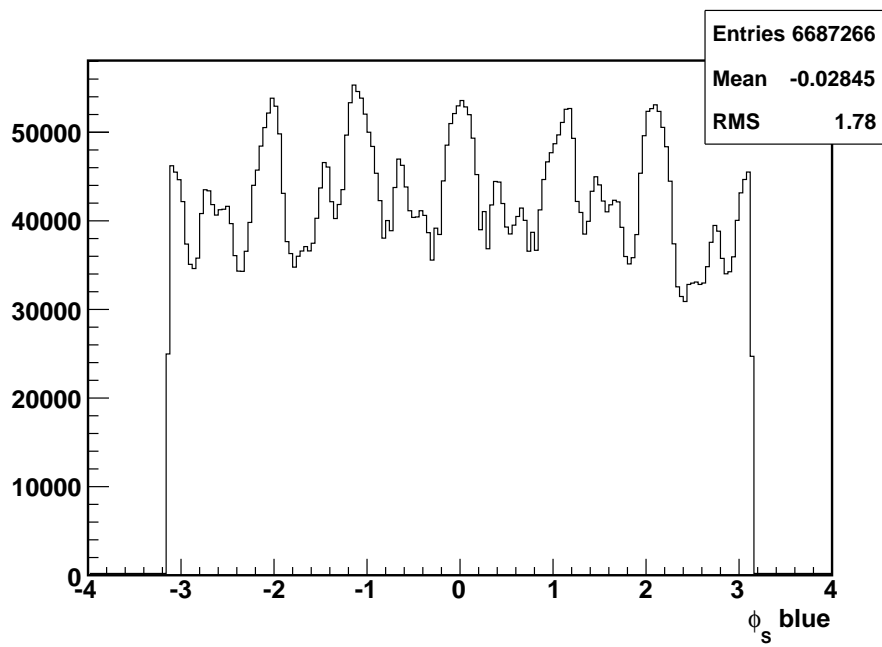


Figure 6.25:  $\phi_S$  distribution of  $\pi^+\pi^-$  pair with reference to the blue beam polarization

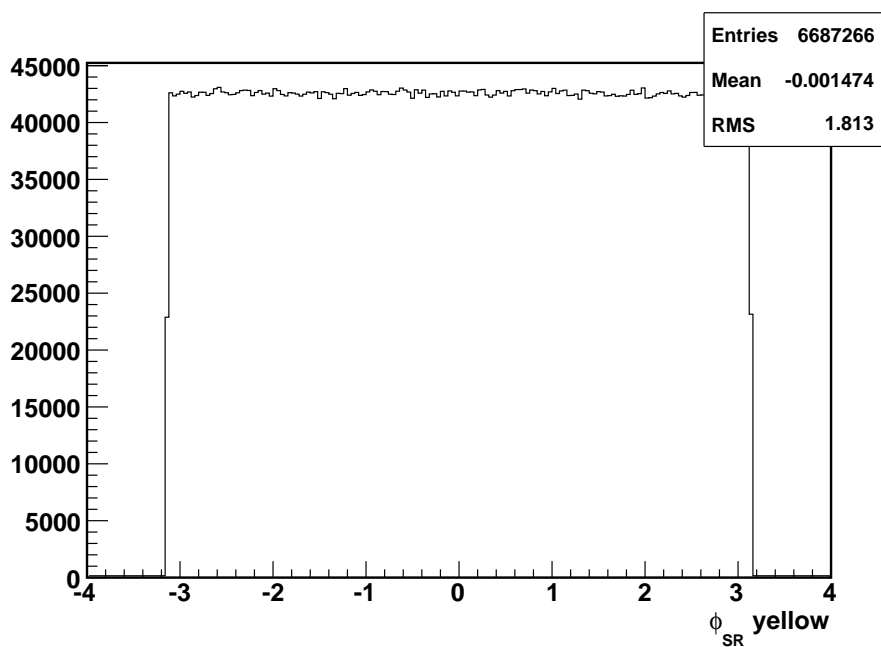


Figure 6.26:  $\phi_{RS}$  distribution of  $\pi^+\pi^-$  pair with reference to the yellow beam polarization.

This is the angle of interest in the sinusoidal modulation in asymmetry and is expected to be flat when spin state is integrated over as it is here.

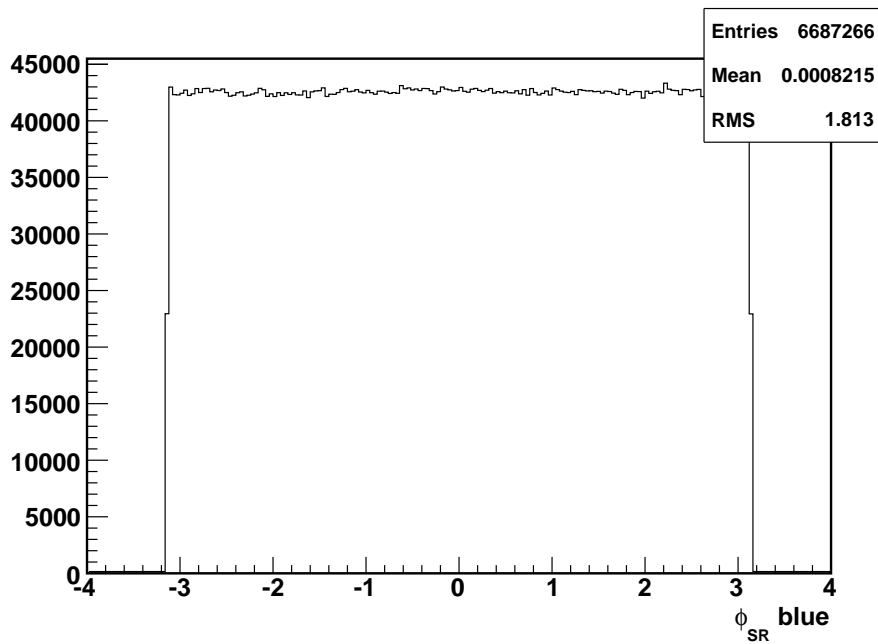


Figure 6.27:  $\phi_{RS}$  distribution of  $\pi^+\pi^-$  pair with reference to the blue beam polarization.

This is the angle of interest in the sinusoidal modulation in asymmetry and is expected to be flat when spin state is integrated over as it is here.

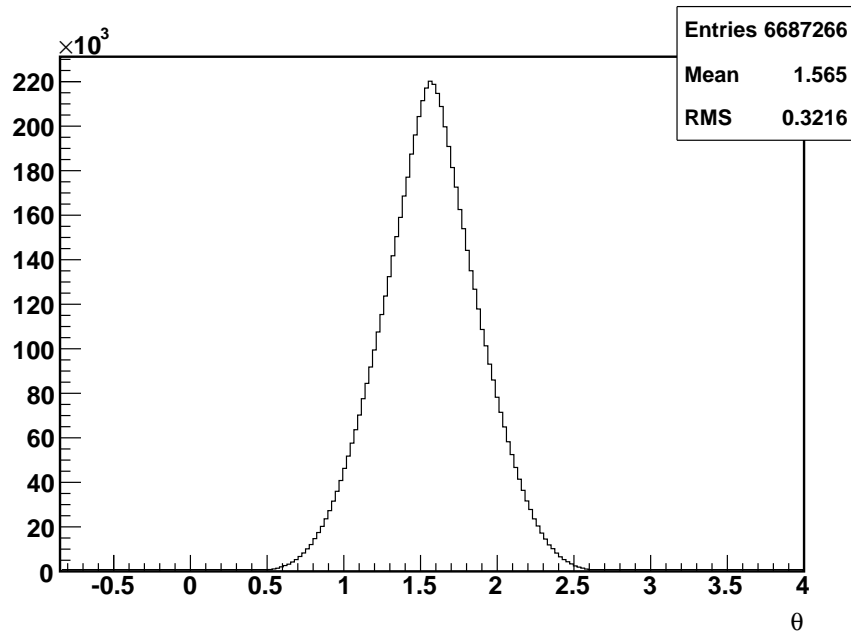


Figure 6.28:  $\theta$  distribution of  $\pi^+\pi^-$  pair

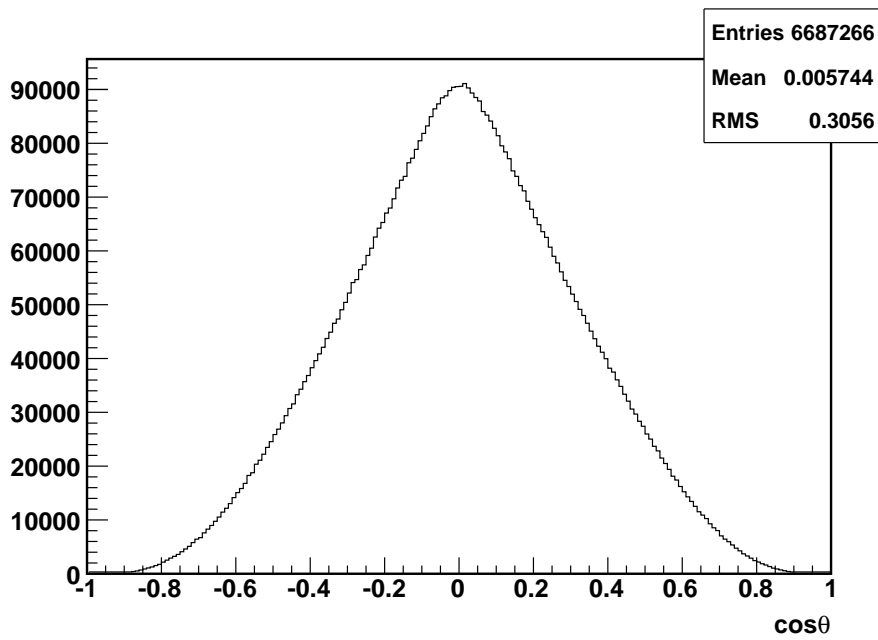


Figure 6.29:  $\cos \theta$  distribution of  $\pi^+\pi^-$  pair

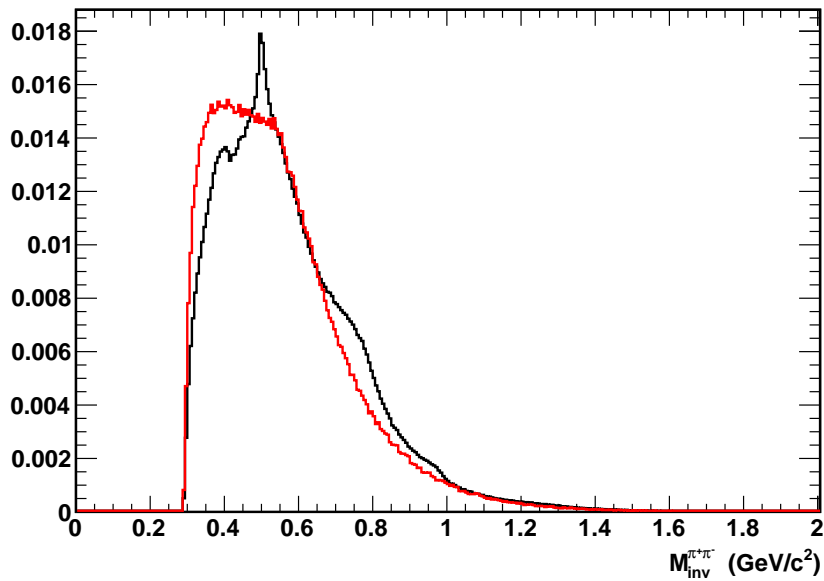


Figure 6.30: Invariant mass of  $\pi^+\pi^-$  pairs (black) and  $\pi^+\pi^+, \pi^-\pi^-$  pairs (red). The histograms are normalized to a total area of 1 unit to account for differing numbers of opposite and same sign pairs found.

## 6.5 Calculating The Asymmetry

### Luminosity Method

The asymmetry is calculated as in equation 6.1. We take the ratio of the difference of pion pairs from spin up events and spin down events, weighted by the luminosity of the beam state, to the total number of pion pairs produced.

$$A_{UT}P \sin(\phi_{RS}) = \frac{\frac{N^\uparrow}{L^\uparrow} - \frac{N^\downarrow}{L^\downarrow}}{\frac{N^\uparrow}{L^\uparrow} + \frac{N^\downarrow}{L^\downarrow}} \quad (6.1)$$

Where  $\phi_{RS}$  can take values from  $-\pi$  to  $\pi$ .

This method requires the knowledge of beam luminosity. Since this is not known exactly, the presence of the luminosity in the calculation introduces another source of error. This is not ideal especially for such a sensitive analysis. Luckily there is another way to determine the asymmetry.

### Cross Ratio Method

A more clever way of constructing the asymmetry is with the cross ratio method[35]. I break the angle  $\phi_{RS}$  up into 32 bins. I then count the number of pion pairs in that  $\phi_{RS}$  bin when the polarization is up  $N_{\phi_{RS}}^\uparrow$ .

$$N_{\phi_{RS}}^\uparrow = L^\uparrow I_{\phi_{RS}}(\theta) [1 + A_{UT}P \sin(\phi_{RS})] \quad (6.2)$$

In the above equation  $I_{\phi_{RS}}(\theta)$  is the unpolarized cross section into the designated  $\phi_{RS}$  bin and polar angle  $\theta$ ,  $L^\uparrow$  is the luminosity when the beam is in the spin up polarization, and  $P$  is the polarization percentage of the beam. The asymmetry causes an enhancement in the number of pion pairs seen. Next we look at the number of pairs we see in the same  $\phi_{RS}$  bin when the spin is down.

$$N_{\phi_{RS}}^\downarrow = L^\downarrow I_{\phi_{RS}}(\theta) [1 - A_{UT}P \sin(\phi_{RS})] \quad (6.3)$$

This time the spin is down so the plus sign in equation 6.2 becomes a negative. This tells us that there will be a decreased number of pairs we see from a spin down polarization.

Next we want to look at what happens when we change the  $\phi_{RS}$  bin by  $\pi$ . Still counting when the polarization is spin down we see that:

$$N_{\phi_{RS}+\pi}^{\downarrow} = L^{\downarrow} I_{\phi_{RS}+\pi}(\theta) [1 + A_{UT} P \sin(\phi_{RS})] \quad (6.4)$$

Since  $\sin(x + \pi) = -\sin(x)$ , the negative sign from equation 6.3 has flipped again. Finally if we look at bin  $\phi_{RS} + \pi$ , with a spin up polarization we see the sign flip one more time.

$$N_{\phi_{RS}+\pi}^{\uparrow} = L^{\uparrow} I_{\phi_{RS}+\pi}(\theta) [1 - A_{UT} P \sin(\phi_{RS})] \quad (6.5)$$

We then define “left” and “right”<sup>1</sup> as

$$\mathcal{L} = \sqrt{N_{\phi_{RS}}^{\uparrow} N_{\phi_{RS}+\pi}^{\downarrow}} = \sqrt{L^{\uparrow} L^{\downarrow} I_{\phi_{RS}} I_{\phi_{RS}+\pi}} [1 + A_{UT} P \sin(\phi_{RS})] \quad (6.6)$$

$$\mathcal{R} = \sqrt{N_{\phi_{RS}}^{\downarrow} N_{\phi_{RS}+\pi}^{\uparrow}} = \sqrt{L^{\uparrow} L^{\downarrow} I_{\phi_{RS}} I_{\phi_{RS}+\pi}} [1 - A_{UT} P \sin(\phi_{RS})] \quad (6.7)$$

The combination  $\frac{\mathcal{L}-\mathcal{R}}{\mathcal{L}+\mathcal{R}}$  gives an expression independent of luminosities.

$$\frac{\mathcal{L}-\mathcal{R}}{\mathcal{L}+\mathcal{R}} = \frac{\sqrt{N_{\phi_{RS}}^{\uparrow} N_{\phi_{RS}+\pi}^{\downarrow}} - \sqrt{N_{\phi_{RS}}^{\downarrow} N_{\phi_{RS}+\pi}^{\uparrow}}}{\sqrt{N_{\phi_{RS}}^{\uparrow} N_{\phi_{RS}+\pi}^{\downarrow}} + \sqrt{N_{\phi_{RS}}^{\downarrow} N_{\phi_{RS}+\pi}^{\uparrow}}} = A_{UT} P \sin(\phi_{RS}) \quad (6.8)$$

or in other words

$$A_{UT} \sin(\phi_{RS}) = \frac{1}{P} \frac{\sqrt{N_{\phi_{RS}}^{\uparrow} N_{\phi_{RS}+\pi}^{\downarrow}} - \sqrt{N_{\phi_{RS}}^{\downarrow} N_{\phi_{RS}+\pi}^{\uparrow}}}{\sqrt{N_{\phi_{RS}}^{\uparrow} N_{\phi_{RS}+\pi}^{\downarrow}} + \sqrt{N_{\phi_{RS}}^{\downarrow} N_{\phi_{RS}+\pi}^{\uparrow}}} \quad (6.9)$$

---

<sup>1</sup>Called left and right because the cross ratio was first used in experiments measuring asymmetries in particle production detected in two different detectors. One of these detectors was situated to the left of the incident beam and the other to the right.

Equation 6.9 is called the cross ratio and is what I will use throughout my analysis.

As stated, this form of the asymmetry is nice because luminosity and detector effects are canceled. This helps us for multiple reasons. The uncertainty in luminosity is difficult to pin down as the luminosity can fluctuate. So not having to take this into account is very beneficial. Also detector irregularities causing more pairs to be found near a “hot tower” are canceled.

One thing to note is that only 16 of my original 32  $\phi_{RS}$  bins are unique because of double counted. This is because I use the same number for  $N_{\phi_{RS}}^{\uparrow}$  for  $\phi_{RS}$  bin 1 and for  $N_{\phi_{RS}+\pi}^{\uparrow}$  for  $\phi_{RS}$  bin 9. The unique range of  $\phi_{RS}$  I choose to use is  $-\pi/2$  to  $\pi/2$

In order to extract the asymmetry, a histogram of  $\frac{1}{P} \frac{\mathcal{L} - \mathcal{R}}{\mathcal{L} + \mathcal{R}}$  is constructed. This is then fit with a sine function with the resulting amplitude of the fit is taken as  $A_{UT}$ . This is done for different kinematic bins. An example of this fitting is shown in figure 6.31.

The errors for  $N^{\uparrow}$  and  $N^{\downarrow}$  in each  $\phi_{RS}$  bin is taken as the poisson error of  $\sqrt{N^{\uparrow}}$  or  $\sqrt{N^{\downarrow}}$  for that bin. By propagating this through, we find the relevant bin error:

$$\begin{aligned} \delta \left( \frac{1}{P} \frac{\mathcal{L} - \mathcal{R}}{\mathcal{L} + \mathcal{R}} \right)_{\phi_{RS}} &= \frac{1}{P^2 \left( \sqrt{N_{\phi_{RS}}^{\uparrow} N_{\phi_{RS}+\pi}^{\downarrow}} + \sqrt{N_{\phi_{RS}}^{\downarrow} N_{\phi_{RS}+\pi}^{\uparrow}} \right)^2} \\ &\times \sqrt{P^2 \left[ N_{\phi_{RS}+\pi}^{\uparrow} N_{\phi_{RS}}^{\downarrow} \left( N_{\phi_{RS}+\pi}^{\downarrow} + N_{\phi_{RS}}^{\uparrow} \right) + N_{\phi_{RS}+\pi}^{\downarrow} N_{\phi_{RS}}^{\uparrow} \left( N_{\phi_{RS}+\pi}^{\uparrow} + N_{\phi_{RS}}^{\downarrow} \right) \right]} \end{aligned} \quad (6.10)$$

A smaller correction to the error due to the error on the polarization measurement is left out because it is significantly smaller than the term shown above.

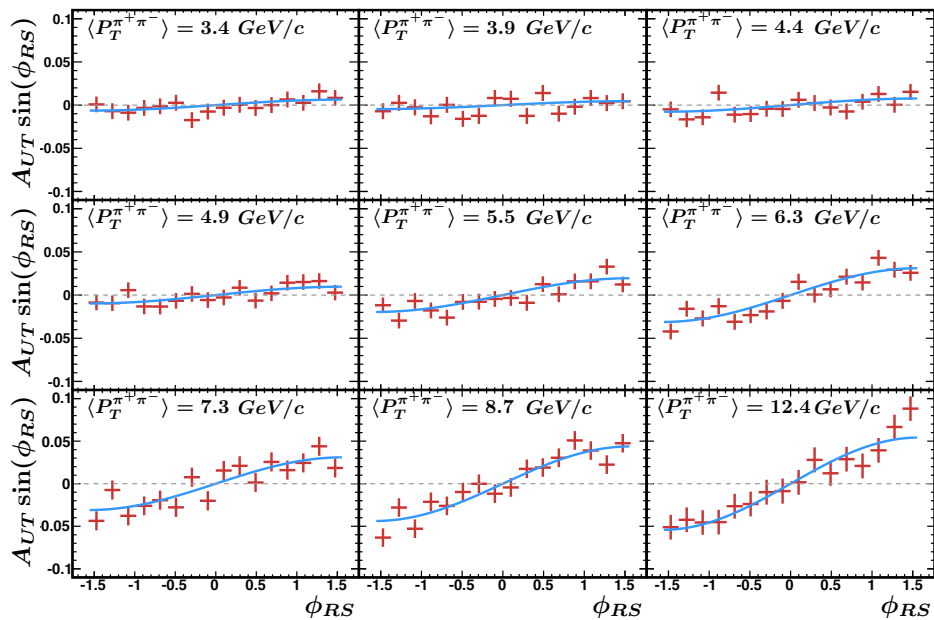


Figure 6.31: Example of the sine fitting. Here different pair transverse momentum ranges are fit with a sine. as the transverse momentum increases, the amplitude of the fit, and thus the asymmetry  $A_{UT}$ , increases.

## 6.6 Analysis Code

The analysis code is broken up into two stages. The first stage finds pion pairs in the raw data and saves them in a “pion pair tree”. The second stage analyses all the pairs and calculated the asymmetry.

The relevant files for the first stage are:

```
/star/u/klandry/ucladisk/2012IFF/xml/2012_200GeV_FinalRunList.txt  
/star/u/klandry/ucladisk/2012IFF/xml/makeTrees.xml  
/star/u/klandry/ucladisk/2012IFF/xml/submitMakeTrees.sh  
/star/u/klandry/ucladisk/2012IFF/StRoot/pionPairTreeMaker/pionPairTreemaker.h  
/star/u/klandry/ucladisk/2012IFF/StRoot/pionPairTreeMaker/pionPairTreemaker.cxx  
/star/u/klandry/ucladisk/2012IFF/makeTrees.C  
/star/u/klandry/ucladisk/2012IFF/StRoot/LoadLibs.C
```

The first step is to call submitMakeTrees.sh. This loops through the good runs we will use for the analysis in 2012\_200GeV\_FinalRunList.txt and submits makeTrees.xml to the scheduler with the run number as an input. All the relevant MuDst files for the specific run number are found by the scheduler and made into a file list. Inside makeTrees.xml, this file list is passed as an argument when makeTrees.C runs. In makeTrees.C, a chain of makers is created to carry out the work, one of which is pionPairTreeMaker. This class looks through each event. If two oppositely charged pions are found which pass  $n_\sigma(\pi)$ , vertex,  $P_T$ , and  $\eta$  cuts, it will save the two tracks in an instance of the class pionPair if the two pion are less than 1 unit in  $\eta, \phi$  space apart. The class pionPair stores all the track information for each pion as well as the trigger and other event information. It also handles all the angle calculations. A .root file is created as output from makeTrees.C for each job. After all jobs are processed, all these files are combined and the second stage is ready to begin.

The second stage consists mainly of two files:

```
/star/u/klandry/ucladisk/2012IFF/calcAsym.CR.C
```

```
/star/u/klandry/ucladisk/2012IFF/calcAsym_2dCR.C
```

They are almost identical except calcAsym\_2dCR.C keeps the asymmetry differential in two kinematic variables simultaneously while calcAsym.CR.C only keeps it differential in one at a time.

This step carries out the asymmetry calculation. During this calculation,  $A_{UT}$  must be kept differential in as many kinematic variables as possible. For this reason,  $P_T^{\pi^+\pi^-}$ ,  $M_{inv}^{\pi^+\pi^-}$ , and  $\eta^{\pi^+\pi^-}$  are broken up into different bins. The binning scheme can be seen in table 6.4. The 2D binning scheme used in calcAsym\_2dCR.C is shown in table 6.5. For each of these bins, a set of several histograms are created. Two of these histograms are responsible for storing the number of pairs from spin up and from spin down beam states. The x-axis of these histograms, which represents  $\phi_{RS}$ , is broken up into 32 bins and range from  $-\pi$  to  $\pi$ . For every pair, these histograms are incremented by one at the corresponding value of pair  $\phi_{RS}$ . In this manner they hold the number of pairs from spin up and down protons at every value of  $\phi_{RS}$ . A third histogram is created for each bin to store every pair's kinematic value to plot against the calculated asymmetry. The final piece needed in the asymmetry calculation is the polarization of the beam. A final histogram for each bin is required to hold the polarization for each pair.

Since both beams are polarized, we first treat the blue beam as the polarized beam. The histograms are filled according to this beam's polarization. The pair is then revisited with the yellow beam considered the polarized beam, and the histograms are filled again according to this beam's state. Positive  $\eta^{\pi^+\pi^-}$  corresponds to the direction of the "polarized" beam. This gives us two values for each pair. Since only one beam is considered polarized at a time, the spin state of the other beam is integrated over. Once all the pairs are processed, the asymmetry calculation begins.

Table 6.4: Binning for asymmetries differential in one kinematic variable

$P_T^{\pi^+\pi^-}$ binning		$M_{inv}^{\pi^+\pi^-}$ binning		$\eta^{\pi^+\pi^-}$ binning	
3.0	-	3.7	0.0	-	0.38
3.7	-	4.15	0.38	-	0.44
4.15	-	4.63	0.44	-	0.50
4.63	-	5.19	0.50	-	0.56
5.19	-	5.87	0.56	-	0.62
5.87	-	6.80	0.62	-	0.72
6.80	-	7.8	0.72	-	0.86
7.8	-	10.0	0.86	-	1.1
10.0	-	50.0	1.1	-	100.5

As part of the asymmetry calculation, another histogram is created for each kinematic variable bin. It is constructed to be the right hand side of equation 6.9. Like the pion number histograms, its x-axis corresponds to  $\phi_{RS}$ . The bin errors for this new histogram are calculated using equation 6.10. These new histograms are then fit with a sine function. The amplitude is taken as the value of  $A_{UT}$  for that kinematic bin. The output of calcAsym.CR.C is a root file containing all the histograms. These can then quickly be refit and plotted using /star/u/klandry/ucladisk/2012IFF/makePlots.C.

### Advanced Treatment of Beam Polarization

Ideally the polarization of the beam will be constant throughout the entire data set, however this is not possible. Because of this, I attempted a more advanced treatment

Table 6.5: Binning for asymmetries differential in two kinematic variables

$P_T^{\pi^+\pi^-}$ binning			$M_{inv}^{\pi^+\pi^-}$ binning			$\eta^{\pi^+\pi^-}$ binning		
3.0	-	4.0	0.0	-	0.4	-2	-	-0.5
4.0	-	5.0	0.4	-	0.6	-0.5	-	0.0
5.0	-	6.5	0.6	-	0.8	0.0	-	0.5
6.5	-	8.0	0.8	-	1.0	0.5	-	2
8.0	-	50.0	1.0	-	100.5			

of the polarization. The following section will be a detailed explanation of how exactly it is calculated. As an example I will focus on just one of the kinematic bins with the assumption that this will be done in each kinematic bin separately.

To handle the polarization, histograms are created for each of the 32  $\phi_{RS}$  bins. These histograms store the beam polarization of pairs from spin up and down events, as well as the error of the beam polarization squared from spin up and spin down events. The latter will be used when calculating errors. Because the polarization can differ between spin up and down pairs as well as between  $\phi_{RS}$  bins, I alter how the polarization is used in the calculation compared to equation 6.9. Instead of having one value for the polarization, I use several values for the polarization, one for each spin state and  $\phi_{RS}$  bin.

$$A_{UT} \sin(\phi_{RS}) = \frac{\sqrt{\frac{N_{\phi_{RS}}^{\uparrow}}{\langle p_{\phi_{RS}}^{\uparrow} \rangle} \frac{N_{\phi_{RS}+\pi}^{\downarrow}}{\langle p_{\phi_{RS}+\pi}^{\downarrow} \rangle}} - \sqrt{\frac{N_{\phi_{RS}+\pi}^{\uparrow}}{\langle p_{\phi_{RS}+\pi}^{\uparrow} \rangle} \frac{N_{\phi_{RS}}^{\downarrow}}{\langle p_{\phi_{RS}}^{\downarrow} \rangle}}}{\sqrt{N_{\phi_{RS}}^{\uparrow} N_{\phi_{RS}+\pi}^{\downarrow}} + \sqrt{N_{\phi_{RS}+\pi}^{\uparrow} N_{\phi_{RS}}^{\downarrow}}} \quad (6.11)$$

Where  $\langle p_{\phi_{RS}}^{\uparrow} \rangle$ ,  $\langle p_{\phi_{RS}+\pi}^{\downarrow} \rangle$ ,  $\langle p_{\phi_{RS}+\pi}^{\uparrow} \rangle$ , and  $\langle p_{\phi_{RS}}^{\downarrow} \rangle$  are the average beam polarizations in pairs from spin up, down events and at angle  $\phi_{RS}$ ,  $\phi_{RS}+\pi$ . Therefore the number of pairs from each spin state and angle are weighted by their own separate average polarization.

The histogram responsible for storing the values to be fit is now used. The x-axis of this histogram is also separated into 32  $\phi_{RS}$  bins and ranges from  $-\pi$  to  $\pi$ . For each  $\phi_{RS}$  bin the left hand side of equation 6.11 is calculated and used to set the value of the corresponding  $\phi_{RS}$  bin in the to fit histogram.

The bin errors seen in figure 6.31 are also set by hand but are a little more intricate.

$$\text{Let } \mathcal{E} = \frac{\sqrt{\frac{N_{\phi_{RS}}^{\uparrow}}{\langle p_{\phi_{RS}}^{\uparrow} \rangle} \frac{N_{\phi_{RS}+\pi}^{\downarrow}}{\langle p_{\phi_{RS}+\pi}^{\downarrow} \rangle}} - \sqrt{\frac{N_{\phi_{RS}+\pi}^{\uparrow}}{\langle p_{\phi_{RS}+\pi}^{\uparrow} \rangle} \frac{N_{\phi_{RS}}^{\downarrow}}{\langle p_{\phi_{RS}}^{\downarrow} \rangle}}}{\sqrt{N_{\phi_{RS}}^{\uparrow} N_{\phi_{RS}+\pi}^{\downarrow}} + \sqrt{N_{\phi_{RS}+\pi}^{\uparrow} N_{\phi_{RS}}^{\downarrow}}} \quad (6.12)$$

The error on  $\mathcal{E}$  is defined as  $\delta\mathcal{E} = \sqrt{E_{stat}^2 + E_{pol}^2}$ . Where  $E_{stat}^2$  is the statistical error and  $E_{pol}^2$  is the error from the polarization uncertainty. Let's look at these two individually starting with the statistical error term.

To make our lives easier let's introduce two new variables,  $a = \sqrt{N_{\phi_{RS}}^{\uparrow} N_{\phi_{RS}+\pi}^{\downarrow}}$  and  $b = \sqrt{N_{\phi_{RS}+\pi}^{\uparrow} N_{\phi_{RS}}^{\downarrow}}$

Rewriting equation 6.12 with these new variables, gives

$$\mathcal{E} = \frac{\frac{a}{\sqrt{\langle p_{\phi_{RS}}^{\uparrow} \rangle \langle p_{\phi_{RS}+\pi}^{\downarrow} \rangle}} - \frac{b}{\sqrt{\langle p_{\phi_{RS}+\pi}^{\uparrow} \rangle \langle p_{\phi_{RS}}^{\downarrow} \rangle}}}{a + b} \quad (6.13)$$

With this notation, the statistical error becomes

$$E_{stat}^2 = \left( \frac{\partial \mathcal{E}}{\partial a} \right)^2 \delta a^2 + \left( \frac{\partial \mathcal{E}}{\partial b} \right)^2 \delta b^2 \quad (6.14)$$

The errors on  $a$  and  $b$  are similarly calculated.

$$\delta a^2 = \left( \frac{\partial a}{\partial N_{\phi_{RS}}^{\uparrow}} \right)^2 \left( \delta N_{\phi_{RS}}^{\uparrow} \right)^2 + \left( \frac{\partial a}{\partial N_{\phi_{RS}+\pi}^{\downarrow}} \right)^2 \left( \delta N_{\phi_{RS}+\pi}^{\downarrow} \right)^2 \quad (6.15)$$

$$\delta b^2 = \left( \frac{\partial b}{\partial N_{\phi_{RS}+\pi}^{\uparrow}} \right)^2 \left( \delta N_{\phi_{RS}+\pi}^{\uparrow} \right)^2 + \left( \frac{\partial b}{\partial N_{\phi_{RS}}^{\downarrow}} \right)^2 \left( \delta N_{\phi_{RS}}^{\downarrow} \right)^2 \quad (6.16)$$

Taking the errors on the number of pairs in a bin as  $\delta N = \sqrt{N}$ ,

$$\delta a^2 = \frac{1}{4} \left( N_{\phi_{RS}}^{\uparrow} + N_{\phi_{RS}+\pi}^{\downarrow} \right) \quad (6.17)$$

$$\delta b^2 = \frac{1}{4} \left( N_{\phi_{RS}+\pi}^{\uparrow} + N_{\phi_{RS}}^{\downarrow} \right) \quad (6.18)$$

Putting everything together  $E_{stat}$  becomes

$$E_{stat}^2 = \frac{1}{4} \frac{1}{(a+b)^4} \left[ \frac{1}{\sqrt{\langle p_{\phi_{RS}}^{\uparrow} \rangle \langle p_{\phi_{RS}+\pi}^{\downarrow} \rangle}} + \frac{1}{\sqrt{\langle p_{\phi_{RS}+\pi}^{\uparrow} \rangle \langle p_{\phi_{RS}}^{\downarrow} \rangle}} \right]^2 \times \left[ b^2 \left( N_{\phi_{RS}}^{\uparrow} + N_{\phi_{RS}+\pi}^{\downarrow} \right) + a^2 \left( N_{\phi_{RS}+\pi}^{\uparrow} + N_{\phi_{RS}}^{\downarrow} \right) \right] \quad (6.19)$$

Assuming all  $N$ s and polarizations are equal we see that the statistical error scales like

$$E_{stat}^2 \sim \frac{1}{p^2 N}; \text{ the same as the simple treatment of the polarization.}$$

The error from the polarization uncertainty is a little bit trickier to tackle. Since each pair comes with its own polarization uncertainty, I want to use all of them. To do this I have to change how I write  $\mathcal{E}$ . Namely I want to explicitly write out how each pair's polarization comes in instead of the average polarization.

$$\mathcal{E} = \sqrt{\frac{\frac{N_{\phi_{RS}}^{\uparrow}^2 N_{\phi_{RS}+\pi}^{\downarrow}^2}{\sum_{i=1}^{N_{\phi_{RS}}^{\uparrow}} p_i \sum_{j=1}^{N_{\phi_{RS}+\pi}^{\downarrow}} p_j} - \frac{N_{\phi_{RS}}^{\downarrow}^2 N_{\phi_{RS}+\pi}^{\uparrow}^2}{\sum_{n=1}^{N_{\phi_{RS}}^{\downarrow}} p_n \sum_{m=1}^{N_{\phi_{RS}+\pi}^{\uparrow}} p_m}}{a+b}} \quad (6.20)$$

To obtain this form of  $\mathcal{E}$  I have used,  $\langle p_x \rangle = \frac{1}{N_x} \sum_{x=1}^{N_x} p_x$ .

By writing  $\mathcal{E}$  as in equation 6.20, it is clearer how the polarization uncertainty propagates to the error of  $\mathcal{E}$ .

$$E_{pol}^2 = \sum_{i=1}^{N_{\phi_{RS}}^{\uparrow}} \left( \frac{\partial \mathcal{E}}{\partial p_i} \right)^2 \delta p_i^2 + \sum_{j=1}^{N_{\phi_{RS}+\pi}^{\downarrow}} \left( \frac{\partial \mathcal{E}}{\partial p_j} \right)^2 \delta p_j^2 + \sum_{n=1}^{N_{\phi_{RS}}^{\downarrow}} \left( \frac{\partial \mathcal{E}}{\partial p_n} \right)^2 \delta p_n^2 + \sum_{m=1}^{N_{\phi_{RS}+\pi}^{\uparrow}} \left( \frac{\partial \mathcal{E}}{\partial p_m} \right)^2 \delta p_m^2 \quad (6.21)$$

Computing the derivative  $\frac{\partial \mathcal{E}}{\partial p_i}$  gives,

$$\frac{\partial \mathcal{E}}{\partial p_i} = \frac{-1}{2(a+b)} \frac{a^2 \sum_{j=1}^{N_{\phi_{RS}+\pi}^{\downarrow}} p_j}{\left( \sum_{j=1}^{N_{\phi_{RS}}^{\downarrow}} p_i \sum_{j=1}^{N_{\phi_{RS}+\pi}^{\downarrow}} p_j \right)^{3/2}} \quad (6.22)$$

Using again the fact that  $\langle p_x \rangle = \frac{1}{N_x} \sum_{x=1}^{N_x} p_x$ , it follows that

$$\sum_{i=1}^{N_{\phi_{RS}}^{\uparrow}} \left( \frac{\partial \mathcal{E}}{\partial p_i} \right)^2 \delta p_i^2 = \sum_{i=1}^{N_{\phi_{RS}}^{\uparrow}} \frac{a^4}{4(a+b)^2} \frac{\delta p_i^2}{N_{\phi_{RS}}^{\uparrow} \langle p_{\phi_{RS}}^{\uparrow} \rangle^3 N_{\phi_{RS}+\pi}^{\downarrow} \langle p_{\phi_{RS}+\pi}^{\downarrow} \rangle} \quad (6.23)$$

$$= \frac{1}{4} \frac{N_{\phi_{RS}+\pi}^{\downarrow}}{(a+b)^2} \frac{\langle \delta p_{\phi_{RS}}^{\uparrow} \rangle^2}{\langle p_{\phi_{RS}}^{\uparrow} \rangle^3 \langle p_{\phi_{RS}+\pi}^{\downarrow} \rangle} \quad (6.24)$$

Each term has a similar form. Putting them all together gives the error from the polarization uncertainty.

$$E_{pol}^2 = \frac{1}{4(a+b)^2} \left[ N_{\phi_{RS}+\pi}^{\downarrow} \frac{\langle \delta p_{\phi_{RS}}^{\uparrow} \rangle^2}{\langle p_{\phi_{RS}}^{\uparrow} \rangle^3 \langle p_{\phi_{RS}+\pi}^{\downarrow} \rangle} + N_{\phi_{RS}}^{\uparrow} \frac{\langle \delta p_{\phi_{RS}+\pi}^{\downarrow} \rangle^2}{\langle p_{\phi_{RS}+\pi}^{\downarrow} \rangle^3 \langle p_{\phi_{RS}}^{\uparrow} \rangle} \right. \\ \left. + N_{\phi_{RS}+\pi}^{\uparrow} \frac{\langle \delta p_{\phi_{RS}}^{\downarrow} \rangle^2}{\langle p_{\phi_{RS}}^{\downarrow} \rangle^3 \langle p_{\phi_{RS}+\pi}^{\uparrow} \rangle} + N_{\phi_{RS}}^{\downarrow} \frac{\langle \delta p_{\phi_{RS}+\pi}^{\uparrow} \rangle^2}{\langle p_{\phi_{RS}+\pi}^{\uparrow} \rangle^3 \langle p_{\phi_{RS}}^{\downarrow} \rangle} \right] \quad (6.25)$$

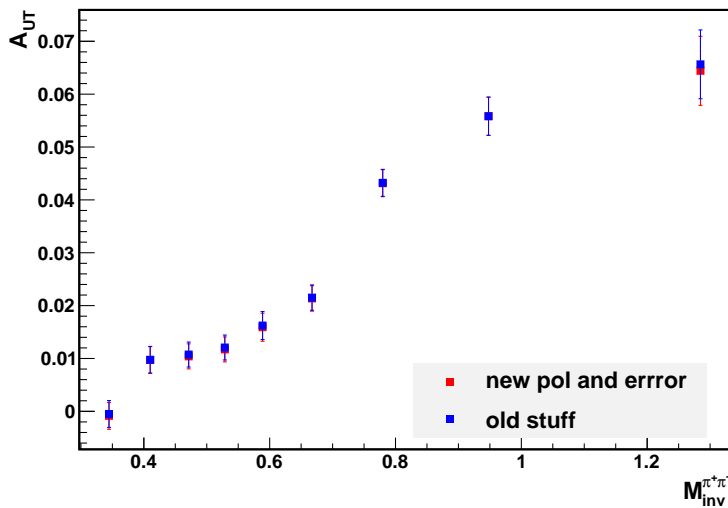


Figure 6.32: The blue points are obtained by treating the asymmetry and error as in equations 6.9 and 6.10. The red points are obtained using the advanced treatment of beam polarization in equations 6.11 and 6.26.

To compare this error to the statistical error, lets check to see how it scales with the number of pairs in the same way we did before. It turns out  $E_{pol}^2 \sim \frac{1}{p^2 N} \frac{\delta p^2}{p^2}$ . In other words the error due to the polarization uncertainty is smaller than the statistical error by a factor of  $\frac{\delta p^2}{p^2}$ . A typical value for this is .01. The total bin error is then

$$E = \sqrt{E_{stat}^2 + E_{pol}^2}. \quad (6.26)$$

At the end of the day this advanced treatment of the polarization made little to know significant difference. It seems as though the polarization was uniform enough for this to not have an impact. This can be seen in figure 6.32.

# 7 Results

## 7.1 One Dimensional Kinematic Binning

The first step was to recreate the results of the 2006 study shown in chapter 5. The larger data set from the 2012 run allowed for more bins in each kinematic variable. The results can be seen in figures 7.1, 7.2, and 7.3. The dependence the asymmetry has on  $\eta$  and  $\eta^{\pi^+\pi^-}$  are very agreeable between 2006 and 2012 analyses. The mass dependence shows the same trend but there are some differences between the two years. In 2006 a larger increase in asymmetry was seen around the  $\rho$  mass than in 2012. Another difference is between the high mass point. In 2006 the highest mass has a decreased asymmetry when compared to the asymmetry near the  $\rho$  but in 2012 the highest mass point shows a larger asymmetry. One possible reason could be that the high mass point in 2012 comes with a higher  $P_T^{\pi^+\pi^-}$  or  $\eta^{\pi^+\pi^-}$  than it did in 2006 due to slightly different cuts. Since the asymmetry is highly dependent on these two, with a larger values correlated to higher asymmetries, this could cause the asymmetry to be increased. As we will see in section 7.4, this trend of a lower asymmetry in the high mass point is indeed a real phenomenon. When we plot the asymmetry in two dimensions, we see the high mass point at a lower asymmetry than the asymmetry near the  $\rho$  region when holding  $P_T^{\pi^+\pi^-}$  constant (figure 7.17), as well as when we hold  $\eta^{\pi^+\pi^-}$  constant (figure 7.13).

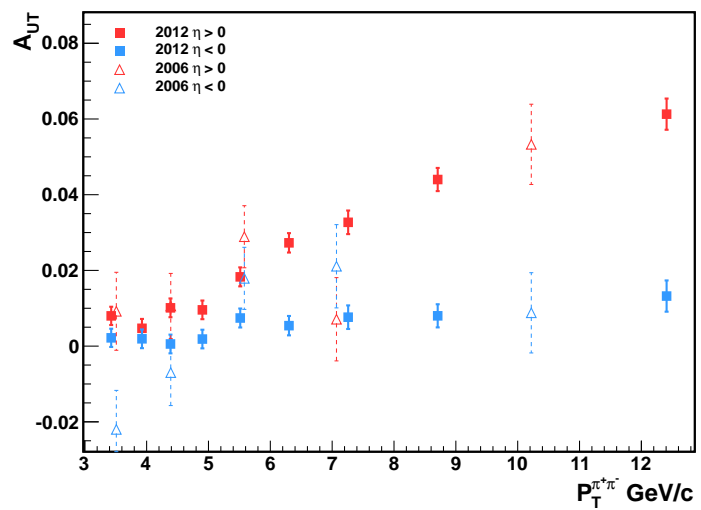


Figure 7.1: Comparison of  $P_T^{\pi^+\pi^-}$  Asymmetries from 2012 and 2006

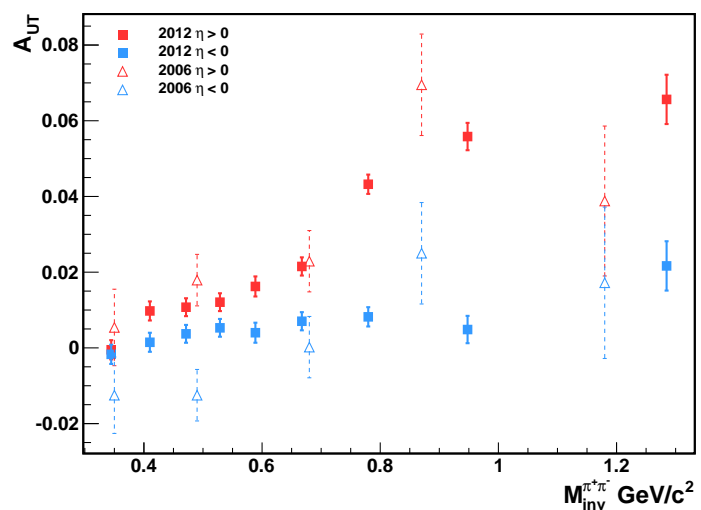


Figure 7.2: Comparison of  $M_{inv}^{\pi^+\pi^-}$  Asymmetries from 2012 and 2006

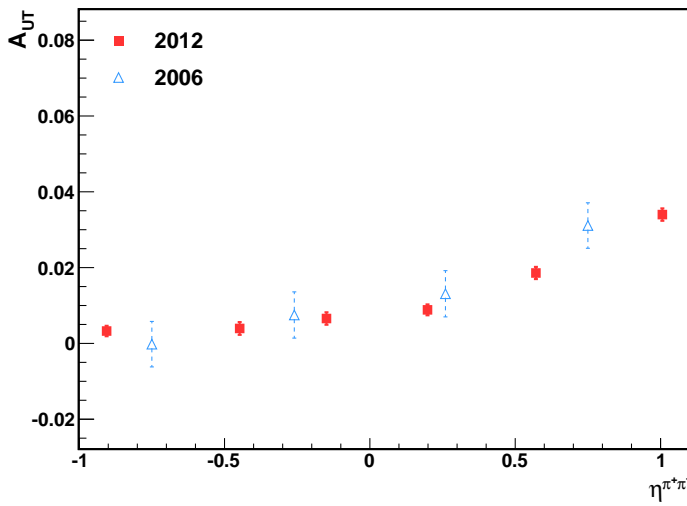


Figure 7.3: Comparison of  $\eta^{\pi^+\pi^-}$  Asymmetries from 2012 and 2006

Show plots for AvM AvPt AvEta probably the full trigger set. Show different radius cuts and the average pt and M plots for the different radius cuts. Show how this gives access to a different z.

Changing the radius changes the invariance mass, transverse momentum relationship.

$$M_{inv}^{\pi^+\pi^-} = 2P_T^{\pi^+} P_T^{\pi^-} \left[ \cosh(\eta^{\pi^+} - \eta^{\pi^-}) - \cos(\phi^{\pi^+} - \phi^{\pi^-}) \right] \quad (7.1)$$

As the difference in  $\eta$  and  $\phi$  of the  $\pi^+$  and  $\pi^-$  decreases, what is in the square brackets in equation 7.2 also decreases. To keep the same invariant mass, the transverse momentums must increase. So by looking at the Asymmetry in the same invariant mass bins across several different cone radii, we expect the smaller radii to have a larger average transverse momentum. As we have seen a larger transverse momentum corresponds to an increased asymmetry. Therefore a smaller radius should have a larger asymmetry for each invariant mass. This can be seen in figure 7.5. This gives us a hint at how the IFF and transversity depend on z.

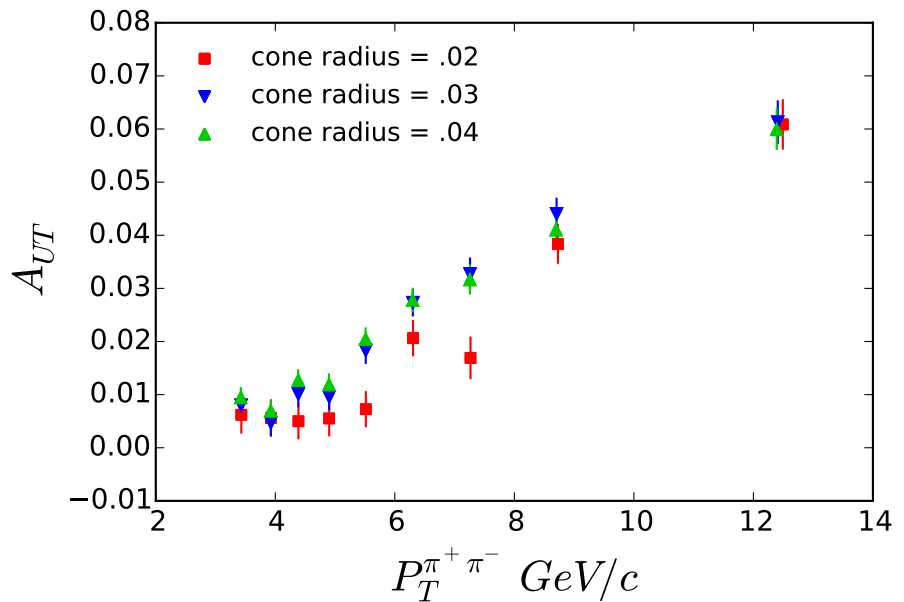


Figure 7.4: should replace with 3-26-15 version

Recall that  $z$  is the fraction of fragmenting quark momentum the pion pair retains.

$$z = \frac{\vec{P}_{\pi^+} + \vec{P}_{\pi^-}}{\vec{P}_q} \quad (7.2)$$

I'm not really sure this makes sense I need to think about it more.

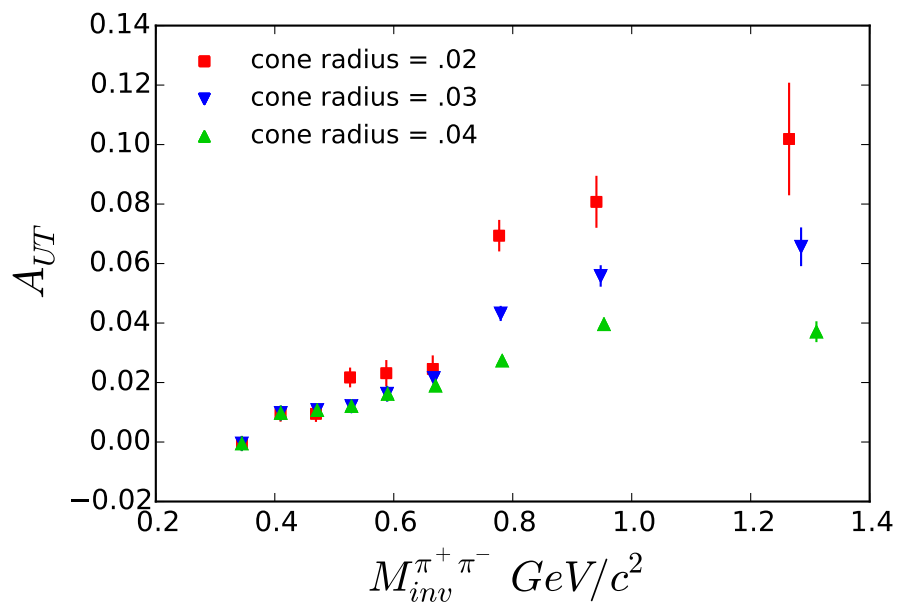


Figure 7.5: should replace with 3-26-15 version  $\eta > 0$

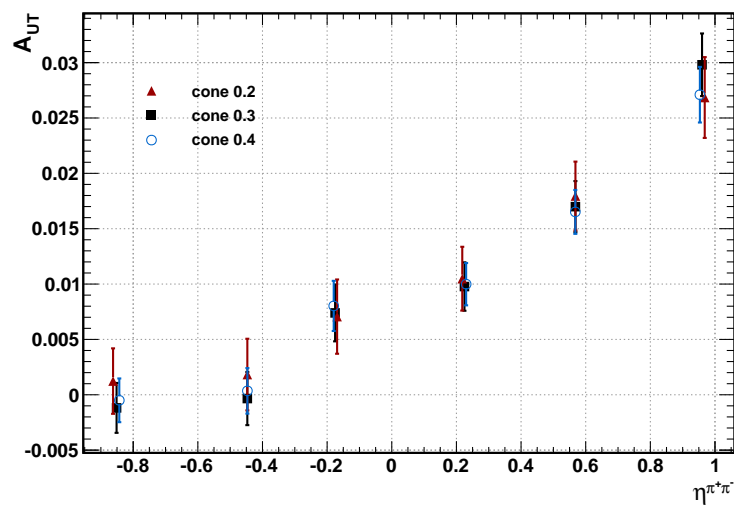


Figure 7.6: should replace with 3-26-15 version

## 7.2 Checking for Asymmetry in Same Sign Pairs

A good check to perform to test if the asymmetry we see is due to the physics we are investigating or some other actuation is to perform the same analysis on pion pairs of the same charge. We would expect the asymmetry to be zero for same sign pairs since the IFF only. So I have done the exact same procedure except matching up same sign pions in each event instead of opposite sign pions. I did this over the entire pseudorapidity range. A comparison of the asymmetry of opposite sign and same sign pion pairs can be seen in figures 7.7, 7.8, and 7.9. As expected the asymmetry for same sign pairs is consistent with zero. This is a good sign that our analysis for the opposite sign pairs is correct.

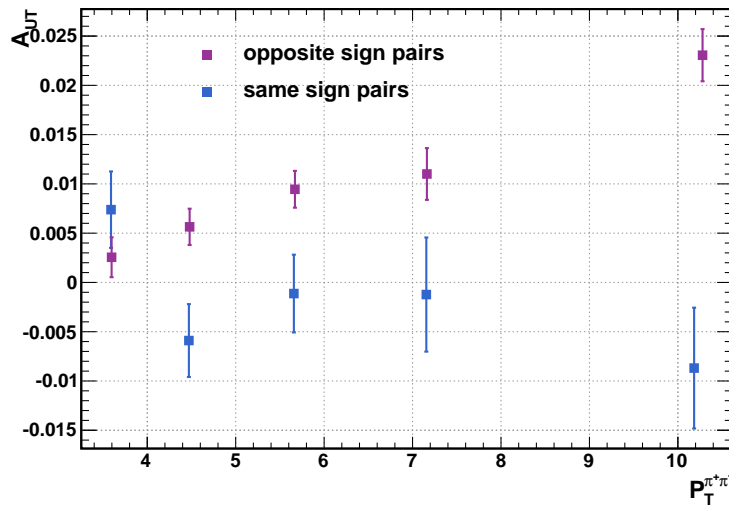


Figure 7.7: Comparison of the asymmetry's dependence on transverse momentum between same sign pairs and opposite sign pairs.

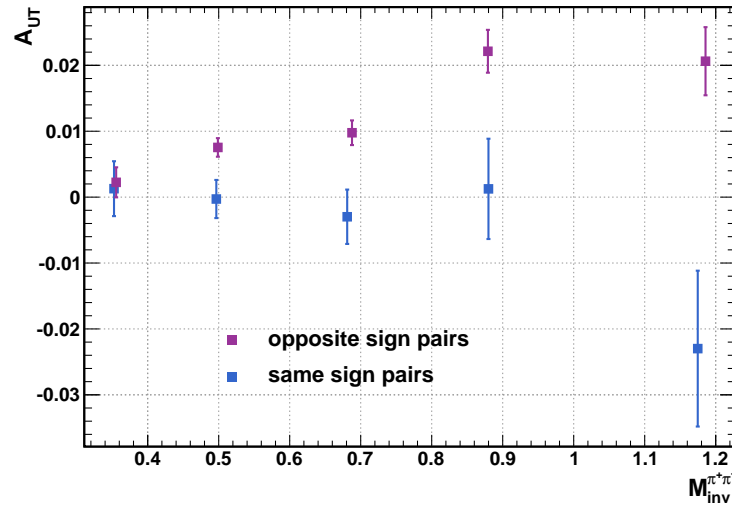


Figure 7.8: Comparison of the asymmetry's dependence on invariant mass between same sign pairs and opposite sign pairs.

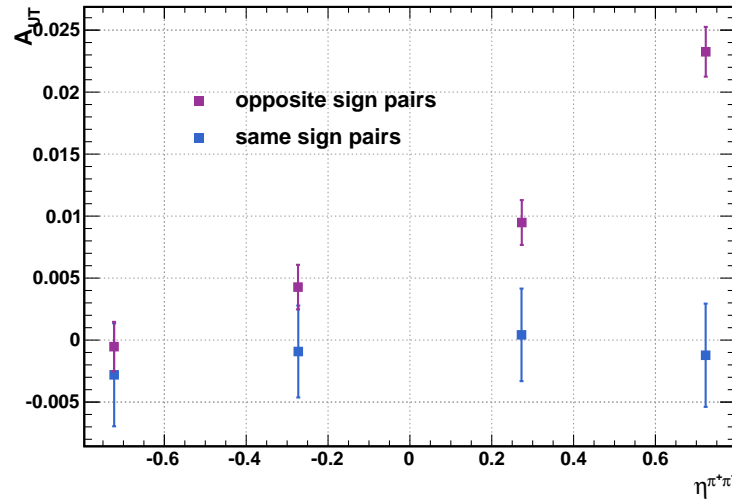


Figure 7.9: Comparison of the asymmetry's dependence on pseudorapidity between same sign pairs and opposite sign pairs.

### 7.3 Check For Other False Asymmetries

In order to make sure the asymmetries we detect are not caused by some detector factor or an error in the code, we perform checks on situations we think will show zero asymmetry. The first check is done by analyzing the same data but randomly assigning a spin state to the polarized proton. A randomly assigned spin is assigned correctly half the time and incorrectly the other half. Looking at the cross ratio formula from earlier (eq 6.8) for both cases we see the asymmetry should vanish. The correct spin assignment is represented to the left of the plus sign in equation 7.3, and the incorrect assignment to the right. The incorrect assignment is taken into account by the change in the spin orientation superscripts right of the plus sign in equation 7.3. The two factors cancel exactly with enough statistics and should lead to zero observed asymmetry.

$$\frac{1}{2} \frac{\sqrt{N_{\phi_{RS}}^{\uparrow} N_{\phi_{RS}+\pi}^{\downarrow}} - \sqrt{N_{\phi_{RS}}^{\downarrow} N_{\phi_{RS}+\pi}^{\uparrow}}}{\sqrt{N_{\phi_{RS}}^{\uparrow} N_{\phi_{RS}+\pi}^{\downarrow}} + \sqrt{N_{\phi_{RS}}^{\downarrow} N_{\phi_{RS}+\pi}^{\uparrow}}} + \frac{1}{2} \frac{\sqrt{N_{\phi_{RS}}^{\downarrow} N_{\phi_{RS}+\pi}^{\uparrow}} - \sqrt{N_{\phi_{RS}}^{\uparrow} N_{\phi_{RS}+\pi}^{\downarrow}}}{\sqrt{N_{\phi_{RS}}^{\downarrow} N_{\phi_{RS}+\pi}^{\uparrow}} + \sqrt{N_{\phi_{RS}}^{\uparrow} N_{\phi_{RS}+\pi}^{\downarrow}}} = 0 \quad (7.3)$$

You can see in figure 7.10 we see no false asymmetry for random proton spin assignment.

Just as we randomly assigned the spin state of the proton, we also randomly assign the charges on the  $\pi^+, \pi^-$ . This changes the direction of  $\mathbf{R}$ .

$$\sin(\phi_R) = \frac{(\mathbf{P}_B \times \mathbf{R}) \hat{\mathbf{P}}_h}{|\hat{\mathbf{P}}_h \times \mathbf{P}_B| |\hat{\mathbf{P}}_h \times \mathbf{R}|} \quad (7.4)$$

$$\cos(\phi_R) = \frac{\hat{\mathbf{P}}_h \times \mathbf{P}_B}{|\hat{\mathbf{P}}_h \times \mathbf{P}_B|} \frac{\hat{\mathbf{P}}_h \times \mathbf{R}}{|\hat{\mathbf{P}}_h \times \mathbf{R}|} \quad (7.5)$$

By making the substitution  $R \rightarrow -R$  in equations 7.4 and 7.5, it is seen that  $\phi_R \rightarrow \phi_R + \pi$  (or  $\phi_R \rightarrow \phi_R - \pi$  because  $\phi_R$  is restricted to the range  $-\pi$  to  $\pi$ ). Since  $R$  doesn't appear in the definition of  $\sin(\phi_S)$  or  $\cos(\phi_S)$ ,  $\phi_S$  is unchanged. This leads to  $\phi_{RS} \rightarrow \phi_{RS} + \pi$  (or  $\phi_{RS} \rightarrow \phi_{RS} - \pi$  again because of the restriction on the values of  $\phi_{RS}$ ). Just like

the random spin assignment, the random pion charge assignment will be correct half the time and incorrect the other half. By substituting  $\phi_{RS} \rightarrow \phi_{RS} \pm \pi$  into the cross ratio equation 6.8 half the time, we come to an equation similar to equation 7.3 with both factors canceling.

$$\frac{1}{2} \frac{\sqrt{N_{\phi_{RS}}^{\uparrow} N_{\phi_{RS}+\pi}^{\downarrow}} - \sqrt{N_{\phi_{RS}}^{\downarrow} N_{\phi_{RS}+\pi}^{\uparrow}}}{\sqrt{N_{\phi_{RS}}^{\uparrow} N_{\phi_{RS}+\pi}^{\downarrow}} + \sqrt{N_{\phi_{RS}}^{\downarrow} N_{\phi_{RS}+\pi}^{\uparrow}}} + \frac{1}{2} \frac{\sqrt{N_{\phi_{RS}+\pi}^{\uparrow} N_{\phi_{RS}}^{\downarrow}} - \sqrt{N_{\phi_{RS}+\pi}^{\downarrow} N_{\phi_{RS}}^{\uparrow}}}{\sqrt{N_{\phi_{RS}+\pi}^{\uparrow} N_{\phi_{RS}}^{\downarrow}} + \sqrt{N_{\phi_{RS}+\pi}^{\downarrow} N_{\phi_{RS}}^{\uparrow}}} = 0 \quad (7.6)$$

Again, as figure 7.11 shows, we detect no asymmetry from randomly assigned pion charges.

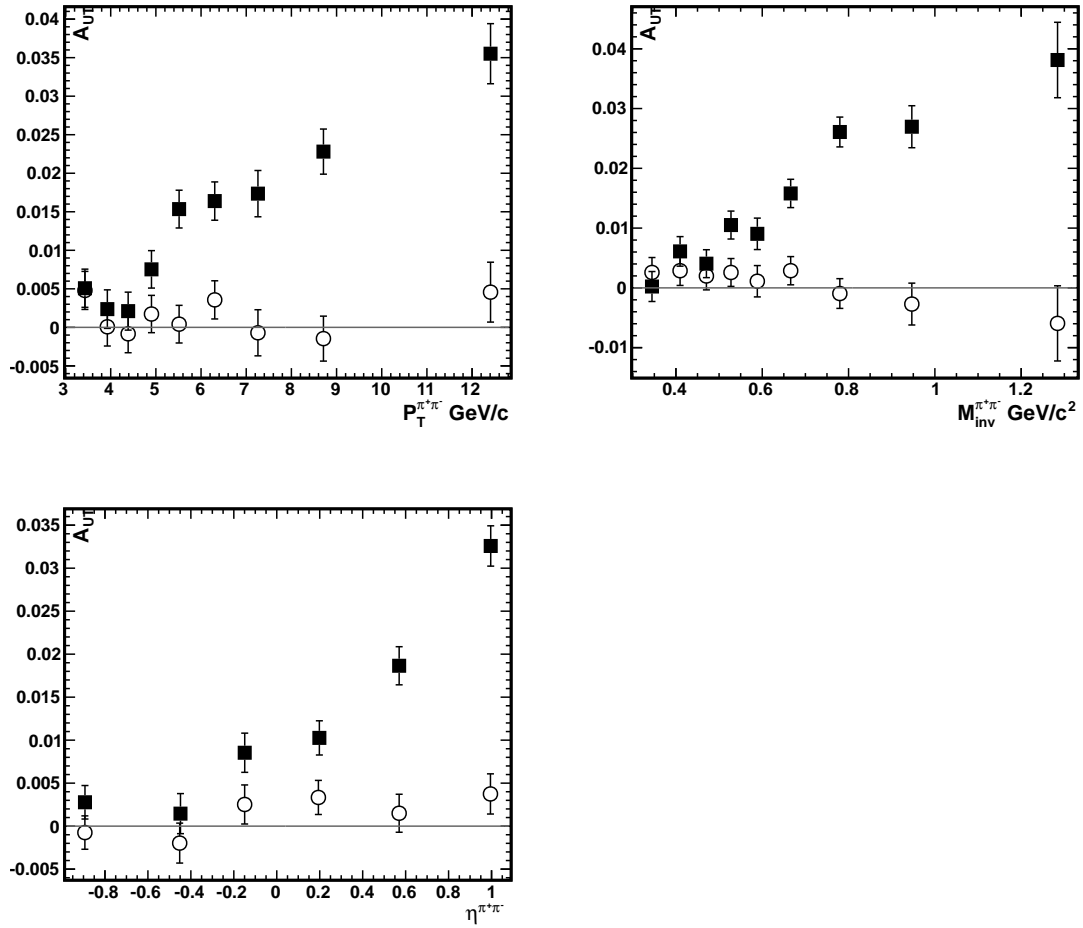


Figure 7.10: Randomly assigned spin state (open circles) show no sign of asymmetry in any kinematic variable. Correct assignment (solid squares) shown for comparison.  
 $-2 < \eta^{\pi^+\pi^-} < 2$  for  $P_T^{\pi^+\pi^-}$  and  $M_{\text{inv}}^{\pi^+\pi^-}$  plots.

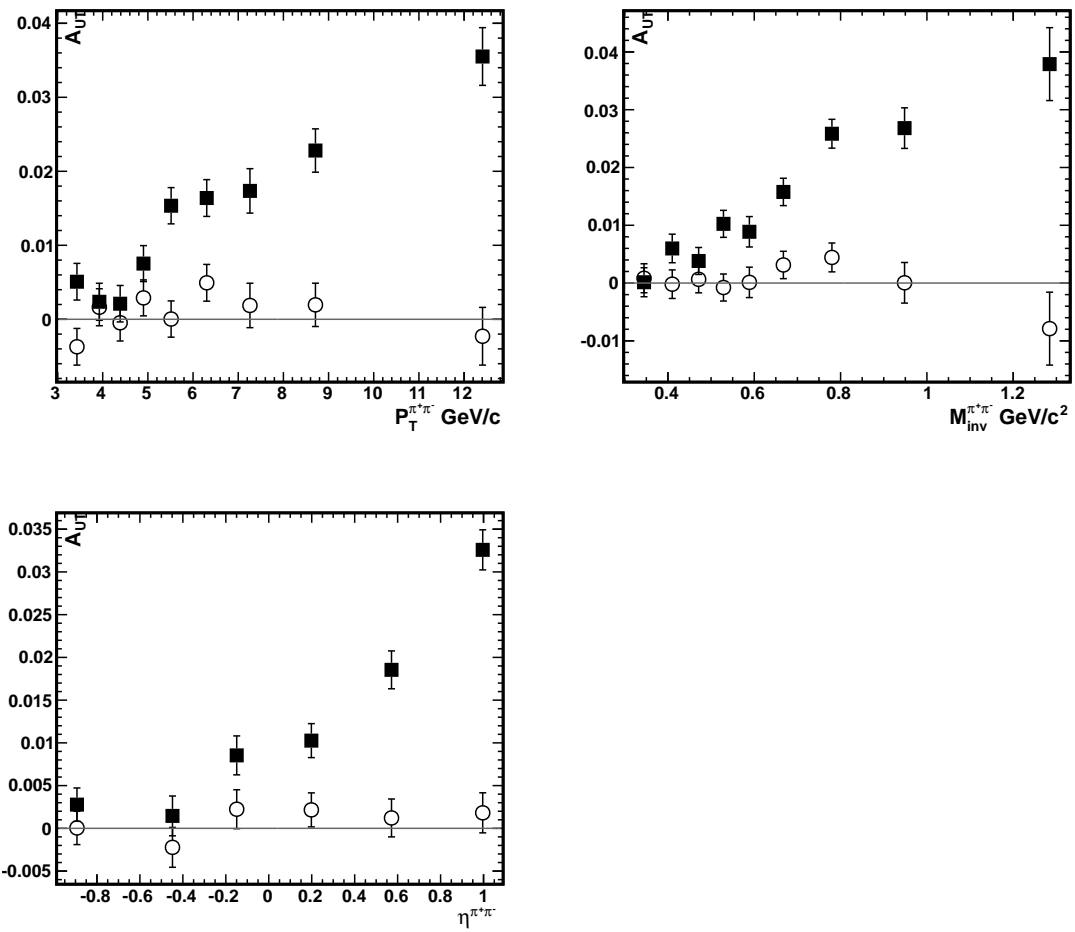


Figure 7.11: Randomly assigned pion charges (open circles) show no sign of asymmetry in any kinematic variable. Correct assignment (solid squares) shown for comparison.  $-2 < \eta^{\pi^+\pi^-} < 2$  for  $P_T^{\pi^+\pi^-}$  and  $M_{inv}^{\pi^+\pi^-}$  plots.

## 7.4 Two Dimensional Kinematic Binning

We were lucky enough to get a much larger data set in 2012. This enabled us to not only break each kinematic variable up into more bins but also bin in multiple kinematic variables at once. This is ideal for extracting the transversity distribution. The asymmetry is determined as a function of  $M_{inv}^{\pi^+\pi^-}$  and  $\eta^{\pi^+\pi^-}$  (figures 7.12 and 7.13, as funtion of  $\eta^{\pi^+\pi^-}$  and  $P_T^{\pi^+\pi^-}$  (figures 7.14 and 7.15, and as a function of  $M_{inv}^{\pi^+\pi^-}$  and  $P_T^{\pi^+\pi^-}$  (figures 7.16 and 7.17. A cone radius cut of 0.7 was used for all 2D binning measurements. There is an  $\eta^{\pi^+\pi^-} > 0$  cut used when measuring the asymmetry as a function of  $M_{inv}^{\pi^+\pi^-}$  and  $P_T^{\pi^+\pi^-}$ .

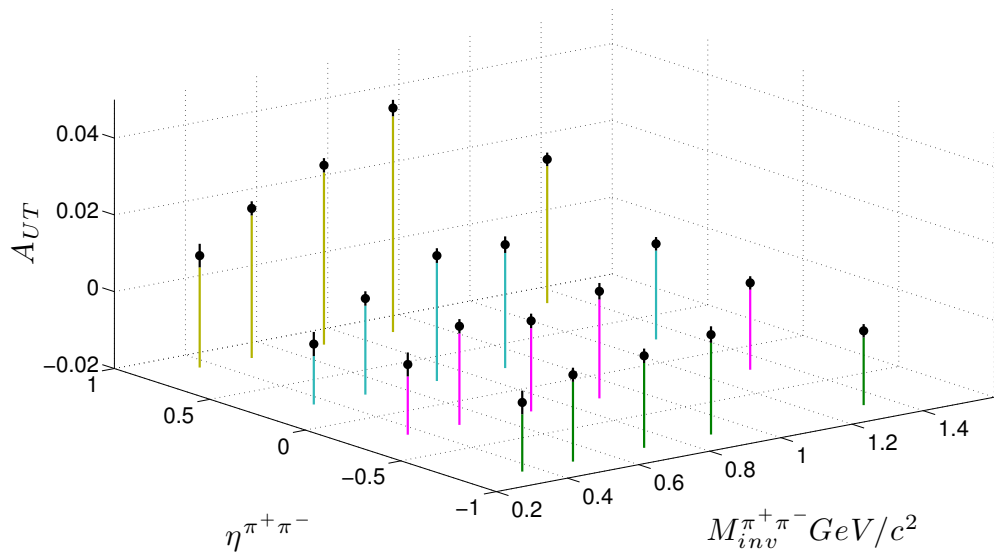


Figure 7.12:  $A_{UT}$  versus  $M_{inv}^{\pi^+\pi^-}$  and  $\eta^{\pi^+\pi^-}$ . Different colored stands denote different  $\eta^{\pi^+\pi^-}$  bins. Note zero is not ground level of the plot.

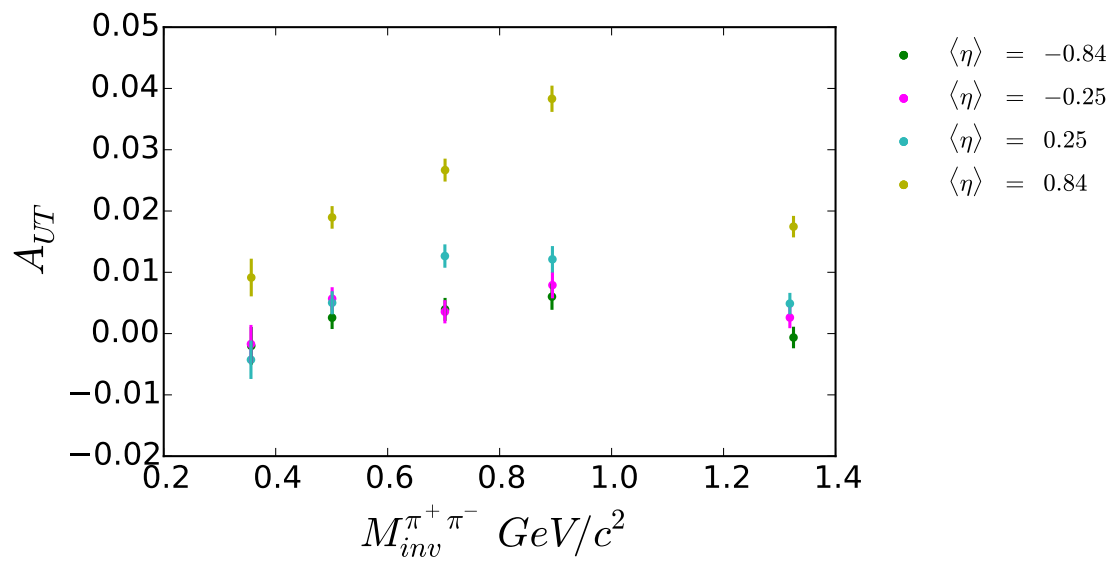


Figure 7.13

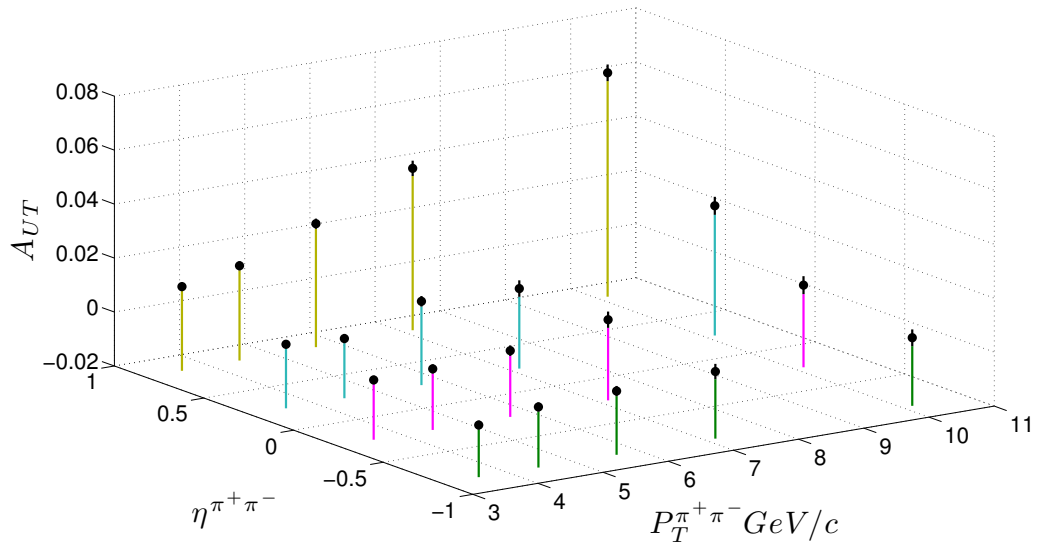


Figure 7.14:  $A_{UT}$  versus  $P_T^{\pi^+\pi^-}$  and  $\eta^{\pi^+\pi^-}$ . Different colored stands denote different  $\eta^{\pi^+\pi^-}$  bins. Note zero is not ground level of the plot.

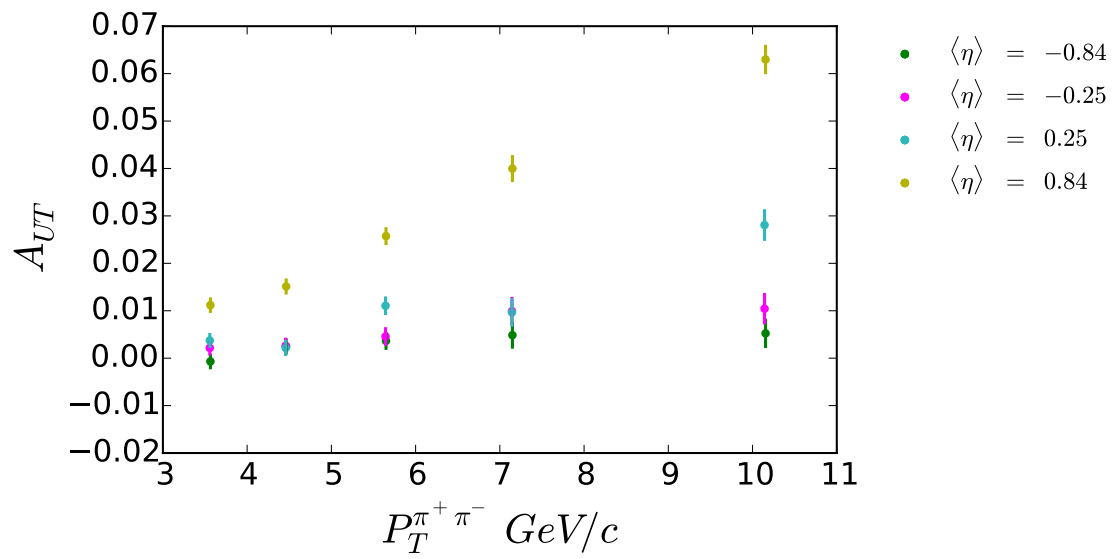


Figure 7.15

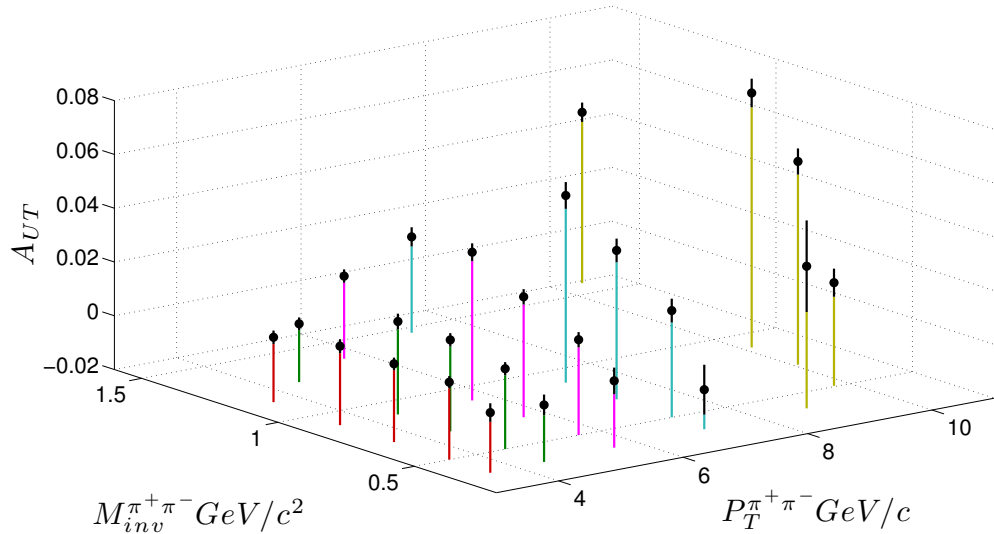


Figure 7.16:  $A_{UT}$  versus  $M_{inv}^{\pi^+\pi^-}$  and  $P_T^{\pi^+\pi^-}$ . Different colored stands denote different  $P_T^{\pi^+\pi^-}$  bins. Note zero is not ground level of the plot. ( $\eta^{\pi^+\pi^-} > 0$ )

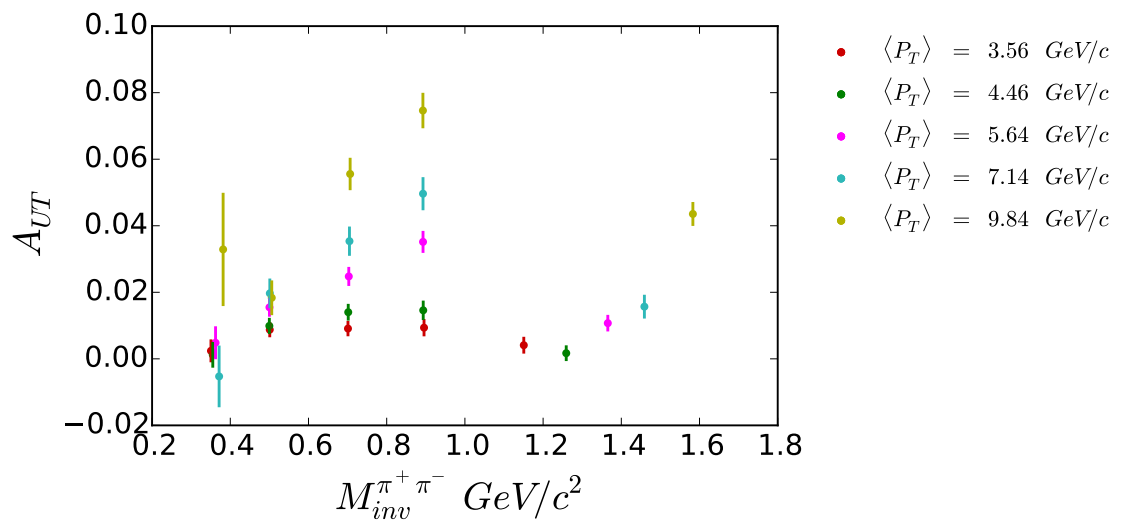


Figure 7.17: ( $\eta^{\pi^+\pi^-} > 0$ )

## 7.5 Asymmetry with partial wave expansion

As stated in chapter 4, the cross section for the scattering process can be expanded.

$$\begin{aligned} \sin \theta H_1^{\triangleleft c}(\bar{z}_c, \cos \theta, M_{inv}^{\pi^+ \pi^- 2}) &\approx H_{1,ot}^{\triangleleft c}(\bar{z}_c, M_{inv}^{\pi^+ \pi^- 2}) \sin \theta \\ &+ H_{1,lt}^{\triangleleft c}(\bar{z}_c, M_{inv}^{\pi^+ \pi^- 2}) \sin \theta \cos \theta \end{aligned} \quad (7.7)$$

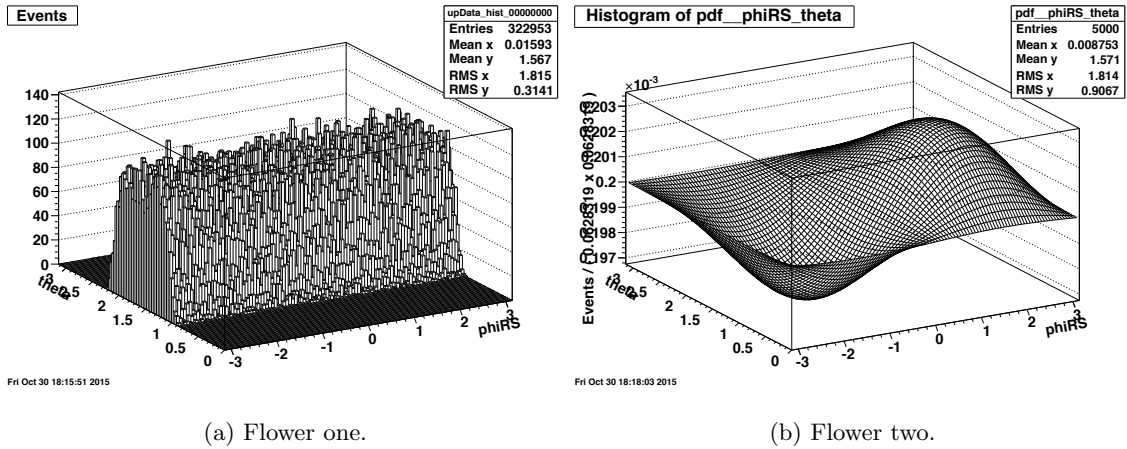
Starting from 6.2, one can come up with a relationship for the yield of pion pairs from spin up and spin down after the expansion. This time the polarization is encapsulated in the asymmetry coefficients  $A_{sp}$  and  $A_{pp}$ .

$$N^\uparrow = L^\uparrow [1 + \sin(\theta) (A_{sp} + A_{pp} \cos(\theta)) \sin(\phi_{RS})] \quad (7.8)$$

$$N^\downarrow = L^\downarrow [1 - \sin(\theta) (A_{sp} + A_{pp} \cos(\theta)) \sin(\phi_{RS})] \quad (7.9)$$

The data was separated into two different sets, one for spin up collisions and one for spin down, and fit simultaneously with the corresponding yield relationship using an unbinned maximum likelihood fit. The luminosity values and asymmetry coefficients are both determined from the fit. As a cross check, the number of pairs from up and down were counted separately can compared to the luminosity values determined from the fit. These were always consistent. A histogram of the data in  $\phi_{RS}$  and  $\theta$  is shown in figure 7.18a, and an example of with the unbinned maximum likelihood fit can be seen in figure 7.18b.

The fitting procedure was done for pairs in the forward direction ( $\eta > 0$ ) in the same invariant mass and transverse momentum bins as the previous section, and the results are shown below. Since the polarization was folded into the asymmetry coefficients in the fit the values here must be scaled by 1/polarization in order to make a fair comparison to the values shown in the previous section. The average polarization for data analyzed is  $|\langle \ell \rangle| = 0.0000$ .



(a) Flower one.

(b) Flower two.

Figure 7.18: Data and unbinned maximum likelihood fit

.55. This puts the black points in figure 7.19 very close to the values seen in the original two dimensional analysis. This makes sense because if  $\theta$  is integrated over, as was the case in the previous 2D binning, only  $A_{sp}$  would survive. The red points corresponding to the  $A_{pp}$  coefficient seem to have no significant difference from zero, and if so, there is certainly no trend noticeable. If one looks hard enough, it seems the sign of  $A_{pp}$  seems to be positive at lower invariant mass and negative at higher invariant mass, the change coming at the  $\rho$  mass. However the size of the error bars make this not significant.

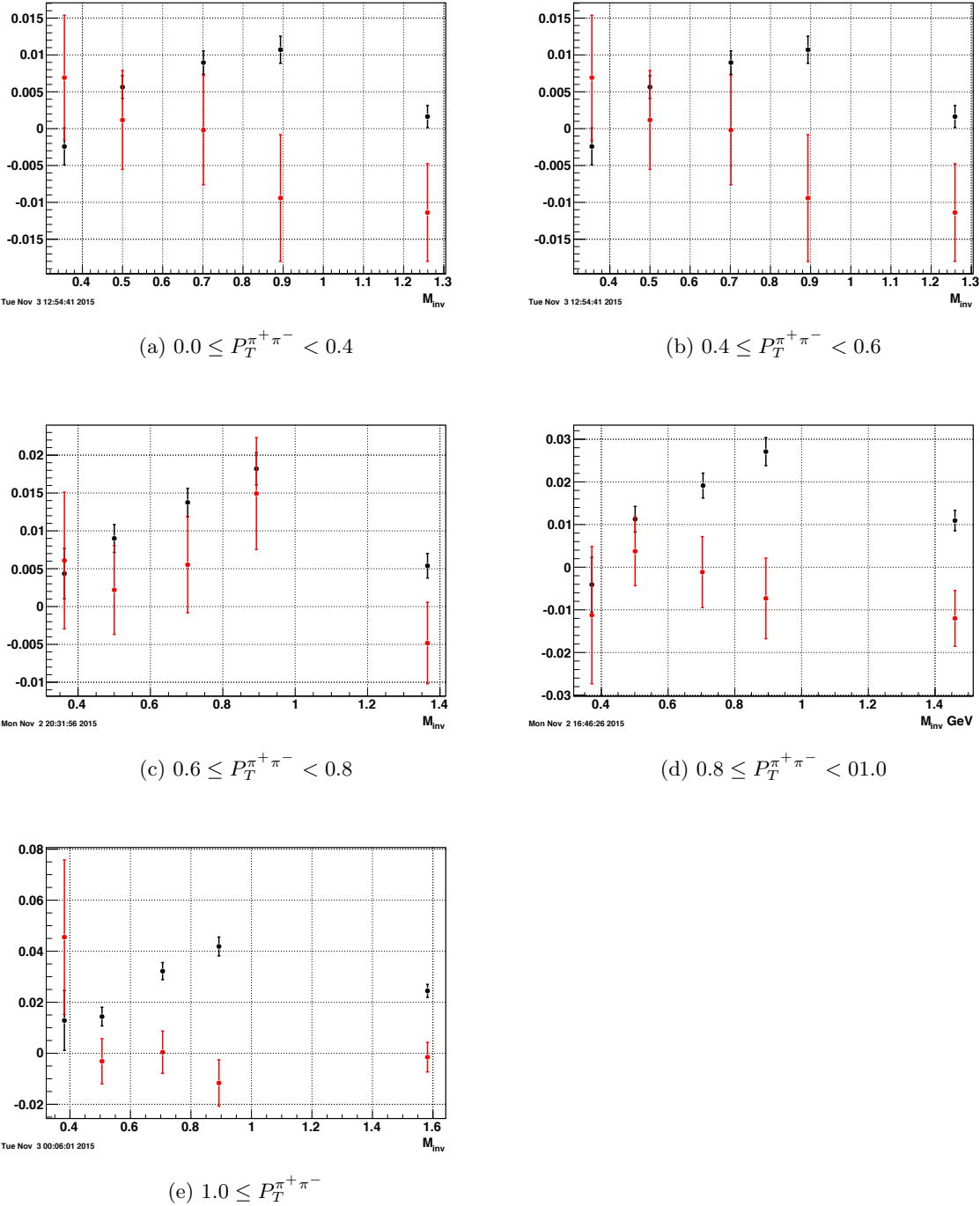


Figure 7.19:  $A_{sp}$  (black) and  $A_{pp}$  (red) vs invariant mass for different  $P_T^{\pi^+\pi^-}$  ranges for pion pairs scattered into the forward ( $\eta > 0$ ) direction

## 7.6 Kaon Pion Pairs

We can perform a similar analysis for other dihadron pairs. In this section, we focus on kaon-pion pairs. Since  $K\pi$  pairs go through an intermediate vector meson  $K^*(892)$  the IFF for the fragmentation of a transversely polarized quark into a kaon and a pion, and therefore observed asymmetry, should be enhanced in this range just like in the  $\rho$  mass range for  $\pi^+\pi^-$  pairs[31].

In the  $\pi^+\pi^-$  pair analysis the identification of pions was relatively simple and unimportant because there are so many more pions than kaons or protons. We attempt to cut as many kaons and protons out as possible and the rest just come as a dilution to the proton sample. It is a lot more difficult to look specifically for kaons. To do this we have to use the ToF as well as the ionization energy loss in the TPC to distinguish between pions and kaons accurately. Figure 7.20 shows a heat map of the particle mass determined by the ToF vs the track  $n_\sigma(\pi)$  determined by the ionization energy loss. This is separated into 11 different track momentum ranges. Looking at the first momentum range in the upper left hand plot, the protons are seen as the faint green region at an time of flight mass of just under one  $\text{GeV}/c^2$ . As expected the pions are located around the bright red region at centered at  $n_\sigma(\pi) = 0$ . The kaons are the faint green region just above and to the left of the pion region. Since protons are so far away from kaons and pions, they are easily removed from the sample with a ToF mass cut. However in order to correctly identify kaons, we need to make a distinction between them and pions.

Looking at each momentum bin individually I constructed the interface between the pion region and the kaon region. I then removed the overlap region where it was impossible to distinguish pions and kaons. This can be seen for the lowest momentum bin in figure ???. Everything between the white lines is not included in the analysis. Particles above

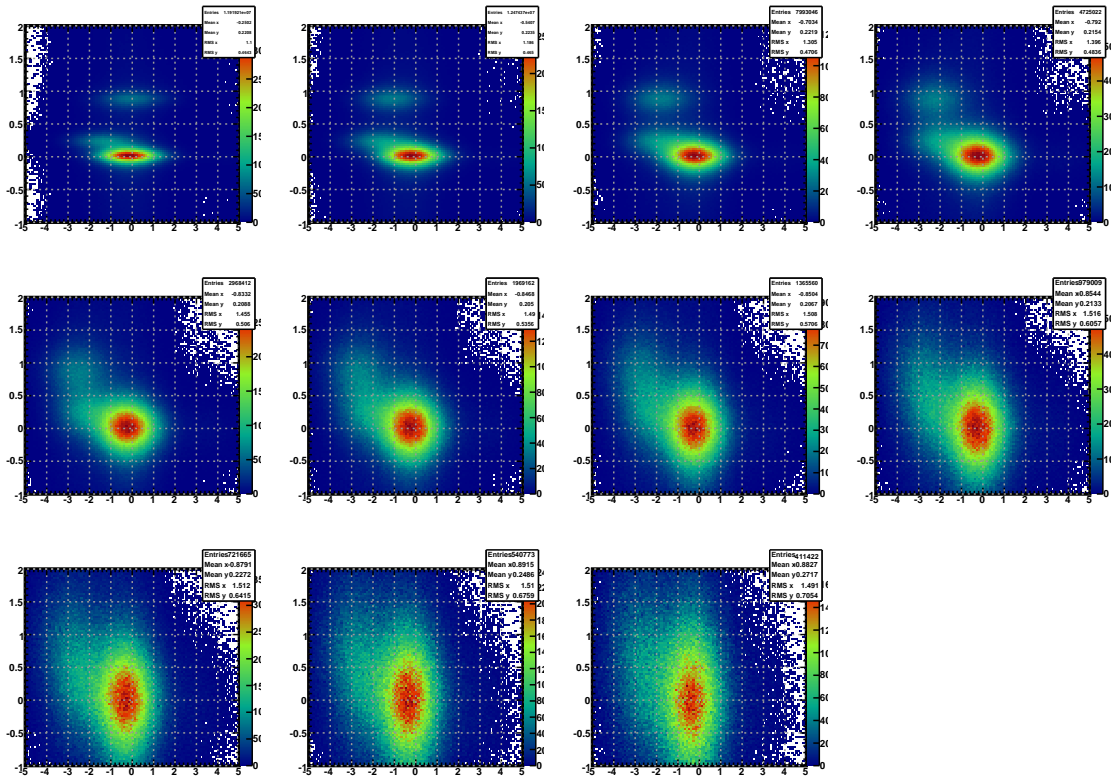


Figure 7.20

the top line is taken to be a kaon, except for the clear proton region which is removed by a horizontal ToF mass cut. Everything below the bottom line is declared a pion. I was able to do this method with varying success for the first four momentum bins. The bin limits can be seen in table ???. The pion, kaon, and sometimes even proton regions in the remaining bins overlapped too much and were not included in the analysis. As the track momentum increases the exclusion region between the white lines increases.

Once  $K\pi$  pairs are found, the analysis continues as in the  $\pi^+\pi^-$  pair case, however with much lower statistics.  $\text{|||how much lower|||}?$  Figure 7.22 shows the asymmetry vs the invariant mass of the  $K\pi$  pair for  $\eta^{K\pi} > 0$ . The lower limit on invariant mass is now 633.25 Mev/ $c^2$  and the invariant mass bins are changed accordingly. The low statistics

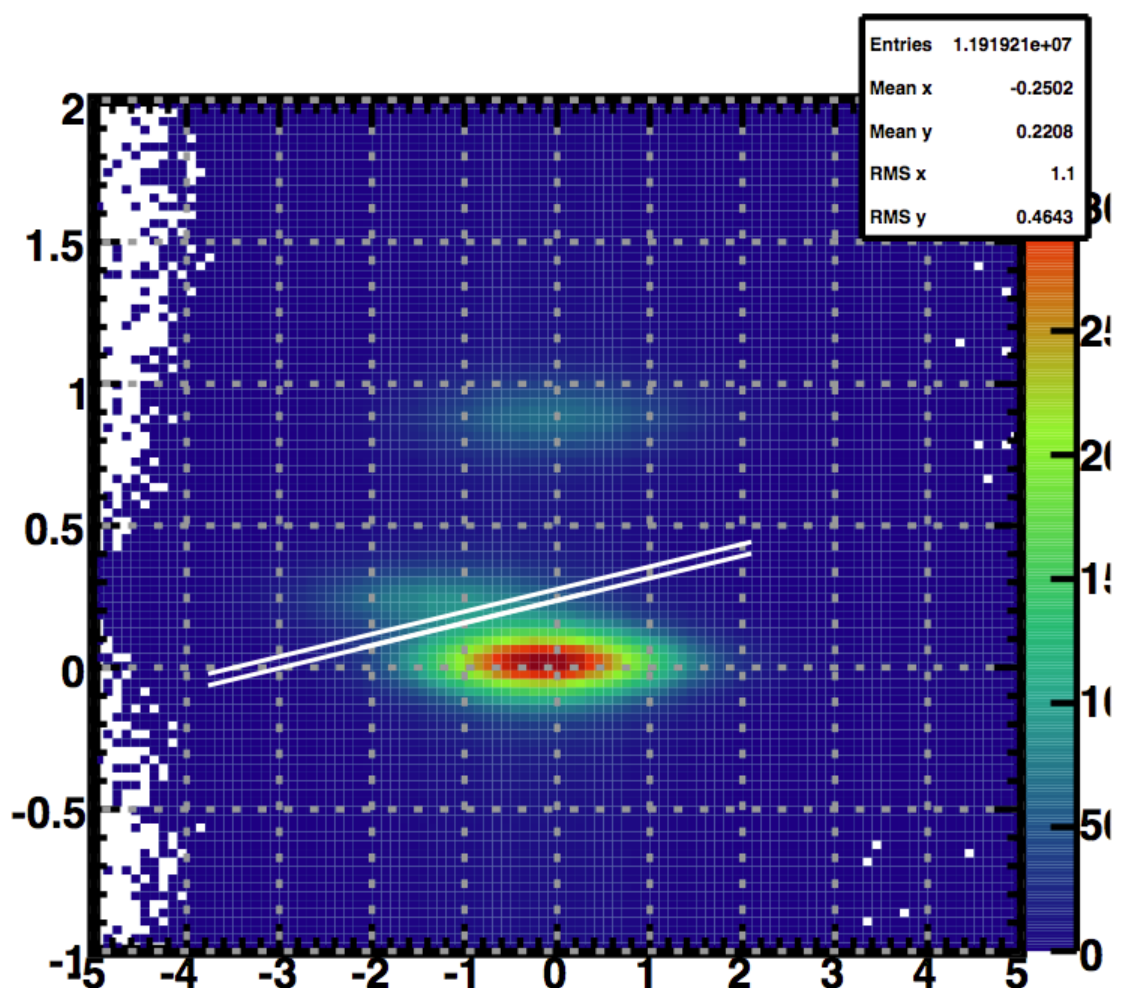


Figure 7.21

Table 7.1: Track momentum bins for  $K\pi$  analysis

1.5	1.9
1.9	2.3
2.3	2.7
2.7	3.1

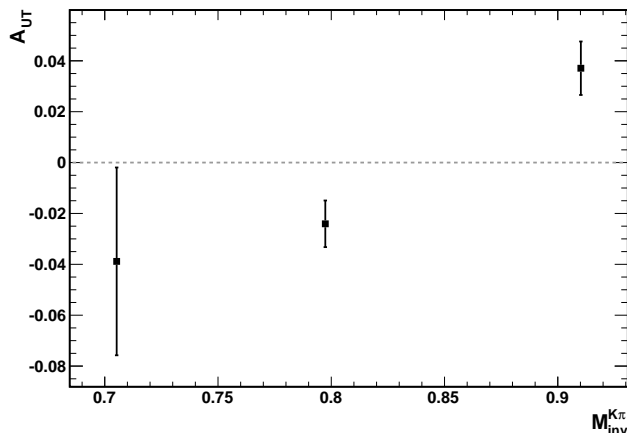


Figure 7.22: Asymmetry vs Invariant Mass for Kaon Pion Pairs. Nonzero asymmetry is only seen in the mass bin containing the  $K^*(892)$  mass.  $\eta^{K\pi} > 0$

only allow for three invariant mass bins. Any more results in huge error bars in the largest bin. Just like the  $\pi^+\pi^-$  pair scenario, we expect an enhancement to the asymmetry in the vicinity of  $K^*$  mass ( $892 \text{ MeV}/c^2$ ). As you can see in figure 7.22, we do see an enhancement in this mass region, however we also see a sizable negative asymmetry in the mass region directly before it. This leads me to believe the asymmetry near the  $K^*$  mass may just be due to statistical fluctuations and our low statistics. More investigation is needed to make a clear statement.

We know from the  $\pi^+\pi^-$  pair case that the asymmetry should increase with the pseudo-rapidity of the pair. In figure 7.22 we had a lower  $\eta^{K\pi}$  limit of 0. If we increased the lower

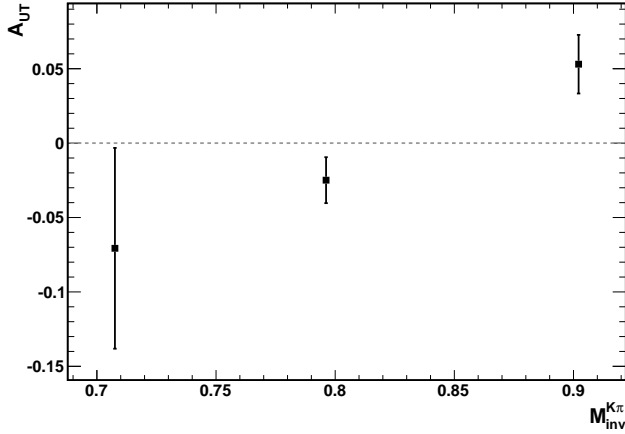


Figure 7.23: Asymmetry vs Invariant Mass for Kaon Pion Pairs. Nonzero asymmetry is only seen in the mass bin containing the  $K^*(892)$  mass.  $\eta^{K\pi} > 0.50$

limit, we should see an increase in the asymmetry. Seeing an increase in the asymmetry near the  $K^*$  could be evidence that the asymmetry is real and not a product of statistical fluctuations. The asymmetry when  $\eta^{K\pi} > 0.5$  can be seen in figure 7.23.

The third mass bin has an asymmetry of  $0.0530 \pm 0.0197$  when the lower  $\eta^{K\pi}$  limit is 0.5 and  $0.0371 \pm 0.0105$  when the lower  $\eta^{K\pi}$  limit is 0. This suggests the asymmetry in this bin is an actual asymmetry. Not only that but the asymmetry in the second bin has decreased when the lower  $\eta^{K\pi}$  limit was changed to 0.5.

In the  $\pi^+\pi^-$  analysis the pions were ordered by electric charge; the positive pion always chosen to be hadron 1 in the calculation of the vector  $\mathbf{R}$  (refer to chapter 4). In the  $K\pi$  analysis, it is not so clear. The two particles could be ordered by charge or by particle type. As a check, the asymmetry was determined in  $K^+\pi^-$  and  $K^-\pi^+$  pairs separately when using charge ordering. This can be seen in figure 7.24. With the exception of the lowest mass bin, which is hindered by low statistics, the asymmetry is equivalent between  $K^+\pi^-$  and  $K^-\pi^+$  pairs. This suggest that charge ordering is correct, which is the expected result.

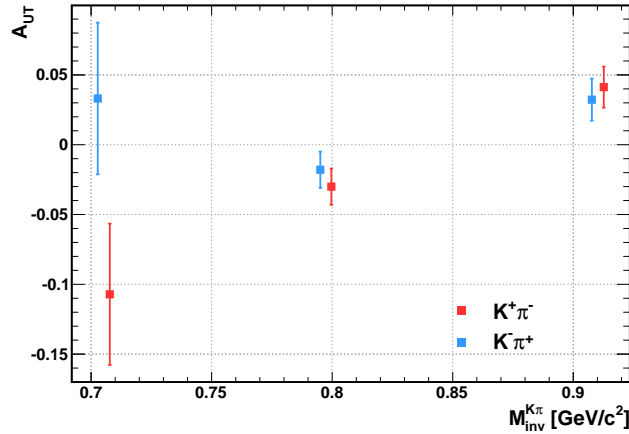


Figure 7.24: Asymmetry vs Invariant Mass for different charge combinations of Kaon Pion Pairs.  $\eta^{K\pi} > 0$

As with the pion pair analysis, I would like to explore the effect of the radius cut on the asymmetry. Since there is only one invariant mass bin with a significant asymmetry, I look at the asymmetry in this bin for different radii. In the pion analysis, the lowest radius cut (0.2) resulted in the highest observed asymmetries. In the  $K\pi$  analysis, this same radius cut results in zero observed asymmetry. To investigate this more deeply, I measured the asymmetry at the same three used in the pion analysis (0.2, 0.3, 0.4) as well as other intermediate values of the radius cut. The results are shown in figure 7.25. Like the pion analysis, the asymmetry decreases with increasing radius cut, with the exception of the smallest cuts. Since only three radii were used in the pion analysis, it is not clear whether a decrease in asymmetry would have been seen at lower radii. This may be something to investigate, as it could give insight into very low Z behavior of the IFF.

Unfortunately this is all we have done so far for  $K\pi$  pairs. The statistics are so low that we can not do a multivariable analysis as we did for  $\pi^+\pi^-$  pairs. Since the only nonzero asymmetry we see is in the vicinity of  $K^*$  integrating over the invariant mass washes out any asymmetry we see. Thus investigating how the asymmetry behaves with

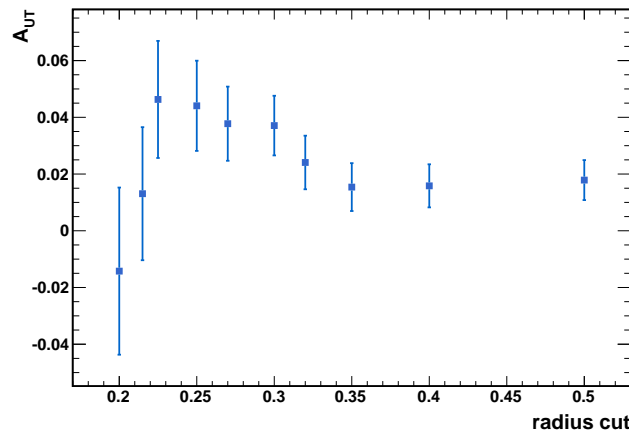


Figure 7.25: Asymmetry vs radius cut for the highest invariant mass bin.  $\eta^{K\pi} > 0$

$P_T^{K\pi}$  or  $\eta^{K\pi}$  when the invariant mass is integrated over results in zero asymmetry. With more statistics it would be interesting to look at how varying the transverse momentum affects the asymmetry near  $K^*$ .

## 8 Theoretical Predictions

With the IFF extracted from electron positron annihilation at BELLE (see 2.6) half the puzzle is complete. Once the IFF is known the transversity distribution can be extracted, also using the replica method [10], from the observed asymmetry in dihadrod leptonproduction [39]. Combining the results of the extraction of the IFF and the transversity distribution, Radici et. al. made predictions for the observed asymmetry in hadron collisions [37] by replacing the IFF and the transversity distribution in

$$A_{UT} = 2P_T^{\pi^+\pi^-} \sum_{a,b,c,d} \frac{|\mathbf{R}|}{M_{inv}^{\pi^+\pi^-}} \int \frac{dx_a dx_b}{16\pi z_c} f_1(x_a) h_1(x_b) \frac{d\Delta\hat{\sigma}_{ab\uparrow \rightarrow c\uparrow d}}{d\hat{t}} H_1^{\triangleleft c}(\bar{z}_c, M_{inv}^{\pi^+\pi^-}) \quad (8.1)$$

with the extracted replica. These replicas are first evolved to the STAR transverse momentum scale using the DGLAP evolution equations [37].

### 8.0.1 Predictions for 2006

Predictions for  $A_{UT}$  as a function of invariant mass of the  $\pi^+\pi^-$  pair is shown in figure 8.1. The grey band corresponds to the predicted value of 68% of the replicas. It is superimposed behind the data points shown in figure 5.1 for  $\eta > 0$ . The 68% replica band does well to predict the data. The prediction for  $A_{UT}$  as a function of  $\eta^{\pi^+\pi^-}$  can be seen in figure 8.2. The convention used is opposite to the one used in this thesis - the direction

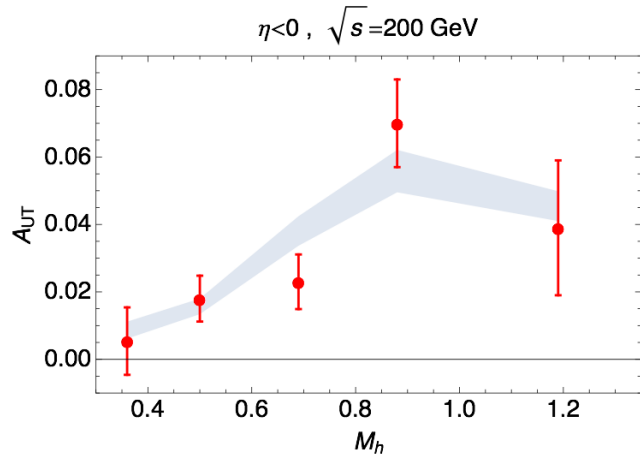


Figure 8.1

of the polarized beam is taken to be in the negative  $\eta$  direction. The 68% replica band doesn't do as well to predict the results especially in the most forward direction. Three replicas (6, 31, and 43) are shown that fall outside the 68% replica band but predict the result with more accuracy.

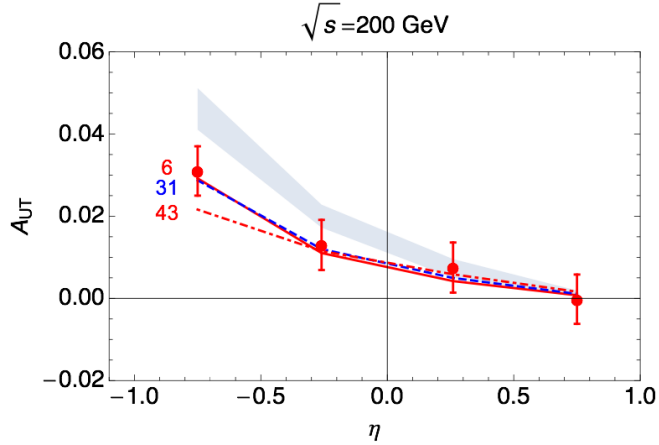


Figure 8.2

### 8.0.2 Predictions for 2012

The predictions for 2012 are done in the same manor as for 2006. With more data from the 2012 production, these predictions can be put to another test. Figure 8.3 shows the prediction values of  $A_{UT}$  as a function of  $\eta^{\pi^+\pi^-}$  and the 2012 data points shown in figure 7.3. This time the predicted 68% replica band perfectly predicts the data. In figure 8.4, the prediction for  $A_{UT}$  is shown as a function of  $M_{inv}^{\pi^+\pi^-}$  along with the 2012 data for  $\pi^+\pi^-$  pairs in the direction of the polarized beam ( $\eta^{\pi^+\pi^-} < 0$  in the convention of the authors). There is a slight discrepancy between the prediction and the 2012 data at larger  $M_{inv}^{\pi^+\pi^-}$ . There is also one data point from 2012 at higher  $M_{inv}^{\pi^+\pi^-}$  that has been left off. This data point, which can be see in figure ?? at  $M_{inv}^{\pi^+\pi^-} > 1.2$ , would disagree with the prediction even further. Figure 8.5 shows the prediction for pairs in the backwards direction as the polarized beam. Here the predictions do a better job.

The accuracy seen in these predictions, although not incredible, hints at the universality of the transversity distribution function. In the near future, the transversity distribution will be able to be extracted from a global fit of the STAR data in conjunction with

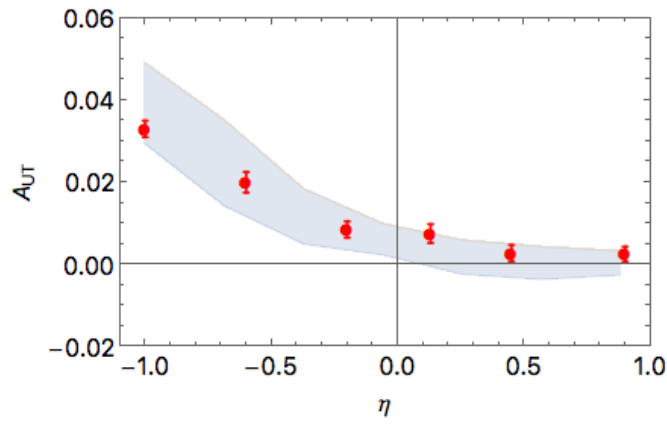


Figure 8.3

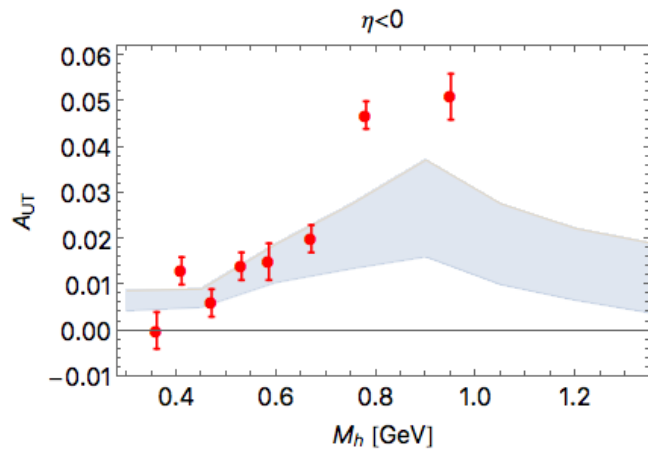


Figure 8.4

the HERMES/COMPASS data [37]. This should give us the best understanding of the transversity distribution to date.

IS THIS NOW USING THE 2006 DATA TO EXTRACT/MAKE PREDICTIONS  
ALONG WITH THE ep AND ee STUFF???

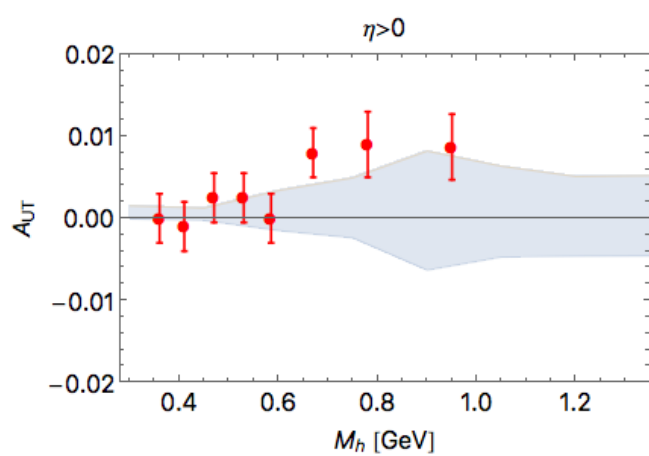


Figure 8.5

## 9 Pythia Tune Selection

Typically additional information is needed to frame experimental results which are not accessible experimentally. For this purpose we use embedding with events generated by Pythia and detector simulation with Geant. This year much work was done by Kevin Adkins to select Pythia settings in such a way that the simulated events reflect the actual data as well as possible.

The first step was selecting which Pythia tune produced particle yields most comparable to the STAR data. A total of five tunes were investigated. Figure 9.1 shows the ratio of  $\pi^+$  yields in simulation to real data as a function of transverse momentum. Perugia 0 seems to be the worst fit out of all the tunes. The only Pythia tune to match at low  $p_T$  is CDF Tune A which doesn't match for higher  $p_T$ . Perugia 2012 seems to be the best fit overall even though it doesn't match at low  $p_T$ .

One idea is to decrease the value of the primordial  $k_T$  in Perugia 0 which has a high default  $k_T$  value at 2 GeV/c. This parameter accounts for the infrared effects.[43] The suitability of Perugia 0 is drastically increased when changing this parameter from 2 GeV/c to 0.5 GeV/c as seen in figure 9.2. It seems as though this corrected disagreement at low  $p_T$  as caused Perugia 0 to be satisfactory fit at higher  $p_T$  as well. In fact it worked so well that the primordial  $k_T$  was decreased to 0.5 GeV/c in Perugia 2012 and Perugia 6 as well. As with Perugia 0, low  $p_T$  yields for Perugia 2012 is corrected with the change

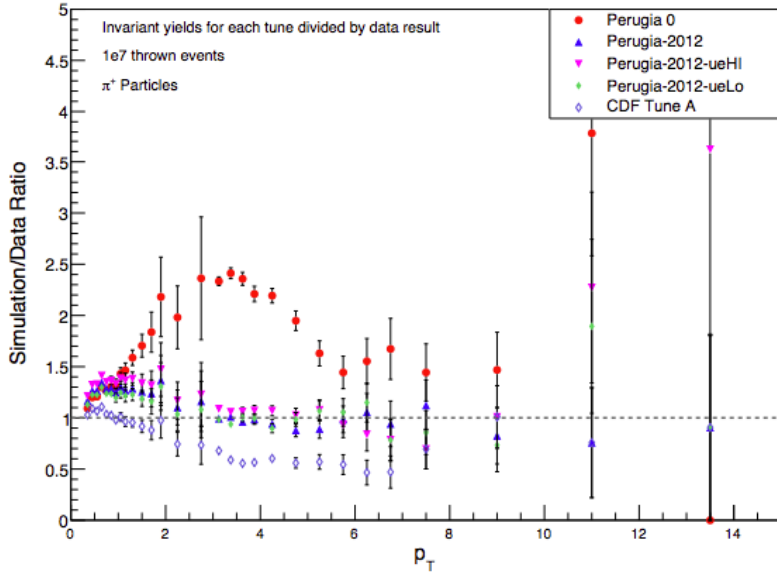


Figure 9.1: Ratio of simulated pion yield to real data pion yield for five different Pythia tunes as a function of pion transverse momentum.

in primordial  $k_T$  ???. It is possible that, although it corrects particle yields, altering the default primordial  $k_T$  value could have adverse effects on different properties of the data. Because of this we want to keep in mind the Pythia tune which performs best at nominal  $k_T$ . This seems to be Perugia 2012 as seen in figure 9.1.

With two possible tunes in hand we investigate the effect of our choice of parton distribution function set. Figure 9.4 shows the  $\pi^+$  yield ratio for default PDF sets for nominal  $k_T$  and for reduced  $k_T$ . By comparing the yield ratio of the default PDF set to other we find the most suitable PDF set to be NNPDF 3.0 Lo for nominal  $k_T$  Perugia 2012 shown in figure 9.5, and CT10 for reduced  $k_T$  and Perugia 0 shown in figure 9.6

So the two candidates are Perugia 0 with PDF set CT10 and reduced  $k_T$  and Perugia 2012 with PDF set NNPDF 2.0 Lo and nominal  $k_T$ . The next thing to look at is if each generates jets with subprocess fractions in a correct manner. Figure 9.7 shows how the Pythia subprocess fractions compare to NLO theoretical curves for both candidates. It is

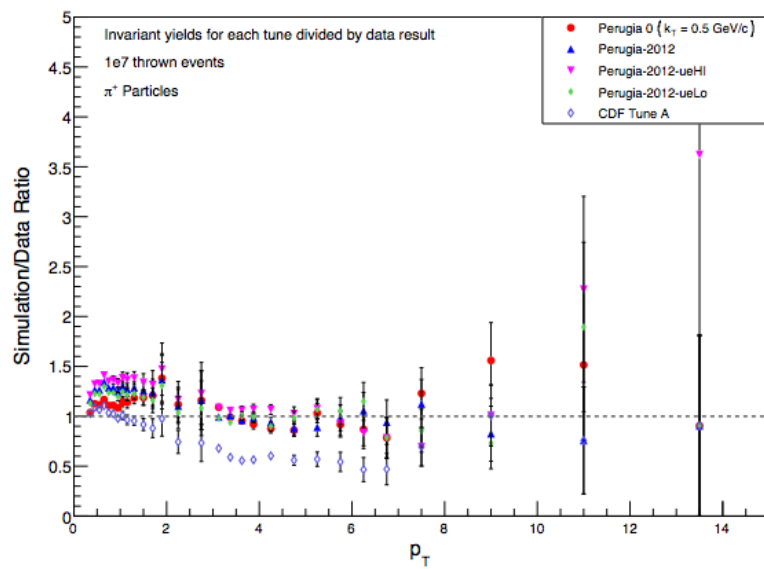


Figure 9.2: Ratio of simulated pion yield to real data pion yield for five different Pythia tunes as a function of pion transverse momentum with reduced  $k_T$  for Perugia 0.

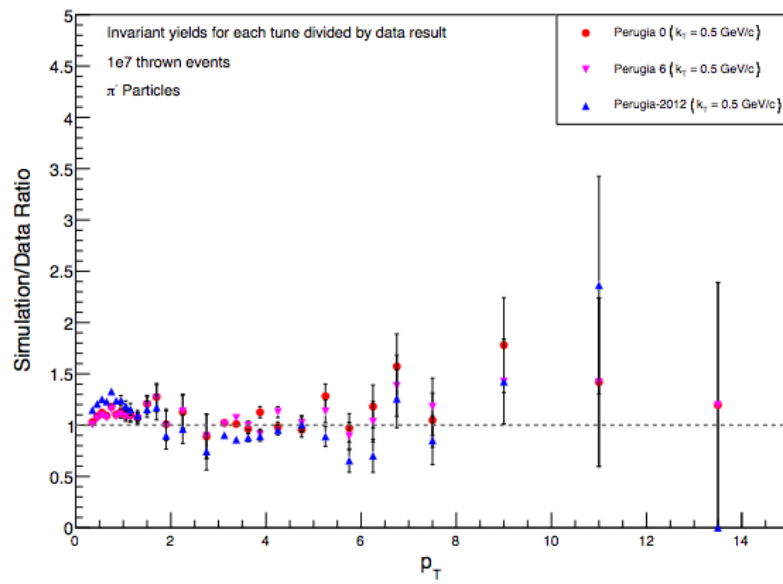


Figure 9.3: Ratio of simulated pion yield to real data pion yield for best three Pythia tunes as a function of pion transverse momentum all with reduced  $k_T$ .

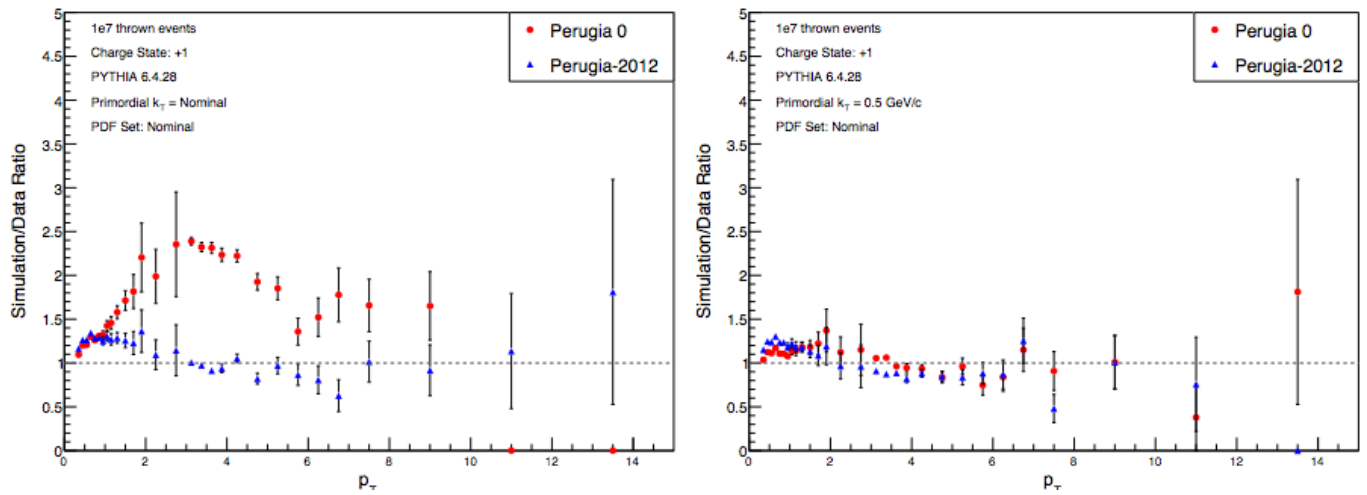


Figure 9.4: Pion yield ratios for Perugia 0 and Perugia 2012 for nominal  $k_T$  and reduced  $k_T$ .

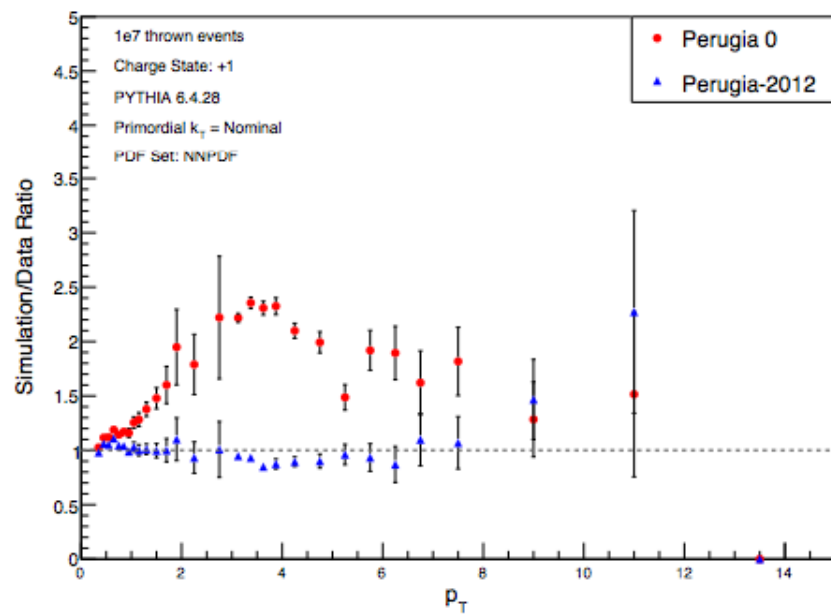


Figure 9.5: The best PDF set for Perugia 2012 and nominal  $k_T$  is NNPDF 3.0 Lo.

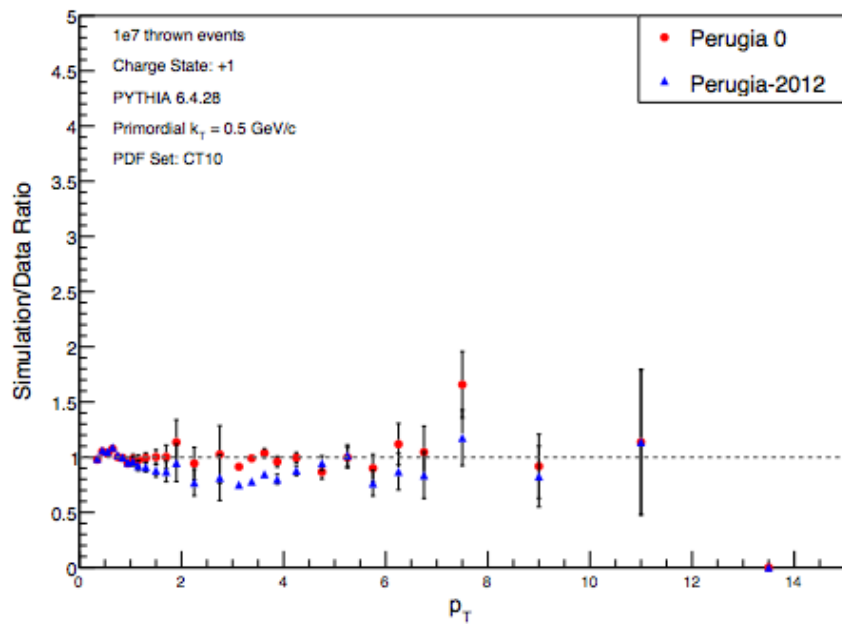


Figure 9.6: The best PDF set for Perugia 0 and reduced  $k_T$  is CT10.

clearly seen that Perugia 0 matches the theoretical curves much better than Perugia 2012.

After this investigation we will chose Perugia 0 with PDF set CT10 and reduced  $k_T$  to generate the simulated data for the embedding analysis.

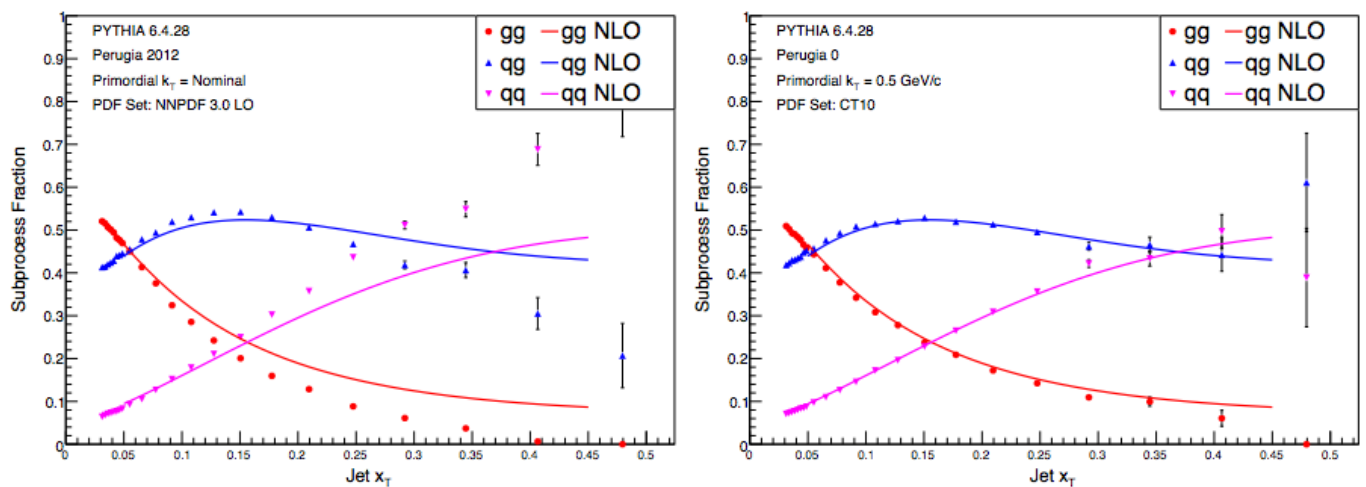


Figure 9.7

## **10 Embedding Analysis**

not sure if I want to split this up into two sections like I have. embedding analysis and trigger bias.

## 11 Trigger Bias

The way the STAR triggers select events introduces a bias to our sample. It does this in two ways. First, it can trigger on quark jets and gluon jets in a different ratio than they are produced in the collisions. This is important to quantify because theorist interpreting results from this analysis will assume the ratio of quark jets to gluon jets is consistent with the ratio they are produced at. To investigate how this affects the asymmetry we will start by revisiting equations 6.2 through 6.5. It is convenient to introduce two variables  $g = N_g/2\pi$  and  $q = N_q/2\pi$ , where  $N_g$  and  $N_q$  are the total number of pion pairs from gluons jets and quark jets at any angle  $\phi_{RS}$ . Since pairs from gluons don't contribute to the asymmetry, the number of gluon jets at any angle  $\phi_{RS}$  is simply  $g$ . There is no sinusoidal modulation as you would see with the number of pion pairs from fragmenting quarks. Using these two new variables, equations 6.2 through 6.5 can be rewritten as:

$$N_{\phi_{RS}}^{\uparrow} = L^{\uparrow} I_{\phi_{RS}}(\theta) [g + q + q A_{UT} P \sin(\phi_{RS})] \quad (11.1)$$

$$N_{\phi_{RS}}^{\downarrow} = L^{\downarrow} I_{\phi_{RS}}(\theta) [g + q - q A_{UT} P \sin(\phi_{RS})] \quad (11.2)$$

$$N_{\phi_{RS}+\pi}^{\downarrow} = L^{\downarrow} I_{\phi_{RS}+\pi}(\theta) [g + q + q A_{UT} P \sin(\phi_{RS})] \quad (11.3)$$

$$N_{\phi_{RS}+\pi}^{\uparrow} = L^{\uparrow} I_{\phi_{RS}+\pi}(\theta) [g + q - q A_{UT} P \sin(\phi_{RS})] \quad (11.4)$$

By defining  $\mathcal{L}$  and  $\mathcal{R}$  in the same manor as before,

$$\frac{\mathcal{L} - \mathcal{R}}{\mathcal{L} + \mathcal{R}} = \frac{\sqrt{N_{\phi_{RS}}^{\uparrow} N_{\phi_{RS}+\pi}^{\downarrow}} - \sqrt{N_{\phi_{RS}}^{\downarrow} N_{\phi_{RS}+\pi}^{\uparrow}}}{\sqrt{N_{\phi_{RS}}^{\uparrow} N_{\phi_{RS}+\pi}^{\downarrow}} + \sqrt{N_{\phi_{RS}}^{\downarrow} N_{\phi_{RS}+\pi}^{\uparrow}}} = f_q^{detector} A_{UT} P \sin(\phi_{RS}) \quad (11.5)$$

where  $f_q^{detector} = \frac{q}{q+g}$  is the fraction of pion pairs originating from quarks after trigger selection has occurred. So what was measured in the analysis should actually be thought of as  $A_{UT}^{experiment} = f_q^{detector} A_{UT}$ , where  $A_{UT}$  is now the “true” asymmetry.

The theorist will have a similar result,

$$\frac{\mathcal{L} - \mathcal{R}}{\mathcal{L} + \mathcal{R}} = \frac{\sqrt{N_{\phi_{RS}}^{\uparrow} N_{\phi_{RS}+\pi}^{\downarrow}} - \sqrt{N_{\phi_{RS}}^{\downarrow} N_{\phi_{RS}+\pi}^{\uparrow}}}{\sqrt{N_{\phi_{RS}}^{\uparrow} N_{\phi_{RS}+\pi}^{\downarrow}} + \sqrt{N_{\phi_{RS}}^{\downarrow} N_{\phi_{RS}+\pi}^{\uparrow}}} = f_q^{collision} A_{UT} P \sin(\phi_{RS}). \quad (11.6)$$

This time  $f_q^{collision}$  is the fraction of pion pairs originating from quarks before triggers are taken into account. Their perception of the asymmetry is  $A_{UT}^{theory} = f_q^{collision} A_{UT}$ . From this, it can be seen that

$$A_{UT}^{experiment} = \frac{f_q^{detector}}{f_q^{collision}} A_{UT}^{theory}. \quad (11.7)$$

The values for  $f_q^{detector}$  and  $f_q^{theory}$  can be determined from simulated data.

The main triggers I use in my analysis are the barrel jet patch triggers and the barrel high tower triggers. These triggers are fired when there is substantial amount of energy deposited in one or a group of towers. This happens when there are a lot of high energy neutral particles in the event. This occurs more often in gluon jets than in quark jets. This causes the data set to have a skewed percentage of quark and gluon jets than in reality. Since gluons carry no transversity , the results actually under represent the asymmetry. In reality, if the number of quark and gluon jets matched with the actual production, we would see a higher asymmetry.  To account for this, we use embedding to determine the ratio of pion pairs coming from a quark to the number coming from a

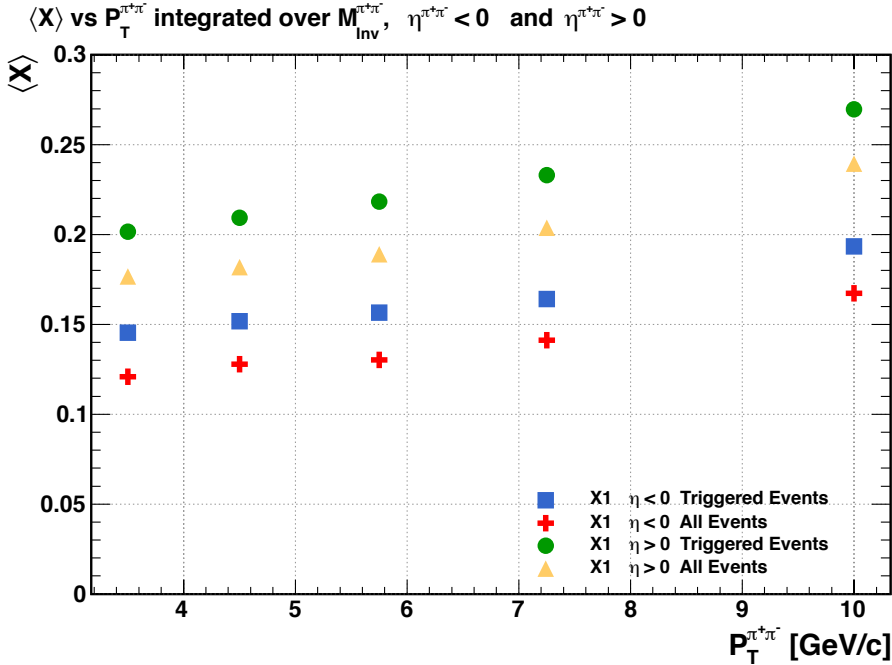


Figure 11.1: The average momentum fraction  $x$  of the polarized quark (quark 1) is larger for triggered events than for all events. This effect is seen if both the forward and backward directions and for all  $\pi^+\pi^-$  transverse momenta. Note this figure is from the 2006 set up

gluon when the triggers are turned off and when the triggers are turned on. This gives us an idea of how the triggers bias the data set.

The trigger also has a bias toward events coming from a parton carrying a high momentum fraction  $x$ . A quark with a large  $x$  will lead to outgoing products carrying more energy. These products will have a greater chance to be over the trigger threshold. This bias toward higher  $X$  events is shown in figure 11.1.

## **12 discussion**

testing bibliography [43] [27] [41] [28] [4] [10] [45] [16] [7] [17] [2] [34] [22] [21] [35] [6]  
[44] [33] [26] [36] [24] [12] [20] [31] [46] [40] [18] [42] [14] [3] [9] [32] [23] [11]

# Bibliography

- [1] K. Abe et al. “Measurements of the proton and deuteron spin structure functions  $g(1)$  and  $g(2)$ ”. In: *Phys. Rev.* D58 (1998), p. 112003. DOI: [10.1103/PhysRevD.58.112003](https://doi.org/10.1103/PhysRevD.58.112003). arXiv:[hep-ph/9802357](https://arxiv.org/abs/hep-ph/9802357) [hep-ph].
- [2] K.H. Ackermann et al. “STAR detector overview”. In: *Nuclear Instruments and Methods in Physics Research A* 499 (2003), pp. 624–632. URL: [http://dx.doi.org/10.1016/S0168-9002\(02\)01960-5](http://dx.doi.org/10.1016/S0168-9002(02)01960-5).
- [3] L. Adamczyk et al. “Observation of Transverse Spin-Dependent Azimuthal Correlations of Charged Pion Pairs in  $p^\uparrow + p$  at  $\sqrt{s} = 200$  GeV”. In: *Phys. Rev. Lett.* 115 (24 2015), p. 242501. DOI: [10.1103/PhysRevLett.115.242501](https://doi.org/10.1103/PhysRevLett.115.242501). URL: <http://link.aps.org/doi/10.1103/PhysRevLett.115.242501>.
- [4] A. Airapetian et al. “Measurement of the Proton Spin Structure Function  $g_1^p$  with a Pure Hydrogen Target”. In: *Phys.Lett.B* 442 (1998), pp. 484–492. URL: <http://arxiv.org/abs/hep-ex/9807015v1>.
- [5] A. Airapetian et al. “Single-spin asymmetries in semi-inclusive deep-inelastic scattering on a transversely polarized hydrogen target”. In: *Phys. Rev. Lett.* 94 (2005), p. 012002. DOI: [10.1103/PhysRevLett.94.012002](https://doi.org/10.1103/PhysRevLett.94.012002). arXiv:[hep-ex/0408013](https://arxiv.org/abs/hep-ex/0408013) [hep-ex].

- [6] Marco Radici Alessandro Bacchetta. “Dihadron interference fragmentation functions in proton-proton collisions”. In: *Phys. Rev. D* 70 (3 2004). URL: DOI : 10 . 1103 / PhysRevD.70.094032.
- [7] M. Anderson et al. “The STAR time projection chamber: a unique tool for studying high multiplicity events at RHIC”. In: *Nuclear Instruments and Methods in Physics Research A* 499 (2003), pp. 659–678. URL: <http://arxiv.org/abs/nucl-ex/0301015>.
- [8] M. Anselmino et al. “Transversity and Collins functions from SIDIS and e+ e- data”. In: *Phys. Rev. D* 75 (2007), p. 054032. DOI: 10 . 1103 / PhysRevD.75.054032. arXiv:hep-ph/0701006 [hep-ph].
- [9] F. Arbabifar et al. “Symmetry breaking effect on determination of polarized and unpolarized parton distributions”. In: (2012). [Nucl. Phys. Proc. Suppl. 234, 66 (2013)]. DOI: 10 . 1016 / j . nuclphysbps . 2012 . 11 . 016. arXiv:1208.5234 [hep-ph].
- [10] Marco Radici Aurore Courtoy Alessandro Bacchetta and Andrea Bianconi. “First extraction of Interference Fragmentation Functions from  $e^+e^-$  data”. In: *Phys. Rev. D* 85 (2012). URL: <http://arxiv.org/abs/1202.0323>.
- [11] Alessandro Bacchetta. “Probing the Transverse Spin of Quarks in Deep Inelastic Scattering”. PhD thesis. Vrije U., Amsterdam, 2002. arXiv:hep-ph/0212025 [hep-ph]. URL: [https://inspirehep.net/record/594456/files/arXiv:hep-ph\\_0212025.pdf](https://inspirehep.net/record/594456/files/arXiv:hep-ph_0212025.pdf).
- [12] Alessandro Bacchetta and Marco Radici. “Modeling dihadron fragmentation functions”. In: *Phys. Rev. D* 74 (11 2006), p. 114007. DOI: 10 . 1103 / PhysRevD.74.114007. URL: <http://link.aps.org/doi/10.1103/PhysRevD.74.114007>.

- [13] Alessandro Bacchetta and Marco Radici. “Partial wave analysis of two hadron fragmentation functions”. In: *Phys. Rev.* D67 (2003), p. 094002. doi: 10.1103/PhysRevD.67.094002. arXiv:hep-ph/0212300 [hep-ph].
- [14] Alessandro Bacchetta et al. “Asymmetries involving dihadron fragmentation functions: From DIS to  $e^+e^-$  annihilation”. In: *Phys. Rev. D* 79 (3 2009), p. 034029. doi: 10.1103/PhysRevD.79.034029. URL: <http://link.aps.org/doi/10.1103/PhysRevD.79.034029>.
- [15] Vincenzo Barone, Alessandro Drago, and Philip G. Ratcliffe. “Transverse polarisation of quarks in hadrons”. In: *Phys. Rept.* 359 (2002), pp. 1–168. doi: 10.1016/S0370-1573(01)00051-5. arXiv:hep-ph/0104283 [hep-ph].
- [16] M. Beddoa et al. “The STAR Barrel Electromagnetic Calorimeter”. In: *Nuclear Instruments and Methods in Physics Research A* 499 (2003), pp. 725–739. URL: [http://dx.doi.org/10.1016/S0168-9002\(02\)01970-8](http://dx.doi.org/10.1016/S0168-9002(02)01970-8).
- [17] F. Bergsmaa et al. “The STAR detector magnet subsystem”. In: *Nuclear Instruments and Methods in Physics Research A* 499 (2003), pp. 633–639. URL: [http://dx.doi.org/10.1016/S0168-9002\(02\)01961-7](http://dx.doi.org/10.1016/S0168-9002(02)01961-7).
- [18] A. Bianconi et al. “Two-hadron interference fragmentation functions. I. General framework”. In: *Phys. Rev. D* 62 (3 2000), p. 034008. doi: 10.1103/PhysRevD.62.034008. URL: <http://link.aps.org/doi/10.1103/PhysRevD.62.034008>.
- [19] A. Bianconi et al. “Two hadron interference fragmentation functions. Part 1. General framework”. In: *Phys. Rev. D* 62 (2000), p. 034008. doi: 10.1103/PhysRevD.62.034008. arXiv:hep-ph/9907475 [hep-ph].
- [20] Daniël Boer, Rainer Jakob, and Marco Radici. “Interference fragmentation functions in electron-positron annihilation”. In: *Phys. Rev. D* 67 (9 2003), p. 094003. doi:

- 10 . 1103 / PhysRevD . 67 . 094003. URL: <http://link.aps.org/doi/10.1103/PhysRevD.67.094003>.
- [21] HERMES Collaboration. “Evidence for a transverse single-spin asymmetry in lepto-production of  $\pi^+\pi^-$  pairs”. In: *Journal of High Energy Physics* 0806 (2008), p. 017. URL: <http://arxiv.org/abs/0803.2367>.
- [22] The COMPASS Collaboration. “Transverse spin effects in hadron-pair production from semi-inclusive deep inelastic scattering”. In: *Phys. Lett. B* 713 (2012), pp. 10–16. URL: <http://arxiv.org/abs/1202.6150>.
- [23] John C. Collins, Davison E. Soper, and George F. Sterman. “Factorization of Hard Processes in QCD”. In: *Adv. Ser. Direct. High Energy Phys.* 5 (1989), pp. 1–91. DOI: 10.1142/9789814503266\_0001. arXiv:hep-ph/0409313 [hep-ph].
- [24] A Courtoy, A Bacchetta, and M Radici. “Dihadron fragmentation functions and their relevance for transverse spin studies”. In: *Journal of Physics: Conference Series* 295.1 (2011), p. 012053. URL: <http://stacks.iop.org/1742-6596/295/i=1/a=012053>.
- [25] A.V. Efremov, L. Mankiewicz, and N.A. Trnqvist. “Jet handedness as a measure of quark and gluon polarization”. In: *Physics Letters B* 284.3 (1992), pp. 394 –400. ISSN: 0370-2693. DOI: [http://dx.doi.org/10.1016/0370-2693\(92\)90451-9](http://dx.doi.org/10.1016/0370-2693(92)90451-9). URL: <http://www.sciencedirect.com/science/article/pii/0370269392904519>.
- [26] R. Gastmans and T. T. Wu. *The Ubiquitous photon: Helicity method for QED and QCD*.
- [27] David Griffiths. *Introduction to Elementary Particles*. Germany: Wiley-Vch, 2004.

- [28] I.Alekseev et al. “Polarized proton collider at RHIC”. In: *Nuclear Instruments and Methods in Physics Research A* 499 (2003), pp. 392–414. URL: [http://dx.doi.org/10.1016/S0168-9002\(02\)01946-0](http://dx.doi.org/10.1016/S0168-9002(02)01946-0).
- [29] R. L. Jaffe. “Can transversity be measured?” In: *Deep inelastic scattering off polarized targets: Theory meets experiment. Physics with polarized protons at HERA. Proceedings, Workshops, SPIN'97, Zeuthen, Germany, September 1-5, 1997 and Hamburg, Germany, March-September 1997.* 1997. arXiv:hep-ph/9710465 [hep-ph]. URL: <http://alice.cern.ch/format/showfull?sysnb=0260728>.
- [30] R. L. Jaffe. “The Theory of the nucleon spin”. In: *Phil. Trans. Roy. Soc. Lond.* A359 (2001), pp. 391–404. DOI: 10.1098/rsta.2000.0731. arXiv:hep-ph/0008038 [hep-ph].
- [31] R. L. Jaffe, Xuemin Jin, and Jian Tang. “Interference Fragmentation Functions and the Nucleon’s Transversity”. In: *Phys. Rev. Lett.* 80 (6 1998), pp. 1166–1169. DOI: 10.1103/PhysRevLett.80.1166. URL: <http://link.aps.org/doi/10.1103/PhysRevLett.80.1166>.
- [32] Robert L. Jaffe. “Where Does the Proton Really Get Its Spin?” In: (1995).
- [33] W.J. Llope et al. “The TOFp/pVPD time-of-flight system for STAR”. In: *Nuclear Instruments and Methods in Physics Research A* 522 (3 2004), pp. 252–273. URL: [doi:10.1016/j.nima.2003.11.414](https://doi.org/10.1016/j.nima.2003.11.414).
- [34] S. Ozaki M. Harrison T. Ludlam. “RHIC project overview”. In: *Nuclear Instruments and Methods in Physics Research A* 499 (2003), pp. 235–244. URL: [http://dx.doi.org/10.1016/S0168-9002\(02\)01937-X](http://dx.doi.org/10.1016/S0168-9002(02)01937-X).

- [35] Gerald G. Ohlsen and P.W. Keaton Jr. “Techniques for Measurement of spin- $\frac{1}{2}$  and spin-1 Polarization Analyzing Tensors”. In: *Nuclear Instruments and Methods* 109 (1973), pp. 41–59.
- [36] Marco Radici, Rainer Jakob, and Andrea Bianconi. “Accessing transversity with interference fragmentation functions”. In: *Phys. Rev. D* 65 (7 2002), p. 074031. DOI: 10.1103/PhysRevD.65.074031. URL: <http://link.aps.org/doi/10.1103/PhysRevD.65.074031>.
- [37] Marco Radici et al. “Exploring universality of transversity in proton-proton collisions”. In: (2016). arXiv:1604.06585 [hep-ph].
- [38] Marco Radici et al. “Improved extraction of valence transversity distributions from inclusive dihadron production”. In: *JHEP* 05 (2015), p. 123. DOI: 10.1007/JHEP05(2015)123. arXiv:1503.03495 [hep-ph].
- [39] Marco Radici et al. “Realistic estimate of valence transversity distributions from inclusive dihadron production”. In: (2015).
- [40] John P. Ralston and Davidson E. Soper. “Production of dimuons from high-energy polarized proton-proton collisions”. In: *Nuclear Physics B* 152.1 (1979), pp. 109–124. ISSN: 0550-3213. DOI: [http://dx.doi.org/10.1016/0550-3213\(79\)90082-8](http://dx.doi.org/10.1016/0550-3213(79)90082-8). URL: <http://www.sciencedirect.com/science/article/pii/0550321379900828>.
- [41] John P. Ralston and Davison E. Soper. “Production of dimuons from high-energy polarized proton-proton collisions”. In: *Nuclear Physics B* 152 (1979), pp. 109–124. URL: [http://dx.doi.org/10.1016/S0168-9002\(02\)01946-0](http://dx.doi.org/10.1016/S0168-9002(02)01946-0).
- [42] Jun She et al. “Transversity from two pion interference fragmentation”. In: *Phys. Rev. D* 77 (1 2008), p. 014035. DOI: 10.1103/PhysRevD.77.014035. URL: <http://link.aps.org/doi/10.1103/PhysRevD.77.014035>.

- [43] P. Z. Skands. “Tuning Monte Carlo Generators: The Perugia Tunes”. In: *PhysRevD* 82 (2010). URL: <http://arxiv.org/abs/1005.3457v5>.
- [44] Jian Tang. “Probing the Nucleon’s Transversity Via Two-Meson Production in Polarized Nucleon-Nucleon Collisions”. In: *Submitted to Phys. Rev. D* (1998). URL: [arXiv:hep-ph/9807560](https://arxiv.org/abs/hep-ph/9807560).
- [45] A. Vossen et al. “Observation of Transverse Polarization Asymmetries of Charged Pion Pairs in  $e^+e^-$  Annihilation near  $\sqrt{s} = 10.58$  GeV”. In: *Phys. Rev. Lett.* 107 (7 2011), p. 072004. DOI: 10.1103/PhysRevLett.107.072004. URL: <http://arxiv.org/abs/1104.2425>.
- [46] J. Zhou and A. Metz. “Dihadron Fragmentation Functions for Large Invariant Mass”. In: *Phys. Rev. Lett.* 106 (17 2011), p. 172001. DOI: 10.1103/PhysRevLett.106.172001. URL: <http://link.aps.org/doi/10.1103/PhysRevLett.106.172001>.